sid.inpe.br/mtc-m21d/2021/07.19.19.39-TDI

PLASMA BLOBS IN THE TROPICAL REGION: A STUDY USING GROUND-BASED OPTICAL AND RADIO TECHNIQUES AND MULTISATELLITE DATA

Oluwasegun Micheal Adebayo

Master's Dissertation of the Graduate Course in Space Geophysics, guided by Dr. Alexandre Alvares Pimenta, approved in July 12, 2021.

URL of the original document:
<http://urlib.net/8JMKD3MGP3W34T/4552AL2>

INPE
São José dos Campos
2021

PUBLISHED BY:

Instituto Nacional de Pesquisas Espaciais - INPE
Coordenação de Ensino, Pesquisa e Extensão (COEPE)
Divisão de Biblioteca (DIBIB)
CEP 12.227-010
São José dos Campos - SP - Brasil
Tel.:(012) 3208-6923/7348
E-mail: pubtc@inpe.br

sid.inpe.br/mtc-m21d/2021/07.19.19.39-TDI

PLASMA BLOBS IN THE TROPICAL REGION: A STUDY USING GROUND-BASED OPTICAL AND RADIO TECHNIQUES AND MULTISATELLITE DATA

Oluwasegun Micheal Adebayo

Master's Dissertation of the Graduate Course in Space Geophysics, guided by Dr. Alexandre Alvares Pimenta, approved in July 12, 2021.

URL of the original document:
<http://urlib.net/8JMKD3MGP3W34T/4552AL2>

INPE
São José dos Campos
2021

Cataloging in Publication Data

Adebayo, Oluwasegun Micheal.

Ad31p Plasma blobs in the tropical region: a study using ground-based optical and radio techniques and multisatellite data / Oluwasegun Micheal Adebayo. – São José dos Campos : INPE, 2021.

xxiv + 120 p. ; (sid.inpe.br/mtc-m21d/2021/07.19.19.39-TDI)

Dissertation (Master in Space Geophysics) – Instituto Nacional de Pesquisas Espaciais, São José dos Campos, 2021.

Guiding : Dr. Alexandre Alvares Pimenta.

1. Aeronomy. 2. Plasma bubbles and blobs. 3. Lifetime. 4. Aeroluminiscence. 5. All-sky imagers. I.Title.

CDU 523.4-8:533.9

MINISTÉRIO DA CIÊNCIA, TECNOLOGIA E INOVAÇÕES

INSTITUTO NACIONAL DE PESQUISAS ESPACIAIS

MASTER'S DISSERTATION DEFENSE OF OLUWASEGUN MICHEAL ADEBAYO
DEFENSE Nº 186/2021 REG 121492/2019

On July 12th, 2021, at 10:00 AM, via videoconference, the above mentioned candidate defended his/her final work before the appointed evaluation committee (oral presentation followed by arguition) named below. The candidate was APPROVED unanimously by the committee, which considered that he/she fulfilled all the requirements for receiving the degree of Master in Space Geophysics/ Atmospheric Sciences. The written text needs to incorporate the suggestions provided by the committee and a final revision from the advisor(s).

Tittle : "PLASMA BLOBS IN THE TROPICAL REGION: A STUDY USING GROUND-BASED OPTICAL AND RADIO TECHNIQUES AND MULTISATELLITE DATA"

Evaluation Committee:

Dr. Alisson Dal Lago - President - INPE - Brazil

Dr. Alexandre Alvares Pimenta - Advisor - INPE - Brazil

Dr. José Augusto Bittencourt - Internal Member - INPE - Brazil

Dr. Francisco Carlos de Meneses Junior - External Member – UANL - Universidad Autónoma de Nuevo León - Mexico

---

Documento assinado eletronicamente por **Alisson Dal Lago**, **Chefe da Divisão de Heliofísica, Ciências Planetárias e Aeronomia**, em 14/07/2021, às 11:18 (horário oficial de Brasília), com fundamento no § 3º do art. 4º do Decreto nº 10.543, de 13 de novembro de 2020.

Documento assinado eletronicamente por **Alexandre Alvares Pimenta**, **Pesquisador**, em 15/07/2021, às 17:01 (horário oficial de Brasília), com fundamento no § 3º do art. 4º do Decreto nº 10.543, de 13 de novembro de 2020.

Documento assinado eletronicamente por **Francisco carlos de meneses junior (E)**, **Usuário Externo**, em 17/07/2021, às 18:37 (horário oficial de

Brasília), com fundamento no § 3º do art. 4º do Decreto nº 10.543, de 13 de novembro de 2020.

Documento assinado eletronicamente por **José Augusto bittencourt (E)**, **Usuário Externo**, em 02/09/2021, às 11:31 (horário oficial de Brasília), com fundamento no § 3º do art. 4º do Decreto nº 10.543, de 13 de novembro de 2020.

A autenticidade deste documento pode ser conferida no site http://sei.mctic.gov.br/verifica.html, informando o código verificador **7882067** e o código CRC **32B302C1**.

Referência: Processo nº 01340.003498/2021-15 SEI nº 7882067

"Whether you think you can, or you think you can't - you're right!"

Henry Ford

I dedicate this dissertation to my family for their unquantifiable supports.

ACKNOWLEDGEMENTS

And so "...with (my) God all things are possible (Matthew 19:26 KJV)." I give honor to the Giver of all Wisdom and the Strength of my life since day 1 in Brazil until now. Grateful heart!

My sincere gratitude goes to my advisor - Dr. Alexandre Alvares Pimenta. When I got to Brazil and I couldn't get a place to study (an office), a friend - Prosper - followed me to Laser where I met Dr. Pimenta showed me his area of research and asked me to take my time to think if I would be interested. Not only was I interested in his research but also his personality, and my first contact with him was more or less like a Father-to-Son interaction. He is a Researcher per excellence. I have learned a lot from him, as an academic advisor and a role model. He supplied me with every single thing I needed for the success of my master's work. Thank you so much for your support in all dimensions. My sincere gratitude also goes to Dr. Siomel Savio for his contribution and knowledge shared with me for the success of this work. In general, I am deeply grateful to everyone at the LASER section of INPE. I love you all!

My profound gratitude goes to all my lecturers who have taught me with passion; they were never tired of my questions. You all made me fall in love with Space Physics. I am so grateful and I count it a rare privilege to have been in your classes. Also, permit me to recognize the excellent contributions made to this work during the proposal defense by the examining board which comprises Dr. Alisson Dallago, Dr. Jonas Souza, Dr. Jose Augusto Bittencourt, and Dr. Alexandre Alvares Pimenta. I must say that INPE is blessed with erudite professors!

I must appreciate all the African and Brazilian friends I met here in Brazil. Being a foreigner and the first time outside of my country, I was opportune to meet supporting and generous friends whose support I was able to acclimatize to the new environment quicker than expected. Most especially Toyese Tunde, Osanyin Taiwo, Prosper Nyassor, Dr. Makinde Olumide and Mrs. Tosin Olumide, Frank, Fernando, Giorgio, Sony Su Chen, Stella, and Hadassa. Thank you all!

I appreciate the Brazilian government through the Conselho Nacional de Desenvolvimento Cientifico e Tecnologico (CNPq) for the Master's fellowship awarded to me and for the sponsorship of my education. I also thank "Instituto Nacional de Pesquisas Espaciais" for the quality education I received and for all the material and infrastructural resources that were made available during the course of my

work. I wish to equally use this opportunity to thank the good people of Brazil whose hard-earned resources were used to give me an opportunity for quality education.

My special gratitude goes to Prof. Babatunde Rabiu and Prof. Sunday Oluyamo for their support at all times. This will be incomplete without showing my deep appreciation to Engr. Oyejide Olapade of the Physics Dept., Bowen University, Iwo for the huge help he rendered for me when no one was ready to do so. Also, my heartfelt gratitude goes to the late Prof. George Adebisi Adebiyi of Bowen University through whose words of encouragement I took my first step towards academic excellence. Your impacts in my life will forever be appreciated.

Through ups and downs, I've found a friend to share my happiness and burdens with and that is Oluwatunmike Damilola Banigbe. I can't thank you enough for your courage, and the trust you have in me. Also, I want to say a big thank you to Mr. and Mrs. Banigbe for their mammoth support and prayers. Thank you so much.

To the blessed memory of my father, Mr. Adebayo Amuda. Memories shared with you will remain in my heart forever. My special gratitude goes to my mother, Mrs. C.D. Adebayo for her unquantifiable support and encouragement. Also, I want to appreciate the support I received from my sisters Oluwaseun and Olabisi and my entire family.

Thank you all!

Oluwasegun Micheal Adebayo

ABSTRACT

Plasma bubbles and plasma blobs are nighttime phenomena in the ionosphere. Bubbles and blobs have been characterized as the regions of plasma depletions and enhancements, respectively. The relationship between the two phenomena has been a subject of research recently and some authors claimed them to be causally related but some claimed them to be independent. In this work, we have studied the occurrence characteristics of plasma enhancements, blobs, and plasma depletions, bubbles, during high solar activity (HSA), and low solar activity (LSA) for the period of two years. OI 630.0 nm emission images from two all-sky imagers at the tropical region over the Brazilian sector were used to study the occurrence characteristics of plasma blobs and bubbles. The intensity enhancements in the airglow images are the optical signature at the height range of the emitting layer of plasma blobs. An all-sky imaging system, observing the OI 630.0 nm emission, was operational at Cachoeira Paulista ($22.7^oS,\ 45.0^oW;\ \approx 16^oS$ dip latitude), Brazil, during the period from October 1998 to July 2000. Also, an all-sky imager, observing OI 630.0 nm emission, has been operational at the Cuieiras Biological Reserve (also commonly referred to as ZF-2: $2.58^oS,\ 60.22^oW$), Brazil, since August 2015 till date. About 3,000 images collected from both imagers were analyzed in this work and the results are presented. The occurrence patterns of both the plasma bubbles and blobs are seasonal dependent, and with the highest occurrence frequency during summer for both HSA and LSA. During HSA, $\approx 95\%$ of plasma blobs observed were associated with plasma bubbles while every single plasma blobs observed during LSA were associated with plasma bubbles; 100%. Notice that not all the plasma bubbles observed were associated with plasma blobs. The Pearson correlation coefficients, based on the monthly hours of the occurrence of plasma blobs and plasma bubbles, during both HSA and LSA, were +0.738 and +0.870, respectively. The average visibility time of plasma blobs, based on their time of appearance and disappearance from the field of view of the all-sky imagers, during HSA and LSA, was 1.08 hr and 0.57 hr, respectively. On the other hand, the average visibility time of plasma bubbles, during HSA and LSA, was 4.01 hr and 2.19 hr, respectively. Also, during HSA and LSA, the plasma blob had an east-west spatial extension of 54-83 km and 41-81 km, respectively. The north-south spatial extension, during HSA and LSA, was 87-129 km and 110-230 km. The nocturnal variation of plasma blobs during HSA and LSA displays different characteristics. Plasma blobs are likely to be formed just after the post-sunset but get fully developed during midnight and vanish just after midnight mostly. We observed, for the first time, plasma blob merging and detachment. Hence, in this work, we have found a strong relationship between the plasma depletions (bubbles) and plasma enhancements (blobs) in the nighttime ionosphere. In addition, plasma enhancements associated with large plasma depletions observed by SWARM constellation satellites are also discussed in this work.

Keywords: aeronomy. plasma bubbles and blobs. lifetime. aeroluminiscence. all-sky imagers.

BLOBS DE PLASMA NA REGIÃO TROPICAL: UM ESTUDO USANDO TÉCNICAS ÓPTICAS E DE RÁDIO BASEADAS EM TERRA E DADOS MULTISATÉLITE

RESUMO

Bolhas de plasma e aumentos localizados na densidade de plasma (blobs) são fenômenos noturnos na ionosfera. Bolhas e "blobs"são caracterizados como regiões de depleções e intensificações do plasma, respectivamente. A relação entre os dois fenômenos tem sido objeto de pesquisa recentemente e alguns autores afirmam que são fenômenos complementares, mas alguns afirmam que são independentes. Neste trabalho, determinamos a frequência de ocorrência dos "blobs"assim como a das bolhas de plasma, durante atividade solar alta (HSA) e baixa (LSA) pelo período de dois anos. Imagens obtidas através da emissão OI 630,0 nm na região tropical brasileira foram usadas para estudar as características de ocorrência de "blobs". Um dos imageadores operou na cidade de Cachoeira Paulista ($22.7^oS,\ 45.0^oW$; $\approx 16^oS$ dip latitude) Brasil, durante o período de outubro de 1998 a julho de 2000 (atividade solar alta). Um outro imageador operando na região Amazônica ($2.58^oS, 60.22^oW$). Cerca de 3000 imagens de OI 630,0 nm foram analisadas para LSA e HSA. O estudo mostrou que a frequência de ocorrência das bolha e dos "blobs"é sazonal tendo uma maior frequência de ocorrência durante o verão para períodos de HSA e LSA. Durante a HSA, approximadamente 95% das "blobs"estão associados a ocorrência das bolhas de plasma. Por outro lado, há casos em que há bolhas porém não há "blobs"ou vice-versa. A correlação de Pearson, baseada nas horas mensais de ocorrência de plasma e "blobs", durante HSA e LSA, foram de $+0,738$ e $+0,870$, respectivamente. O tempo médio de vida dos "blobs", com base em seu tempo de aparecimento e desaparecimento no campo de visão do imageador, durante períodos de HSA e LSA, foi de 1,08 horas e 0,57 horas, respectivamente. Já o tempo médio de vida das bolhas de plasma, durante período de HSA e LSA, foi de 4,01 horas e 2,19 horas, respectivamente. Os "blobs"começam a se formar logo após o pôr do sol, alcançando o máximo desenvolvimento por volta da a meia-noite. Observamos pela primeira vez a fusão e o desprendimento de um "blob". Também encontramos uma forte relação entre o aparecimento de depleções de plasma (bolhas) e aumentos de plasma (blobs) na ionosfera noturna. Além disso, "blobs"e bolhas de plasma foram observados pela constelação de satélites SWARM e o resultado é apresentado..

Palavras-chave: aeronomia. blobs e bolhas de plasma. tempo de vida. aeroluminescência. imageadores all-sky.

LIST OF FIGURES

Page

LIST OF TABLES

Page

CONTENTS

Page

1 INTRODUCTION

1.1 Background to the study

The ionosphere is the large natural blanket of plasma in the atmosphere, which envelopes the Earth from an altitude of approximately 60 km to several thousands of kilometers, (BITTENCOURT, 2013). Most of the ionized particles in the ionosphere, and during the daytime, are produced by absorbing the extreme solar ultraviolet and x-ray radiation by the atmospheric species. The ionosphere contains significant numbers of free electrons and positive ions. There are also some negative ions at the lower altitudes (RANA; YADAV, 2014). The medium as a whole is electrically neutral, there being equal numbers of positive and negative charges within a given volume. Although the charged particles may be only a minority amongst the neutral ones they exert a great influence on the medium's electrical properties and herein lies their importance. To a large extent, the ionosphere varies in a regular and predictable manner, but these regularities may not always accord with simple theory (RANA; YADAV, 2014). In addition, major perturbations called storms occur from time to time, and the spatial structure includes irregularities of various sizes (RANA; YADAV, 2014).

Plasma instability phenomena occurring in the equatorial F-region ionosphere are usually grouped under the generic name equatorial spread F (ESF). This stems from the earliest observations using ionosondes, which showed that on certain occasions the reflected echo did not display a well-behaved pattern but was "spread" in range or frequency. The phenomenon occurs primarily at night, although isolated daytime events occur. The modern era in ESF studies began on a "low" theoretical note in 1970 with the publication of the first compilation of measurements made by the Jicamarca Radar Observatory in Peru (KELLEY, 2009). The equatorial ionosphere suffers serious modifications during the period from sunset to evening. During astronomical twilight conditions, the solar terminator passes through the ionosphere and photoionization ceases. Under the presence of zonal winds in the lower thermosphere, pre-reversal $\mathbf{E}\times\mathbf{B}$ uplifting of the ionosphere produces amplification of plasma density in the off-equatorial latitudes, forming the post-sunset equatorial ionization anomaly (PS-EIA) (TAKAHASHI et al., 2015). The quick uplift also contributes to condition of plasma instability (Rayleigh-Taylor instability), which triggers plasma depletions (bubbles) under certain physical conditions (TAKAHASHI et al., 2015). This phenomenon has been extensively studied for decades using All-sky imagers (GURAV et al., 2019; MENDILLO; TYLER, 1983; MOORE; WEBER, 1981;

PAULINO et al., 2020; PIMENTA et al., 2001; PIMENTA et al., 2004; SAHAI et al., 1994; SAHAI et al., 2000; SHARMA et al., 2018; TAKAHASHI et al., 2015; WEBER et al., 1980), GPS (PAULA et al., 2019), and satellites (PARK et al., 2008). That is, bubbles are seen as plasma depletion holes (in situ measurements), plumes (radar observations), and emission-depletion bands (optical observations). It must be noted that no technique can observe the whole three-dimensional structure of a bubble. But another interesting phenomenon closely related to bubble is a plasma enhancement, also known as blob. It was first reported by Oya et al. (1986) and Watanabe and Oya (1986) carried out the statistical analysis of plasma blob occurrence characteristics using the Hinotori Satellite data. But there was no clear correlation between bubble and blob. Park et al. (2003) using the ROCSAT-1 and DMSP data, they found that the localized plasma density enhancements observed at around $\pm 10^o$-20^o magnetic latitudes were associated with plasma bubbles near the equator and that inside blobs the electron temperature decreased and the O^+/H^+ ratio was higher than that of the ambient, implying that the plasma stemmed from below. Pimenta et al. (2004) reported, for the first time in the literature, ground-based observations of plasma blobs in the tropical region and their association with ESF depletion using optical and radio techniques. Blobs have been reported as an effect of bubbles based on their observation in the same longitudes (HUANG et al., 2014; PIMENTA et al., 2004; PIMENTA et al., 2007; YOKOYAMA et al., 2007) or having similar seasonal distributions (PARK et al., 2003; PARK et al., 2008; WATANABE; OYA, 1986). Also, model simulations showed the occurrence of blobs as an effect of development of bubbles (KRALL et al., 2010; OSSAKOW et al., 1979). Therefore, the development of blobs was associated with the occurrence of large-scale plasma irregularities, bubbles. However, blobs have been reported to be found at the regions where bubbles were absent (KIL et al., 2011) and it was suggested that the generation mechanism of these blobs may be different from the actions of bubbles (KIL, 2015). Luo et al. (2018) using the plasma velocities and the composition variations inside the blobs and bubbles with the results from CHAMP, GRACE, and TEC variations suggests that the meridional wind is crucial and plays an important role in the development of the plasma blobs. In addition, blobs associated with medium scale traveling ionospheric disturbances (MSTIDs) have also been reported by (KIL et al., 2019; MILLER et al., 2014). In short, several other scientific papers have observed plasma bubbles and plasma blobs simultaneously (CHOI et al., 2012; SHI et al., 2017; TARDELLI-COELHO et al., 2017; OYA et al., 1986; WANG et al., 2015).

Plasma blobs and their association with plasma bubbles is still an open research question as no conclusion has been made yet as to whether related to each other

or not. The nocturnal variations, lifetime, and physical dynamics of blobs were still open research questions before this research was conducted. In this work we have extensively studied the plasma blobs and their relationship with plasma bubbles during high solar activity (HSA) and low solar activity (LSA) using various instrumentation used for the study of blobs and bubbles; all-sky imagers, ionosondes, and satellites-borne sensors. For each instrument, both bubbles and blobs were observed simultaneously and with a clear causal relationship. The Pearson correlation coefficients based on the monthly hours of occurrence of blobs and bubbles were positive and quite high. The monthly, seasonal, and nocturnal variations of plasma blobs over tropical region of Brazil are presented in this work. Data used in this work were obtained from two different all-sky imagers located at Cachoeira Paulista (22.7^{o}S, 45.0^{o}W; approximately 16.0^{o}S dip latitude) and ZF-2 (2.58^{o}S, 60.22^{o}W) at Amazon region. In order to study the behaviour of the ionospheric parameters during the occurrence of plasma blobs and plasma bubbles, complementary data were also obtained from an ionosonde located at Cachoeira Paulista. In addition, the result of simultaneous observation of plasma bubbles and plasma blobs by the all-sky imager and SWARM constellation (satellites A and C) is presented.

1.2 Research objectives

The main objective of this work is to study the occurrence characteristics of plasma blobs (monthly, seasonal, and nocturnal) of plasma blobs as a function of the solar cycle. Also, we will investigate if the plasma bubbles at the locations of the blob are a prerequisite condition for the appearance of blobs. Then, we aim to calculate the zonal drift velocities of the selected plasma blobs using the technique presented by Garcia et al. (1997). The north-south and east-west extensions of plasma blobs are also aimed to be estimated. The results of the study are aimed to not only answer the research questions but also elucidate controversy about the plasma blobs and their likely association with plasma bubbles.

1.3 Motivation of the research

The research motivation stems from the controversy around the mechanism responsible for the generation of plasma blobs and their association with plasma bubbles. There have been studies on plasma bubble occurrence characteristics (BARROS et al., 2018; PIMENTA et al., 2001; SAHAI et al., 2000) and its dynamics but the closely related phenomena called plasma blobs have not yet been extensively studied such as their physical dynamics, nocturnal, seasonal, and solar cycle variations.

1.4 The preview of the research

This preview provides the contents of each chapter in this report. Chapter 2 will present background information on Earth's ionosphere and F-region Plasma instabilities: Plasma Bubbles and Plasma Blobs. Chapter 3 will provide an overview of the instrumentation used in this research such as the all-sky imagers, ionosonde, and sensors on board the SWARM constellation. Chapter 4 explains the data analysis and processing in this work and the techniques inculcated. Chapter 5 gives the observations and the results obtained from the research and these include the motional characteristics, physical dynamics; plasma blobs merging and detachment, ionospheric parameters behavior, and measurements from sensors on board SWARM satellites. Chapter 6 gives the conclusion of the whole study.

2 THE FUNDAMENTALS

2.1 Solar cycle

In this work, we studied plasma blobs occurrence characteristics as a function of solar cycle i.e. during the both phases of solar activity. The main feature of the solar magnetic field is the 11-year cycle, as manifested in the (approximately) eleven-year variation of the sunspot number. Sunspots are associated with sites of a strong magnetic field of about 2-3 kG peak field strength (KAMIDE; CHIAN, 2007). Sunspots appear typically at about $\pm 30^o$ latitude at the beginning of each cycle, i.e. when the sunspot number begins to rise again. During the course of the cycle, spots appear at progressively lower latitudes. At the end of the cycle, sunspots appear at low latitudes of about $\pm 4^o$ (KAMIDE; CHIAN, 2007).

Therefore, as shown in Figure 2.1, the beginning of a solar cycle is what referred to as the solar minimum, or low solar activity period, or when the Sun has the least sunspots. Over time, solar activity - and the number of sunspots - increases. While the middle of the solar cycle is the solar maximum or the high solar activity period, or when the Sun has the most sunspots. As the cycle ends, it fades back to the solar minimum and then a new cycle begins.

Figure 2.1 - This split image shows the active Sun during solar maximum (on the left, captured in April 2014) and a quiet Sun during solar minimum (on the right, captured in December 2019).

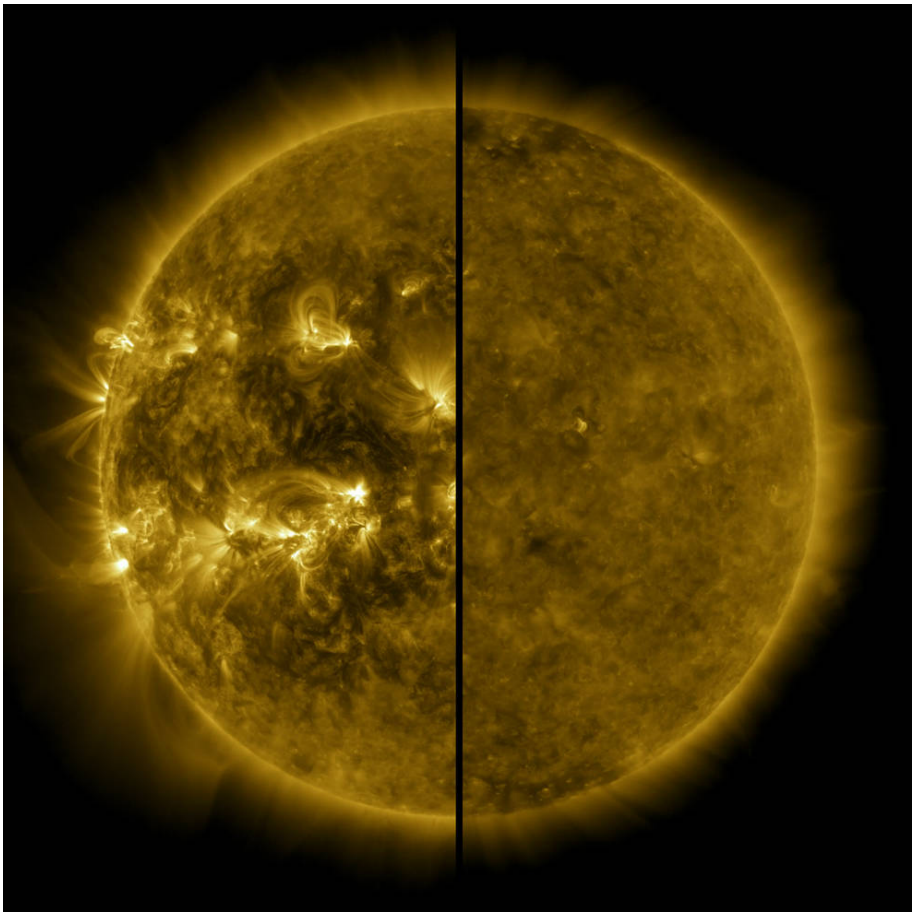

SOURCE: NASA/SDO (2020).

2.2 Earth's magnetic field

According to Campbell (2003), the Earth's magnetic field originated from four main sources: (1) the electric currents that circulate deep inside its interior - outer core (main field); (2) the magnetized material of the crust - (local field); (3) the currents that circulate in the ionized layers of the upper atmosphere (ionosphere and magnetosphere); and (4) the induced currents in the earth's crust (and oceans).

A set of names and symbols is used to describe the Earth's field components in a "right-hand system" (CAMPBELL, 2003). Figure 2.2 illustrates this nomenclature for a location in the Northern Hemisphere where the total field vector points into the

Earth. These components are X, Y, and Z components and are orthogonal i.e. they are at right angles (90^o) to each other. There are two sets of field representations and these are (1) XYZ-component representation; and (2) HDZ-component representation where H, D, and Z are horizontal component, declination, and a vertical component, respectively (CAMPBELL, 2003). The signatures of plasma blobs on these components of the magnetic field have been reported by Park et al. (2008) and Park et al. (2010).

Figure 2.2 - Components of the geomagnetic field measurements for a sample Northern Hemisphere total field vector **F** inclined into the Earth.

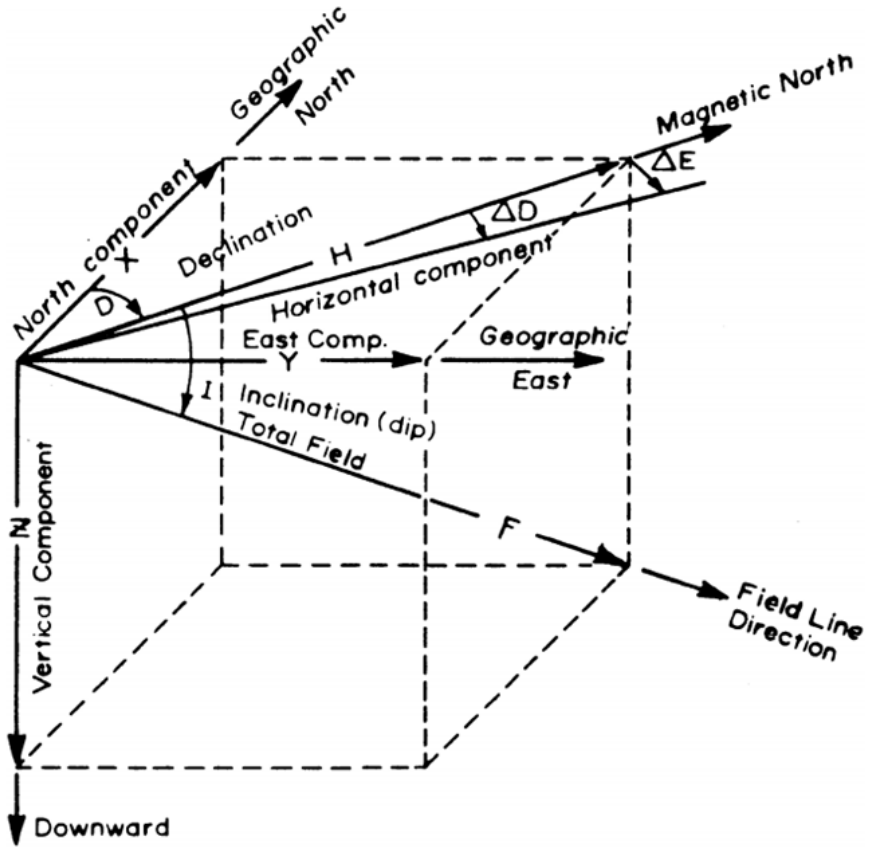

SOURCE: Campbell (2003).

From Figure 2.2, we have

$$X = Hcos(D), \quad Y = Hsin(D) \tag{2.1}$$

and the total field strength, F (or T), is given as

$$F = \sqrt{X^2 + Y^2 + Z^2} \ = \sqrt{H^2 + Z^2} \tag{2.2}$$

The angle that the total field makes with the horizontal plane is called the "inclination," I, or dip angle:

$$\frac{Z}{H} = tan(I) \tag{2.3}$$

It must be noted that when the declination angle is equal to zero, the magnetic field is in the same direction as the geographic pole. When the inclination is equal to zero, the magnetic field is parallel to the Earth's surface. Moreover, the magnetic declination and inclination angles are not constant over the Earth's surface. Cachoeira Paulista and the location of one of the all-sky imagers used in this work is a region with high inclination in Brazil, and this makes the phenomena to tilt westward.

2.3 The earth's ionosphere

The ionosphere is a region that strongly couples with the thermosphere and magnetosphere. As the ionizing radiation from the sun penetrates deeper and deeper into the Earth's atmosphere, it encounters a larger and larger density of gas particles, producing more and more electrons per unit volume (BITTENCOURT, 2013). However, since radiation is absorbed in this process, there is a height where the rate of electron production reaches a maximum. Below this height, the rate of electron production decreases, in spite of the increase in atmospheric density, since most of the ionizing radiation was already absorbed in the higher altitudes (BITTENCOURT, 2013). Several photochemical, chemical, dynamical, and electrodynamical processes take place in this region. As a result, the exchange of mass, momentum, and energy occurs here in a complex manner. The ionosphere extends from about 50km altitude to about 1000 km and has a density high enough electrons and ions that can affect the propagation of a radio wave (RISHBETH; GARRIOTT, 1969). The ionosphere possesses a varying rate of absorption of EUV (Extreme Ultra Violet) radiations by different atoms/molecules. As a result, different ionization peaks or layers are formed, which are called D, E, F1, and F2 layers (RANA; YADAV, 2014) as shown in Figure 2.3. It is a dynamic plasma medium, highly variable in space on scales of meters to hundreds of kilometers and time on scales of seconds to an hour, months, and solar cycles that exhibit climatology and weather features at all latitudes, longitudes, and altitudes (ZOLESI; CANDER, 2014).

During the transition from day to night at the sunset period, the equatorial iono-

sphere suffers serious modification. During astronomical twilight conditions, the solar terminator passes through the ionosphere and photoionization practically ceases. Under the presence of zonal winds in the lower thermosphere, pre-reversal **E** uplifting of the ionosphere produces amplification of plasma density in the off-equatorial latitudes, forming the post-sunset equatorial ionization anomaly (PS-EIA). The quick uplift also contributes to a condition of plasma instability (Rayleigh - Taylor instability), which triggers plasma depletions (bubbles) under certain physical conditions (TAKAHASHI et al., 2015). Plasma blobs, local plasma density enhancements with respect to the background, in low to middle latitudes are understood as by-products of equatorial plasma bubbles, but this hypothesis has been challenged by the observations of blobs in the absence of equatorial bubbles in the same magnetic meridian (CHOI et al., 2012).

Figure 2.3 - ionosphere with various regions (bottomside, topside and plasmasphere) and the ion species associated with the formation of the different ionospheric regions.

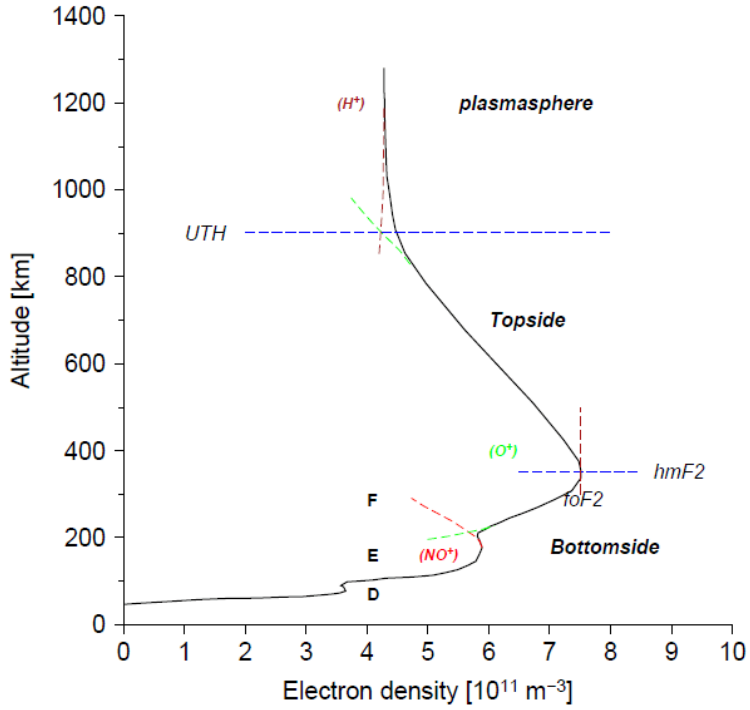

SOURCE: Sibanda (2010).

2.3.1 The formation of ionization

There are essentially two processes, excluding the chemical reactions, which can produce ionization in the upper atmosphere. Radiation can do this only if it is of sufficiently short wavelength. Namely, the energy of light quanta must be high enough to strip the electron from the molecule. This dissociation energy is usually measured in electron volts (eV). For example, the ionization potential energy for the outermost electron of atomic oxygen is 13.6 eV, which can be supplied by radiation of wavelength smaller than about 91 nm, i.e., in the far ultraviolet (BITTENCOURT, 2013). Visible light cannot have an ionizing effect; only ultraviolet light of extremely short wavelength is of interest to us. Most normal layers of the ionosphere are produced by solar radiation in this manner. Furthermore, ionization can be caused by corpuscular emission; i.e, by particles penetrating the earth's atmosphere from outside. These particles might be atoms, electrons, or ions, or conceivably even small dust particles. In this case, also, the energy of the particles must be sufficiently high, in most cases, even a multiple of the ionization potential (RAWER, 1956).

2.3.1.1 Photoionization

The ionospheric layers are formed by photoionization of atoms (X) and molecules (XY). Ionization is mainly owed to EUV - radiation from the sun.

$$\begin{aligned} hv + X &\rightarrow X^+ + e \\ hv + XY &\rightarrow XY^+ + e \end{aligned} \tag{2.4}$$

Ions are lost by recombination through several possible processes:

$$X^+ + e \rightarrow X + hv \ (Slow) \tag{2.5}$$

$$XY^+ + e \rightarrow X^* + Y^* \ (Fast) \tag{2.6}$$

The latter is called dissociative recombination, and leads to the splitting of a molecule into two atoms in an excited state. The process is effective because impulse energy can easily be distributed among X^* and Y^*. In addition, free electrons can form negative ions by attachment:

$$XY + e \rightarrow XY^- \tag{2.7}$$

And the negative ions can be lost by photo detachment:

$$XY^- + hv \rightarrow XY + e \tag{2.8}$$

We get a continuity equation of the form

$$\frac{dn_e}{dt} \;=\; q \;-\; \alpha[XY^+]n_e \tag{2.9}$$

where "q" is the production and $\alpha[XY^+]n_e$ is the loss. Note that $[XY^+]$ refers to the concentration of the molecule XY^+. And the electric neutrality requires that

$$n_e + [XY^-] = [XY^+] \tag{2.10}$$

With the exception of the lowest part of the ionosphere, $[XY^-] \approx 0$ and $n_e = [XY^+]$. We get

$$\frac{dn_e}{dt} = q - \alpha n_e^2 \tag{2.11}$$

The time derivate

$$\frac{d}{dt} = \frac{\partial}{\partial t} + \mathbf{u}.\nabla \tag{2.12}$$

in the more general case where $\overrightarrow{u}$ is the velocity of the air through the volume element we look at. The simplest models assume $\mathbf{u}.\nabla n_e^2 = 0$ so that the equation becomes

$$\frac{dn_e}{dt} = q - \alpha n_e^2 \tag{2.13}$$

The recombination coefficient α depends of what kind of ion species are present. In the equation, α may be replaced by the effective recombination coefficient

$$\alpha_{eff} = \frac{1}{N^+}\sum_{i=1}^{n}(\alpha_i[XY^+]) \tag{2.14}$$

Where α_i refers to a certain ion type. Typical ions are O_2^+, NO^+, O^+ in the E- and F-layer, and composite ions of the type $NO^+(H_2O)_n$ in the lower ionosphere. For NO^+ and O_2^+, $\alpha \approx 5.10^{-7}\ cm^3/s$. When negative ions are present (typical below 75km) we can equate the density of the negative ions with N^- and define $\lambda = \frac{N^-}{n_e}$. By assuming electrical neutrality, the continuity equation becomes:

$$\frac{d}{dt}(n_e + N^-) = q - \alpha_{eff}(n_e + N^-)n_e \tag{2.15}$$

$$\frac{d}{dt}(n_e(1+\lambda)) = q - \alpha_{eff}(1+\lambda)n_e^2 \tag{2.16}$$

If we assume λ time independent we get

$$\frac{dn_e}{dt} = \frac{q}{(1+\lambda)} - \alpha_{eff} n_e^2 \tag{2.17}$$

This equation is similar to Equation 2.13 except for the fact that the ion production q is replaced by an "effective" production $\frac{q}{(1+\lambda)}$ which is always less than q (RAWER, 1956).

2.3.2 The equatorial F-Region dynamo

Winds in the upper thermosphere, produced by the diurnal bulge in thermosphere density, which through collision can interact with F-region ionization to induce fields that in turn can add to dynamo region currents and their effects. During the daytime, the F-region dynamo fields driven by F-region winds are largely short-circuited by the highly conducting E-region. At night, when the E-region conductivity drops drastically, the F-region dynamo can develop an appreciable electric field. The F-region dynamo is particularly effective after sunset when the thermosphere winds are strong and the F-region electron density being quite high (RISHBETH; GARRIOTT, 1969). The F-region dynamo, Figure 2.4, behaves like a constant current generator with high internal impedance. The thermospheric winds provide the source of energy that maintains the electric field in the equatorial region. On average the low-latitude thermosphere superrotates; that is, there is a net eastward average zonal flow of about 150 m/s near 350 km altitude and about 50 m/s at 200 km altitude. The effect is most pronounced in the 21:00-24:00 LT period. Thus, the winds display a high degree of variability from day to day, to a first approximation the winds are eastward and quite strong ($\approx$ 150 m/s) in the postsunset period, decaying in amplitude to less than 50 m/s after midnight (KELLEY, 2009).

Figure 2.4 - Electrodynamics of F-region dynamo. The original image has been slightly modified for the sake of vectorial notation uniformity in this work.

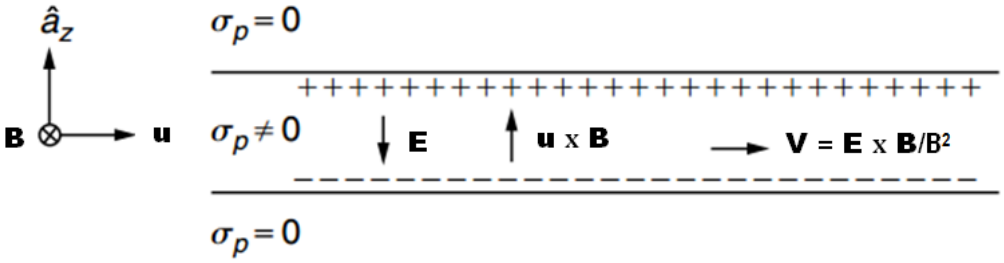

SOURCE: Adapted from Kelley (2009).

2.3.3 Plasma

Plasma is the word used to describe a wide variety of macroscopically neutral substances containing many interacting free electrons and ionized atoms or molecules, which exhibit collective behavior due to the long-range coulomb forces (BITTENCOURT, 2013). The ionosphere does not behave like a pure gas because the number of ionized particles is very large there, hence it is reasonable to consider it as the fourth state of matter i.e. plasma (BANKS, 1973). The electron density is almost exactly equal to the positive ion density in an ionosphere and as a consequence, the net electrical charge density is almost zero; this plasma property is known as quasi-neutrality (BAUMJOHANN; TREUMANN, 1996). The plasma in the solar wind and in the magnetosphere is also quasi-neutral, as are almost all plasmas found in nature. However, unlike ionospheric plasma, the solar wind and magnetospheric plasmas are fully ionized and do not contain neutral atoms and molecules (BAUMJOHANN; TREUMANN, 1996). Ionospheric plasma is one of the closest naturally occurring plasma and is defined in terms of four main parameters like electron density, electron temperature, ion temperature, and ionic composition. The ionosphere is mainly affected by certain natural phenomena like a solar flare, sunspot, magnetic storms, and sudden Ionospheric disturbances (BANKS, 1973). Plasmas are abundant in the universe, and it has been discovered that more than 99% of all known matter is in the plasma state (BAUMJOHANN; TREUMANN, 1996).

Pressure gradient which induces wind, gravity, external electric and magnetic fields have the potential to control the motions of individual plasma species in the iono-

sphere (BANKS, 1973). Although this motion differs from one layer of the ionosphere to the other.The plasma drift across the magnetic field within the E-region results from the flow of polarization currents and the establishment of local and global electric fields (BANKS, 1973). While in the F_2-region the diffusion of ions parallel to the geomagnetic field plays an important part in determining the ionic composition of the middle and upper ionosphere. Furthermore, electric fields perpendicular to the magnetic field cause lateral and radial plasma motions reflecting the importance of magnetospheric processes and neutral winds in the E-region (BANKS, 1973).

2.3.3.1 Plasma criteria

And so the question would be when should we classify an ionized medium to be a plasma? It has been established that a plasma consists of "free positive and negative charge carriers." For this condition to be valid, then the typical potential energy of a free particle due to its nearest neighbor must be much smaller than its random kinetic (thermal) energy (BAUMJOHANN; TREUMANN, 1996). This implies that the particle's motion is practically free from the influence of other charged particles in its neighborhood provided no direct collisions take place (BAUMJOHANN; TREUMANN, 1996). The criteria are:

- **Debye Shielding**: the quasineutral property of a plasma in the stationary state is valid if the numbers of positive and negative charges per volume element are equal. To let the plasma appear electrically neutral, the electric Coulomb potential field of every charge, q

$$\phi_C = \frac{q}{4\pi\epsilon_0 r} \tag{2.18}$$

where ϵ_0 being the free space permitivity, is shielded by other charges in the plasma and assumes the *Debye potential* form

$$\phi_D = \frac{q}{4\pi\epsilon_0 r} exp(-\frac{r}{\lambda_D}) \tag{2.19}$$

in which the exponential function cuts off the potential at distances r > λ_D. The characteristic length scale, λ_D, is called *Debye length* and is the distance, over which a balance is obtained between the thermal particle energy and the electrostatic potential energy. For a plasma to be quasineutral, the physical dimension of the system, L, must be far far greater than the *Debye length*

$$\lambda_D \ll L \tag{2.20}$$

Otherwise there is not enough space for the collective shielding effect to occur, and we have a simple ionized gas. **This is often called the first plasma criterion**.

- **Plasma Parameter**: For the shielding effect as a result of the collective behaviour of the particles inside a Debye sphere of radius λ_D to be valid, then this sphere must contains enough particles (BAUMJOHANN; TREUMANN, 1996). The number of particles inside a Debye sphere is $\frac{4\pi}{3} n_e \lambda_D^3$. The term $n_e \lambda_D^3$ is often called the *plasma parameter*, Λ, and **the second criterion for a plasma** reads

$$\Lambda = n_e \lambda_D^3 \gg 1 \tag{2.21}$$

- **Plasma Frequency**: electron plasma frequency is the typical oscillation frequency in a fully ionized plasma (BAUMJOHANN; TREUMANN, 1996). Denoted by ω_{pe}. Some plasmas, like the Earth's ionosphere, are not fully ionized. That is, these plasmas have a substantial number of neutral particles and if the charged particles collide too often with neutrals, the electrons will be forced into equilibrium with the neutrals, and the medium does not behave as a plasma anymore, but simply like a neutral gas (BAUMJOHANN; TREUMANN, 1996). For the electrons to remain unaffected by collisions with neutrals, the average time between two electron-neutral collisions, τ_n, must be larger than the reciprocal of the plasma frequency

$$\omega_{pe} \tau_n \gg 1 \tag{2.22}$$

This is the third criterion for an ionized medium to behave as a plasma (BAUMJOHANN; TREUMANN, 1996).

2.3.4 Scintillation

According to the effect of the Earth's atmosphere on the electromagnetic waves, the atmosphere is divided into two regions: neutral atmosphere, and ionosphere (HOFMANN-WELLENHOF et al., 2007). Most of the sources of distortion experienced by an electromagnetic signal propagating through the atmosphere come from ionosphere with Bias value of 4.0 (HOFMANN-WELLENHOF et al., 2007), and this is one of the main reasons that makes this region highly important to be studied and understood. The distortion offers to the electromagnetic signal propagating through the atmosphere is mostly known as scintillation. Consider a small-scale structure

encountered by a radio wave propagating through the ionosphere, this causes the signal to either refract or diffract (scatter). This could lead to many consequences depending on the purpose of the signal transmission; for instance, in the case of navigation (e.g. GPS), this can prevent the accurate location of an object of concern. The severity of the scintillation is proportional to the nature of the obstruction encountered by the radio signals. The ionospheric scintillation, Figure 2.5, is quantified by two indexes namely; amplitude scintillation (S_4), and phase scintillation ($\sigma\phi$). Therefore, we study scintillation on radio waves by investigating its impacts on the power and phase of the radio signal of concern.

In terms of latitudinal dependence of the occurrence of scintillation, equatorial and low latitudes experience more of scintillation due to the severity behaviour of the equatorial ionization anomaly (EIA) crests which reside at about $\pm 15^o$ geomagnetic magnetic latitudes (BASU et al., 2002). Other factors that influence the occurrence of scintillation are geomagnetic activity, waves from the lower atmosphere, season, Local time, and solar cycle (BARROS et al., 2018). Scintillation has been one of the great subjects of research in Brazil due to the geographical location of this country, and some of the outstanding works on scintillation have come from this country.

Figure 2.5 - The disorderliness of ionospheric plasma otherwise called scintillation

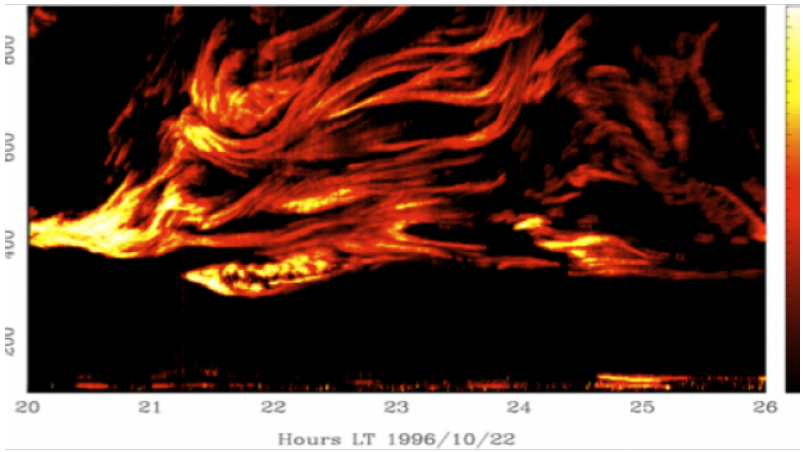

SOURCE: NOAA (1996).

2.4 F-region plasma instabilities

Equatorial Spread F is the generic-name given to the various phenomena occurring as a consequence of plasma instability in the equatorial F-region ionosphere (KELLEY, 2009). The pioneering work on this subject used ionosondes for the observations of this subject, and it was discovered that on certain occasions the reflected echo displayed a "spread" pattern in range or frequency, Figure 2.6. The theoretical studies of ESF started in 1970 and the compilation of the measurements made by the Jicamarca Radar Observatory in Peru was published (KELLEY, 2009).

As a result of this kind of behaviour of plasma in the equatorial region, our understanding of the ambient ionosphere-thermosphere interactive processes and the electrodynamics was limited. Since the discovery of ESF as range spreading F-region in the equatorial post-sunset ionograms (BOOKER; WELLS, 1938), laser-focus has been placed on this phenomenon in the last several decades, and we now have a concrete understanding about their electrodynamics as well as the processes and mechanisms responsible for their development (ABDU et al., 2011).

Figure 2.6 - Range-time intensity (RTI) map displaying the backscatter power at 3 m wavelengths measured at Jicamarca, Peru.

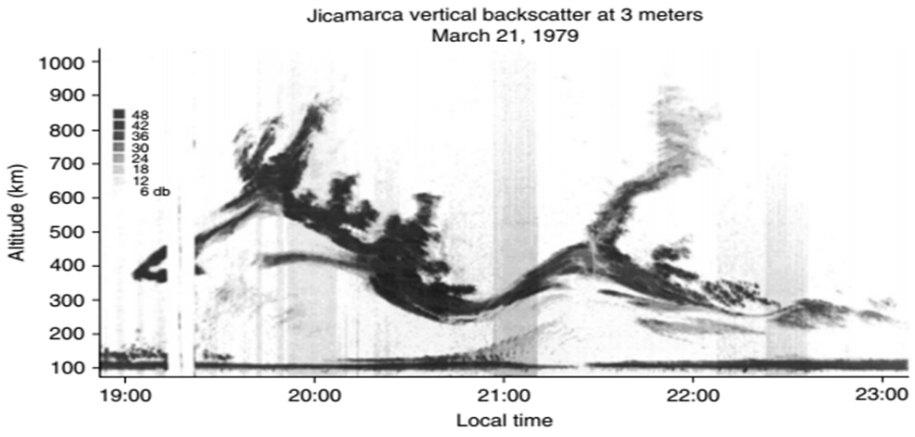

SOURCE: Kelley (2009).

2.4.1 Pre-Reversal Enhancement (PRE)

According to (MARUYAMA; TAKASHI, 2002), due to the **E**×**B** drift the motion of the equatorial ionosphere is generally upward in the daytime and downward in the nighttime. Consider the Figure 2.7, the neutral wind blows eastward, in the presence of magnetic field, this causes the ions to drift upward by collision, and a vertically downward electric field is produced. This field is projected onto the E-region via the geomagnetic field lines which are great conductors. On getting to the boundary of day and night time, the charges accumulate, giving rise to the polarized electric field in the eastward and westward direction. The eastward field is projected back onto the F-region via the geomagnetic field lines where it causes a sudden increase in ionization (normally above the earlier peak) for about 1-2 hours prior to the drift reversal (MARUYAMA; TAKASHI, 2002). This is known as the evening enhancement, or prereversal enhancement, of the equatorial ionospheric electrical field. The rapid recombination reactions that takes place in the E-region at the sunset period and the F-region thermospheric winds are the essential characteristics of the evening enhancement (RAWER, 1956).

Figure 2.7 - Evening pre-reversal enhancement of the equatorial ionospheric electrical field by the F-region dynamo.

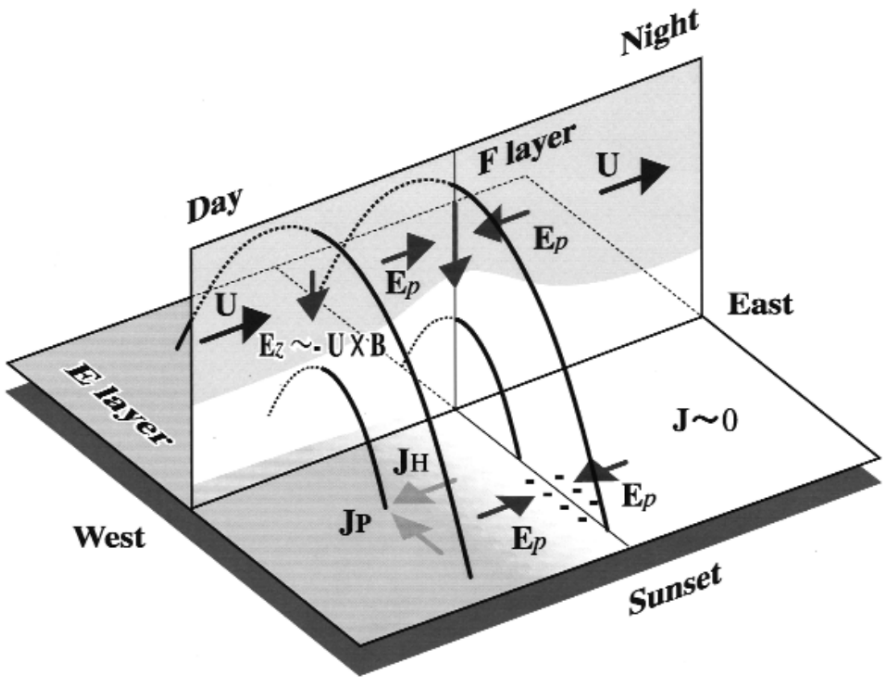

SOURCE: Maruyama and Takashi (2002).

2.4.2 Rayleigh Taylor Instability (RTI)

Figure 2.8 is a linear theory that explains the mechanism responsible for the formation of plasma instability at the bottomside of the ionosphere at the magnetic equator. It is approximated that the magnetic field lines are horizontal in orientation at the equator. Also the F-region plasma at the equatorial region can be considered to be uniform in distribution along the field line due to diffusion. The electrons and ions acted upon by the gravitational force produces eastward electric current. So the presence of a perturbation at the bottomside of the ionosphere causes the isodensity (stable) surface (Figure 2.8) to undulate, and this results into charge separation. Hence, there occurs the accumulation of charges and polarized electric fields are formed in the eastward and westward orientation at the low-density and high-density regions, respectively. So the $\mathbf{E}\times\mathbf{B}$ drift due to this polarization field will be upward and downward in the low-density and high-density regions, respectively (MARUYAMA; TAKASHI, 2002). Consequently, density fluctuation is amplified and this condition is called plasma instability. The growth rate γ (gamma) of the instability in a linear regime can be expressed by the following equation:

$$\gamma = -\frac{g}{v_{in}}\frac{1}{n_{i0}}\frac{\partial n_{i0}}{\partial y} \tag{2.23}$$

where g is the acceleration due to gravity, v_{in} the ion-neutral collision frequency, and n_{i0} the background electron density. It can be deduced from the equation that when the gravitational force and the electron density gradient are anti-parallel, i.e., on the bottomside, the growth rate is positive (note the negative sign on the righthand side of the equation) and that its magnitude is proportional to density gradient (MARUYAMA; TAKASHI, 2002).

Figure 2.8 - Rayleigh Taylor Instability.

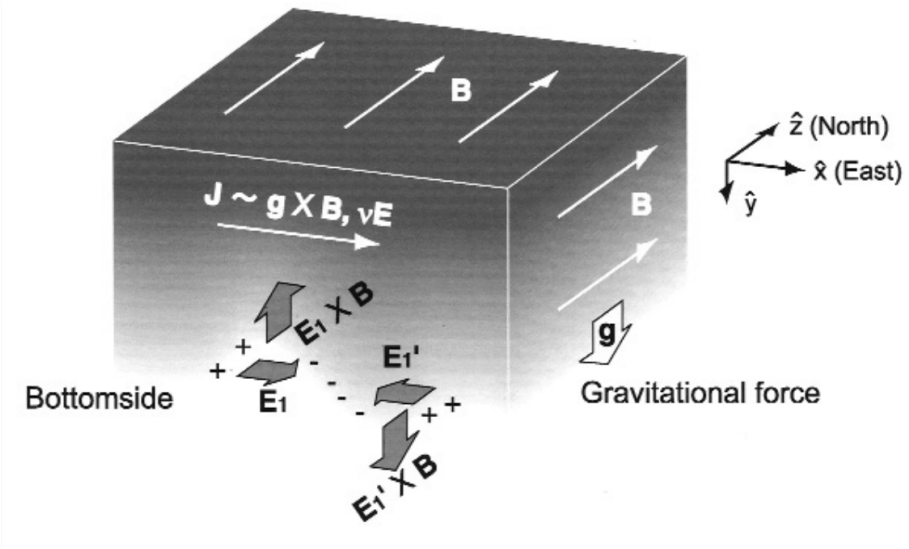

SOURCE: Maruyama and Takashi (2002).

2.4.3 Equatorial plasma bubbles (EPB)

Ionospheric plasma bubbles are regions with depleted plasma and first appear at the bottomside of the F-region (200 km) which extend vertically into the topside of the ionosphere. Because these phenomena are similar to bubbles rising through a liquid, they are called plasma bubbles (ONDOH; MARUBASHI, 2001). They are generated at the magnetic equator after sunset due to plasma instabilities, and as they move upward they map along the magnetic field lines to low latitudes (PIMENTA et al., 2001). The main parameter responsible for the plasma bubble irregularity generation and evolution is the vertical plasma drift during the evening prereversal hours (PAULA et al., 2019). The bubble irregularity growth is regulated also by the magnetic field line integrated conductivity which is controlled by transequatorial/meridional winds and the planetary/gravity waves that propagate upward to the ionospheric F-region (PAULA et al., 2019). The smaller-scale structures that develop inside of the bubbles may contribute to scintillation in the phase and amplitude of radio signals propagating through them. The ionospheric scintillations present a large degree of variability on a day-to-day basis with local time, season, solar activity, magnetic storm, and sudden stratospheric warming-SSW events (BARROS et al., 2018).

2.4.3.1 Mechanism of formation

EPBs are post-sunset phenomena that are generated just after sunset where the recombination process is faster in the E-region which causes plasma density in the F-region to be much higher than in the E-region, creating a steep vertical plasma density gradient toward the F-region (TAKAHASHI et al., 2015). The plasma gradient and the uplifting of the F-region by the pre-reversal enhancement (PRE) through the $\mathbf{E}\times\mathbf{B}$ upward plasma drift create the necessary conditions at the bottom side for the growth of Rayleigh-Taylor instability, (RTI), to trigger the EPBs development (TAKAHASHI et al., 2015).

Figure 2.9 - Sequential sketches made from photos of the hydrodynamic Rayleigh-Taylor instability. The original image has been modified by adding the 'stages' to explain the bubble's development phase.

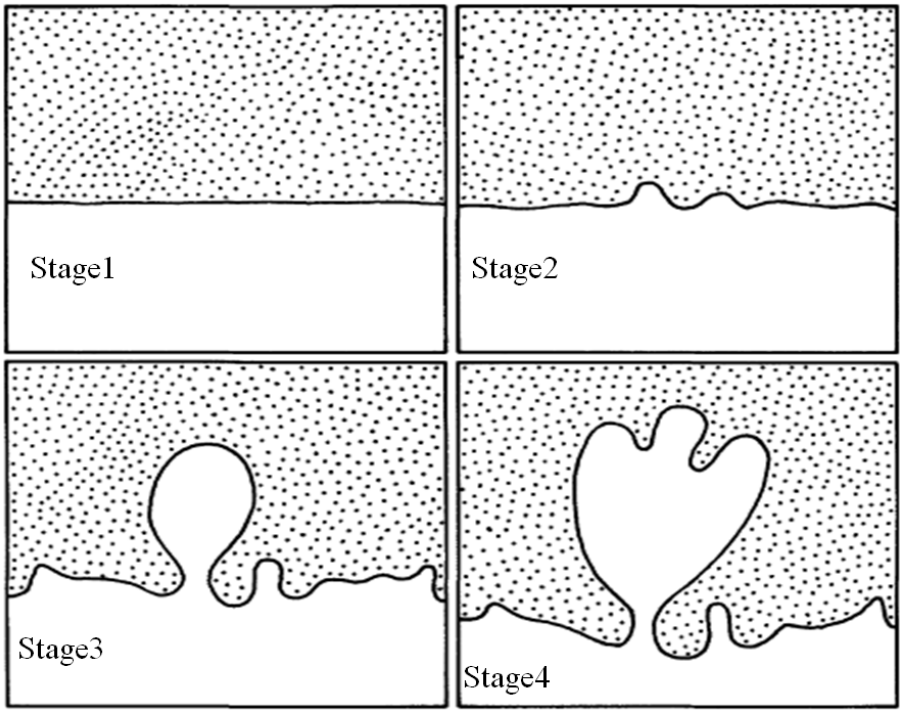

SOURCE: Adapted from Kelley (2009).

Firstly, consider that a steep gradient of the ionospheric plasma region is divided into two parts.Figure 2.9, in region 1 (plain) the concentration of charged particles is zero; in region 2 (dotted) the concentration is not null (see Stage 1). In the absence of

a disturbance, as shown in Stage 1, although the regions have different compositions its elements do not mix.

In the presence of a small disturbance (Stage 2) the environment is unstable and the disturbance tends to grow (Stage 3). Due to the perturbation, the current divergence will not be null, then occur an accumulation of charges at the edge of the disturbed interface producing polarization electric field (see Figure 2.8). The disturbed electric fields produce $\mathbf{E}\times\mathbf{B}$ drift, which removes particles from the region with low density making it even lower, and deposits charges at places with more density. Thus, the disturbance grows generating bubbles/irregularities (Stage 4) (KELLEY, 2009).

2.4.3.2 Effects of EPBs

One of the notable effects of equatorial plasma bubbles is the severe distortion they impose on the radio waves signal passing through the ionosphere by the presence of small-scale structures inside the bubbles (BARROS et al., 2018; PAULA et al., 2019; TAKAHASHI et al., 2015). Figure 2.10 is the image of ionospheric scintillation, showing the parts of a radio wave signal passing through a part of ionosphere with bubbles and another part without bubbles. The signal passing through the disturbed ionosphere is scattered resulting into the multi-path error at the receiver (HOFMANN-WELLENHOF et al., 2007). Therefore the presence of plasma bubbles in the ionosphere creates irregularities that introduce fluctuations in the phase and amplitude of radio signals of communication and navigation systems thereby degrading the signals as they travel through the irregularities.

Figure 2.10 - Scintillation caused by the presence of plasma bubble.

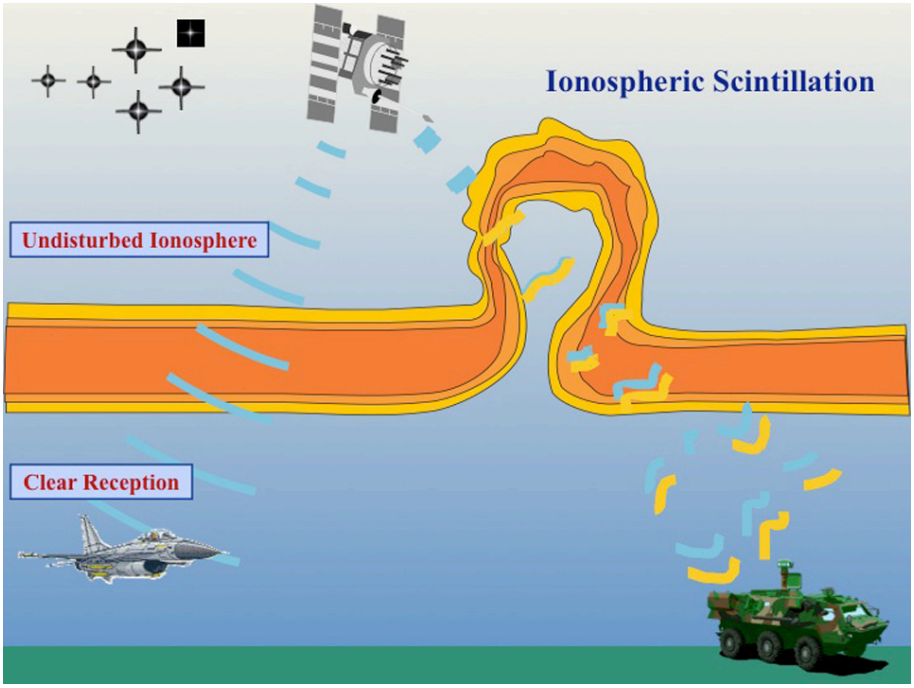

SOURCE: NASA (2013).

2.4.4 Plasma blobs

Plasma blobs are small-scale ionospheric irregularities with plasma density enhancement and generally take place along $\pm 15^o$ geomagnetic latitude (OYA et al., 1986). Using data from the Hinotori satellite, they reported the first observations of localized regions of plasma density enhancements in addition to plasma depletions in the nighttime tropical F-region. Watanabe and Oya (1986) carried out the statistical study and they reported that the occurrence probabilities of plasma depletions and plasma blobs appear to be complementary to each other, and the occurrence region of the plasma blobs is limited to the adjacent parts of the plasma bubble occurrence region. Also, their study indicated that the occurrence of plasma blobs decreases with increasing magnetic activity, while there is a strong anti-correlation of the occurrence of plasma blobs to the solar radiation flux (F10.7).

Pimenta et al. (2004) carried out the first ground-based optical and radio observations of plasma blobs in the tropical region of Brazil, during the period from October 1998 to September 2000 and on several occasions, F-region plasma blob (localized discrete plasma density enhancement) was observed. The plasma blob events were

observed on October 07, 1999, and March 04, 2000, over Cachoeira Paulista (22.7^oS, 45.0^oW); magnetic latitude 13.25^oS, declination 20^oW), showing discrete plasma density enhancements near regions of plasma density depletion structures in the OI 630.0 nm emission images. In the two cases, the electron densities enhanced by a factor of, approximately, 2 above the background level.

2.4.4.1 Formation of plasma blobs

Currently, there is no generally accepted mechanism for the formation of plasma blobs. However, many works have suggested various mechanisms that could be responsible for their formation. Pimenta et al. (2004), using the vertical ionospheric plasma drift velocity variations from their work, they observed that the blob develops just after the reversal of the electric field, when the drift velocity changes from upward (eastward electric field) to downward (westward electric field). Similarly, Wang et al. (2015) also found that the ion drift velocities obtained by ROCSAT-1 showed that the plasma blob was moving upward, accompanied by strong disturbances. Therefore, the eastward polarization electric field should be associated with the plasma blob and its associated density disturbance which then causes the ionospheric amplitude scintillations.

With CHAMP satellite's in situ observations, Park et al. (2008) identified blobs with clear density enhancements and magnetic signatures. They suggested that blobs have a field-aligned structure higher than 400 km and the fluctuations of the perpendicular magnetic fields implying the existence of field-aligned current. Le et al. (2003) reported plasma blobs in situ observed by ROCSAT-1 in the EIA crest region coexisting with EPB observed by DMSP near the magnetic equator. They suggested that blobs in the EIA regions are caused by the polarization electric field, which was generated within EPBs and mapped to the EIA regions along the magnetic field lines. This suggestion was later supported by numerical simulations of Krall et al. (2010), as can be seen in Figure 2.11. They reproduced many observed features and demonstrated the role of polarization electric field. A major characteristic of this view is that plasma blobs occur at the poleward edges of EPBs.

Conversely, Huang et al. (2014) showed cases where plasma blobs were observed equatorward of EPBs using in situ measurements by C/NOFS satellite. The ion density is measured by the planar Langmuir probe (PLP) onboard the C/NOFS, and the ion drift velocity is measured by the ion velocity meter (IVM) and vector electric field instrument (VEFI). Based on the analysis of the cases, they suggested that the relative magnetic latitude and altitude of plasma blobs to bubbles depend

on the evolution stage of bubbles, which changes from the start, intermediate, and fully developed stages of the bubble development. They also suggested that the eastward polarization electric field inside EPBs drives plasma upward and causes plasma blobs just above the upper boundary of the EPBs in the intermediate stage of the bubble development.

Figure 2.11 - Simulation of density enhancements associated with spread F.

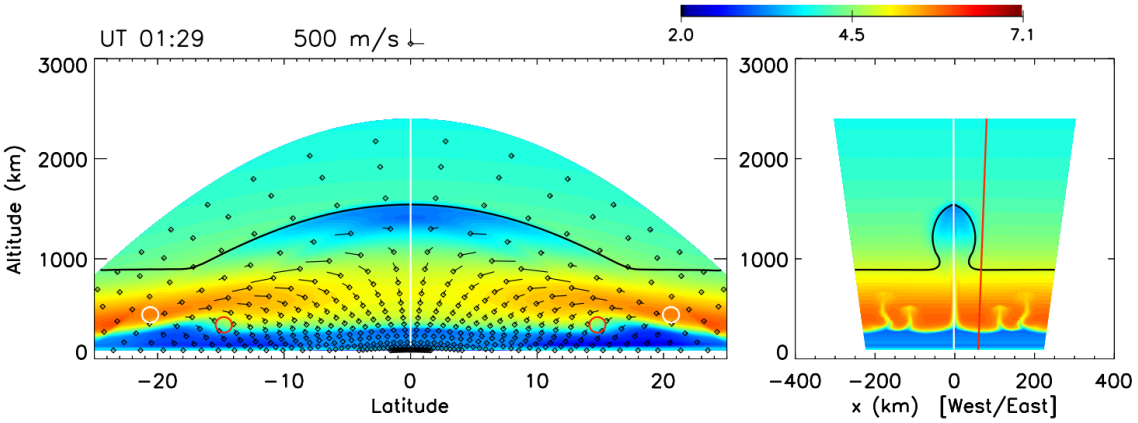

SOURCE: Krall et al. (2010).

2.4.4.2 Effects of plasma blobs

The various effects of plasma bubbles have also been found to be attributed to plasma blobs; they are both consequences of plasma instabilities in the ionosphere. Many investigators have documented various effects of plasma blobs such as the scintillation, and the signatures of blobs on magnetic field components (LE et al., 2003; PARK et al., 2008; PARK et al., 2010; PARK et al., 2015; SHI et al., 2017; WANG et al., 2015).

Some authors have observed the relationship between plasma blobs and radio signal (or ionospheric) scintillations. With the 136-MHz geostationary satellite data Maruyama (1991) studied the ionospheric scintillations over Wakkanai station $(45^oN, 141^oE)$. With the 244-MHz data Paul et al. (2001) studied the ionospheric scintillations over the station Haringhata $(22.97^oN, 88.5^oE)$. Both of them found that the radio signal scintillations were produced by small-scale plasma blobs.

Ionospheric scintillations at low latitude are considered as signatures of equatorial plasma bubbles (depletions). However, some authors considered that scintillations may also be associated with plasma blobs (enhancements). Wang et al. (2015) performed a case study on the concurrent observation of an ionospheric plasma blob with in-situ measurements by ROCSAT-1 and of GPS amplitude scintillations in the low latitude ionosphere on June 1, 2003. The blob measured in situ had a scale size of about 800 km in the F-layer, and the ion density inside the blob was severely disturbed; the density inside the blob peaked at twice that outside the blob. Amplitude scintillation with $S_4 > 0.3$ was observed concurrently in the same longitude range as the blob measured. They discovered that according to the relative densities of each species, the blob was mainly caused by O^+ ion activity. The observation period of the plasma blob was within the observation periods of scintillations, and the longitude ranges of these two phenomena were nearly the same. In their study, the ion drift velocities obtained by ROCSAT-1 showed that the plasma blob was moving upward, accompanied by strong disturbances. Therefore, the eastward polarization electric field should be associated with the plasma blob and its associated density disturbance which then causes the ionospheric amplitude scintillations. Rezende et al. (2007) in their work - mapping and survey of Plasma Bubbles over Brazillian Territory, observed that amplitude ranges of scintillation increase from the equator to the anomaly crest due to the background ionization enhancement.

The formation flight of Swarm satellites provides a unique opportunity to identify the horizontal structure of blobs as reported by Kil et al. (2019). From a preliminary survey of Swarm observations at low and middle latitudes in 2014, Kil et al. (2019) identified blobs that show the conjugate property and the alignment in the northwest direction in the Northern Hemisphere and in the southeast direction in the Southern Hemisphere. These are the characteristics of nighttime MSTIDs. The detection of MSTIDs by TEC perturbation maps near the locations of the blobs and the absence of bubbles in the equatorial region at the times of the blob detection further support the association of the blobs with MSTIDs.

2.4.5 Theoretical and numerical relationship between plasma bubbles and plasma blobs

Ossakow et al. (1979) worked on four different two-dimensional plasma fluid-type numerical simulations following the nonlinear evolution of the collisional Rayleigh-Taylor instability in the nighttime equatorial F-region ionosphere. The ambient geomagnetic field $\mathbf{B}$ is taken to be constant and in the z-direction, the y axis is vertically

upward (altitude), gravity $\mathbf{g}$ is in the negative y-direction, the x-axis points westward, and $\mathbf{g} \times \mathbf{B}$ is toward the east. The ambient electron density profile depicted in Figure 2.12 shows a steep bottomside. The bottomside steepens owing to recombination effects and electrodynamic forces. In what follows, we will neglect any motions or variations parallel to $\mathbf{B}$. Consequently, all spatial derivatives will be taken in the x, y plane.

Figure 2.12 - Geometry of Equatorial spread F. N(y) represents the ambient electron density profile and only depends on the altitude (y). $\mathbf{B}$ points to the north, x is west, and so $\mathbf{g}\times\ \mathbf{B}$ is to the east. A horizontal pertubation is denoted by $\mathbf{k}$. The original image has been modified for the sake of the vectorial notation uniformity.

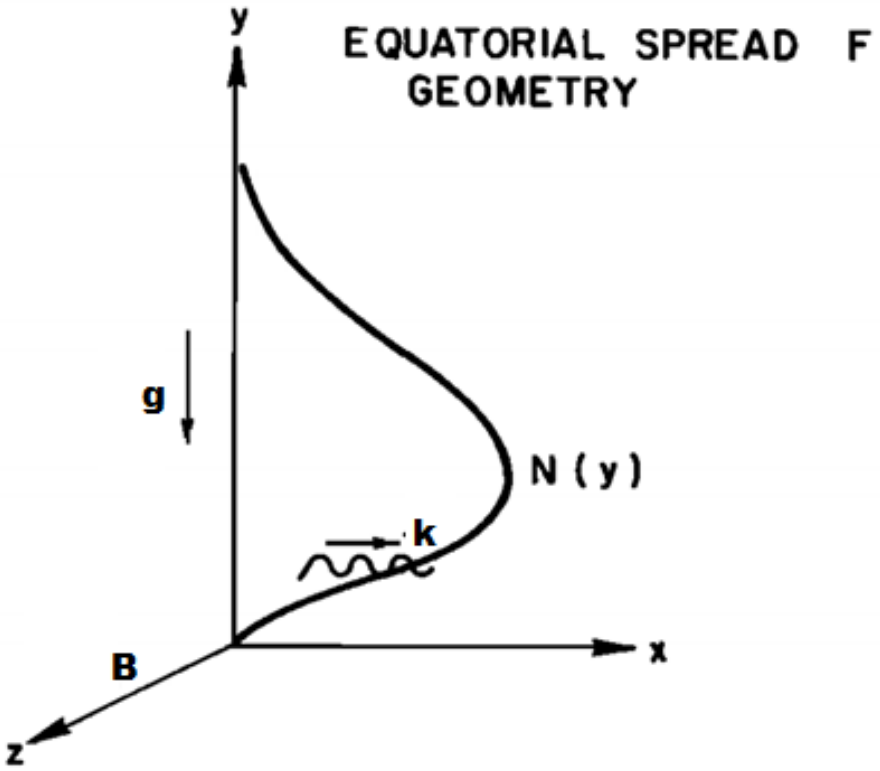

SOURCE: Ossakow et al. (1979).

The basic plasma two-fluid equations describing the system are

$$\frac{\partial n_\alpha}{\partial t} + \nabla.(n_\alpha \mathbf{v}_\alpha) = -\nu_R(n_\alpha - n_{\alpha 0}) \tag{2.24}$$

$$\left(\frac{\partial}{\partial t} + \mathbf{v}_\alpha.\nabla\right)\mathbf{v}_\alpha \;= \frac{q_\alpha}{m_\alpha}\left(\mathbf{E} \;+ \frac{\mathbf{v}_\alpha \;\times \mathbf{B}}{c}\right) \;+ \mathbf{g} - \nu_\alpha \mathbf{v}_\alpha \tag{2.25}$$

where the subscript α denotes species (e is electron, i is ion), n is charged particle number density, $\mathbf{v}$ is velocity, ν_R is recombination rate, $\mathbf{E}$ is the electric field, $\mathbf{g}$ is gravity, q is the charge, ν is collision frequency, c is the speed of light, and m is mass. Note that $n_{\alpha 0}$ in Equation 2.24 is the equilibrium value of the density such that in equilibrium the right-hand side of Equation 2.24 is zero. In the usual form, the right-hand side of Equation 2.24 would have a source minus a loss. The loss term is represented by -$\nu_R n_\alpha$, and we have set the source term equal to $\nu_R n_\alpha 0$, such that $\frac{dn_{\alpha 0}}{dt} = 0$. The recombination rate ν_R represents a combination of the rate-limiting charge exchange reaction

$$O^+ \;+ O_2 \;\xrightarrow{K_1}\; O_2^+ \;+ O \tag{2.26}$$

and the ion-molecule reaction

$$O^+ \;+\; N_2 \xrightarrow{K_2}\; NO^+ + N \tag{2.27}$$

such that

$$\nu_R \;= K_1 n(O_2) \;+\; K_2 n(N_2) \tag{2.28}$$

where $n(O_2)$ and $n(N_2)$ are the neutral number densities of O_2 and N_2, respectively. In Equation 2.25 the temperature and neutral wind have been set to zero (equivalently, we are in a frame moving with the neutral wind). Equation 2.25 is then solved for the electron and ion velocities as follows. The left-hand side of Equation 2.25, i.e., the inertial terms, is neglected, so that the time changes associated with these terms occur over a time scale longer than the gyroperiod or collision time (equivalently, the frequency associated with the inertial terms is small compared to the gyrofrequencies and collision frequencies). For the electrons we take $\nu_e/\Omega_e = 0$, where $\Omega_e = eB/m_\alpha c$, and for the ions $\nu_i/\Omega_i \ll 1$, whereby ν_i we mean ion-neutral collisions (ν_{in}). The equations for the electron and ion velocities are then given by

$$\mathbf{v}_e \;= \frac{c}{B}\mathbf{E} \times \hat{z} \qquad \hat{z} = \frac{\mathbf{B}}{\mid B \mid} \tag{2.29}$$

$$\mathbf{v}_i = \left(\frac{\mathbf{g}}{\Omega_i} \;+\; \frac{c}{B}\mathbf{E}\right) \times \hat{z} + \left(\frac{\mathbf{g}}{\Omega_i} + \frac{c}{B}\mathbf{E}\right)\frac{\nu_{in}}{\Omega_i} \tag{2.30}$$

where in Equation 2.29 we have neglected the electron $\mathbf{g} \times \hat{z}$ motion, because compared with the same ion motion, the ratio is m_e/m_i. Considering the quasi-neutrality such that $n_e = n_i = n$, and using

$$\nabla.j \ = 0 \qquad j = en(\mathbf{v}_i - \mathbf{v}_e) \tag{2.31}$$

Equation 2.31 can be obtained by substracting the electron continuity equation from the ion continuity equation. The electrostatic approximation is made, i.e., $\mathbf{E} = -\nabla\phi$, and we then obtain

$$\frac{\partial n}{\partial t} \ - \ \frac{c}{B}\left(\nabla\phi \times \hat{z} + \frac{m_i}{e}\mathbf{g} \times \hat{z}\right).\nabla n = -\nu_R(n - n_o) \tag{2.32}$$

$$\nabla.(\nu_{in} n \nabla\phi) = \frac{m_i}{e}\mathbf{g}.\nabla(\nu_{in} n) + \frac{B}{c}(\mathbf{g} \times \hat{z}).\nabla n \tag{2.33}$$

Then we set $\phi = \phi_o \ + \ \phi_1$, where ϕ_o is the zero order potential and ϕ_1 is the induced or perturbed potential. The zero order solution of Equation 2.32 and Equation 2.33 requires that $\nabla\phi_o \ = \ m_i\mathbf{g}/e$. Note that this equilibrium value of the potential makes $\mathbf{v}_{io} \ = 0$ (see Equation 2.30) and makes $\mathbf{v}_{eo} \ = \ -(\mathbf{g} \times \hat{z}/\Omega_i)$. Thus, the equilibrium current is carried by the electrons, and we have $j_o \ = \ -n_o e g\hat{x}/\Omega_i$. We then neglect any other zero order or ambient electric fields so that Equation 2.32 and Equation 2.33 become

$$\frac{\partial n}{\partial t} \ - \frac{c}{B}(\nabla\phi_1 \times \hat{z}).\nabla n \ = \ -\nu_R(n - n_o) \tag{2.34}$$

$$\nabla.(\nu_{in} n \nabla\phi_1) = \frac{B}{c}(\mathbf{g} \times \hat{z}).\nabla n \tag{2.35}$$

If ν_{in} were constant, then $(B/c\nu_{in})(\mathbf{g} \times \hat{z})$ would play the role of an effective electric field, and $-\nabla\phi_1$ is the induced or polarization electric field. Equation 2.34 and Equation 2.35 are the basic equations we wish to solve for n and ϕ_1 in the x and y plane. In these equations, n_o, ν_{in}, and ν_R are functions of y (altitude). We note that inclusion of a scalar electron and ion pressure with $T_e = T_i = T$ in Equation 2.29 and Equation 2.30 results in Equation 2.34 and Equation 2.35 with ϕ_1 being replaced by $\psi = \phi_1 + (T/e)ln(n/n_o)$. This has no effect on the linear growth rates which follow or on the nonlinear evolution. We may obtain the linear growth rate from Equation 2.34 and Equation 2.35 by assuming that

$$n = n_o(y) + n_1 e^{t(k_x x + k_y y - wt)} \tag{2.36}$$
$$\phi_1 = \phi_1 e^{t(k_x x + k_y y - wt)}$$

where we have made the local approximation k $\gg (\partial n_o/\partial y)(1/n_o)$. This results in the determinant set of equations

$$(-i\omega + \nu_R)n_1 + i\frac{c}{B}\frac{\partial n_o}{\partial y}k_x\phi_1 = 0 \tag{2.37}$$

$$\frac{B}{c}ik_x g n_1 + \left(\frac{\partial(n_o\nu_{in})}{\partial y}ik_y - n_o\nu_{in}k^2\right)\phi_1 = 0 \tag{2.38}$$

This set yields

$$\omega = -\frac{ik_x^2 g\frac{\partial n_o}{\partial y}}{iky\frac{\partial(n_o\nu_{in})}{\partial y} - n_o\nu_{in}k^2} - i\nu_R \tag{2.39}$$

Setting $\omega = \omega_r + i\gamma$, we obtain

$$\gamma = \frac{(\frac{\partial n_o}{\partial y})k_x^2 g n_o\nu_{in}k^2}{(n_o\nu_{in}k^2)^2 + k_y[\partial(n_o\nu_{in})/\partial y]^2} - \nu_R \tag{2.40}$$

$$\omega_r = \frac{-k_x^2 k_y[\partial(n_o\nu_{in})/\partial y]g(\partial n_o/\partial y)}{(n_o\nu_{in}k^2)^2 + k_y[\partial(n_o\nu_{in})/\partial y]^2} \tag{2.41}$$

Equation 2.40 for the growth rate γ clearly shows that one can have growth (positive γ) only on the bottomside of the F peak where $\partial n_o/\partial y > 0$. Moreover, growth (instability) occurs when the first term (in right side) in Equation 2.40 is greater than the second. Equation 2.40 clearly shows that on the topside where $\partial n_o/\partial y < 0$, γ is negative (stable). For purely horizontal propagating waves ($k_y = 0$) the above discussion still applies, and we obtain

$$\gamma = \frac{1}{n_o}\frac{\partial n_o}{\partial y}\frac{g}{\nu_{in}} - \nu_R \tag{2.42}$$

$$\omega_r = 0 \tag{2.43}$$

and we can identify $n_o(\partial n_o/\partial y)^{-1}$ with the background electron density gradient scale length L. In the denominator of Equation 2.40 and Equation 2.41 the second term is small compared with the first if kL $\gg 1$ (neglecting the ν_{in} altitude dependence), which is just the local approximation. Then Equation 2.40 and Equation 2.41

become

$$\gamma = \frac{1}{n_o}\frac{\partial n_o}{\partial y}\frac{k_x^2}{k^2}\frac{g}{\nu_{in}} - \nu_R \tag{2.44}$$

$$\omega_r = -\frac{k_x^2 k_y g(\partial n_o/\partial y)[\partial(n_o\nu_{in})/\partial y]}{(n_o\nu_{in}k^2)^2} \tag{2.45}$$

Equation 2.44 shows that the growth rate is independent of $\mid k \mid$ and maximizes when $k^2 = k_x^2$ (horizontal propagation). Also if one neglects the y dependence of ν_{in}, then Equation 2.45 shows that $\omega_r \approx -(g/\nu_{in}L)(1/kL)$ or $-(kL)^{-1}$ times the growth rate. Ossakow et al. (1979) in their numerical simulations, four equatorial spread F (ESF) cases were considered and the varying parameters were the height of F peak and the minimum bottomside scale length, L. All other conditions were the same from simulation to simulation. All the four nonlinear numerical simulations were performed over a two-dimensional mesh corresponding to an altitude (y) range of 200 km, and an east-west(x) extent of 8 km.

In this work, we shall only use the first case (ESF 1) and the last case (ESF 3) of ESF to explain the relationship between the plasma depletions, bubble, and plasma enhancements, blobs; for details consult Ossakow et al. (1979). In the first case (ESF 1, see Figure 2.13) the F peak height of 354 km, the scale length of 10 km, and time, t of 2000, 4000, 8000, and 10000 seconds were used for the simulation and the results were summarized below:

Figure 2.13 - Contour plots of constant n_1/n_o for the simulation ESF 1. The small dashed contours with a plus sign inside and the solid contours with a minus sign inside indicate enhancement and depletions over the ambient electron number density. The large dashed curve depicts the ambient electron number density n_o as a function of altitude. The vertical y axis represents altitude, the lower horizontal x axis is the east-west range, and the ambient magnetic field is along the z axis, out of the figure.

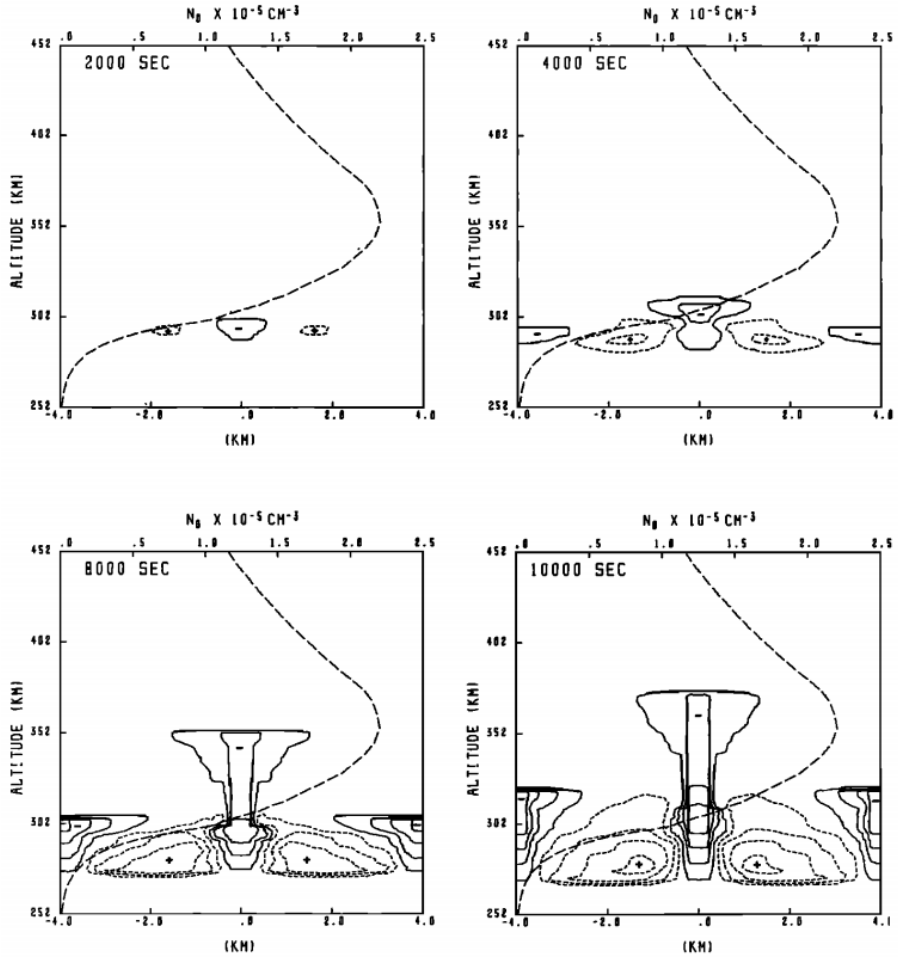

SOURCE: Ossakow et al. (1979).

- At t=2000 s the early phase of the growth of the collisional Rayleigh-Taylor instability is exhibited. It shows the formation of plasma density enhancements (pluses) and depletions (minuses), depicted by small dashed and solid contours, respectively. The depletion contour had 16% depletion, with a maximum of 27% within the contour, whereas the enhancement contour represents a 19% enhancement, with a maximum of 23% within the contour. Thus, the depletion has the highest percentage within the

contour.

- At t=4000 s the density depletion is already rising with innermost depletion within this contour of 41% and with a maximum depletion of 54%. The innermost enhancement contour of 68% and with a maximum enhancement of 84% within this contour. Also, there is the formation of other depletions in the wings. Thus, the enhancement has the highest percentage within the contour. I suppose, aside from the gravity, the two bubbles are exerting opposite force on the enhancement causing it to increase in magnitude as it does not rise, unlike the bubble.

- At t=8000 s the density depletion upper boundary is at the F peak. The innermost contour of the rising bubble is a 41% depletion; however, there is a 58 % depletion contour below this at an altitude of $\approx 300km$, and within this contour a maximum depletion of 66%. The plasma enhancements, confined at $y \leq 302$ km with innermost contour contours of 138% enhancements and maximum enhancements inside these innermost contours of 226%. Note that the bubbles at the wings are, at this moment, extending over the enhancements and the bottomside of the enhancements is getting steepen. Thus, the top and the bottom of the enhancements are constrained.

- At t=10,000 s the main bubble is above the F peak with an innermost depletion contour of 41%. However, in the ionosphere below the bubble near $x = 0$, there is a 71% depletion contour with a maximum depletion inside this contour of 73%. In the wings, there are depletions with innermost contours of 71 %, and inside of these depletion contours maximum depletions of 75%. The innermost enhancement contour is 236% with a maximum inside this contour of 294%. Notice that the higher the altitude of the bubble the lower the depletion's contour percentage.

Basically, the isolated depletions move upward, while isolated enhancements move downward in the equatorial spread F geometry (OSSAKOW; CHATURVEDI, 1978), however, this concept is altered when depletions are surrounded by enhancements or vice-versa. So from Figure 2.13, we see that the more isolated high-latitude part of the central bubble is acted on by an induced electric field which points from the west (positive x) to the east (negative x) and is dipolar in nature. This causes the bubble to rise with a velocity $(-c/B)\nabla\phi_1 \times \hat{z}$. However, the lower portion of the mesh is acted on by an induced electric field that points from east to west and is

much weaker than the induced electric field acting upon the isolated portion of the central bubble (OSSAKOW et al., 1979). This basically causes the enhancements to move downward along with the lower altitude depletions. Thus the lower part of the central becomes 'captured' by the enhancements.

In the third case (ESF 3, see Figure 2.14), the results were completely different from the first case (ESF 1). At this time the F peak height of 434 km; this F peak is 80 km higher than it was for ESF 1, the scale length of 10 km and time, t of 300, 700, 1000, and 1400 seconds were used for the simulation and the results were summarized as:

(1) the simulation was developing more rapidly than ESF 1;

(2) the entire bottomside was linearly unstable;

(3) the bubble rose far above the F peak and

(4) the depletions and the enhancements contours percentage pattern were similar to the ESF 1 but of course, larger.

Figure 2.14 - Contour plots of constant n_1/n_o for the simulation ESF 3 at t = 300, 700, 1000, 1400s. All other nomenclature is same as Figure 2.13.

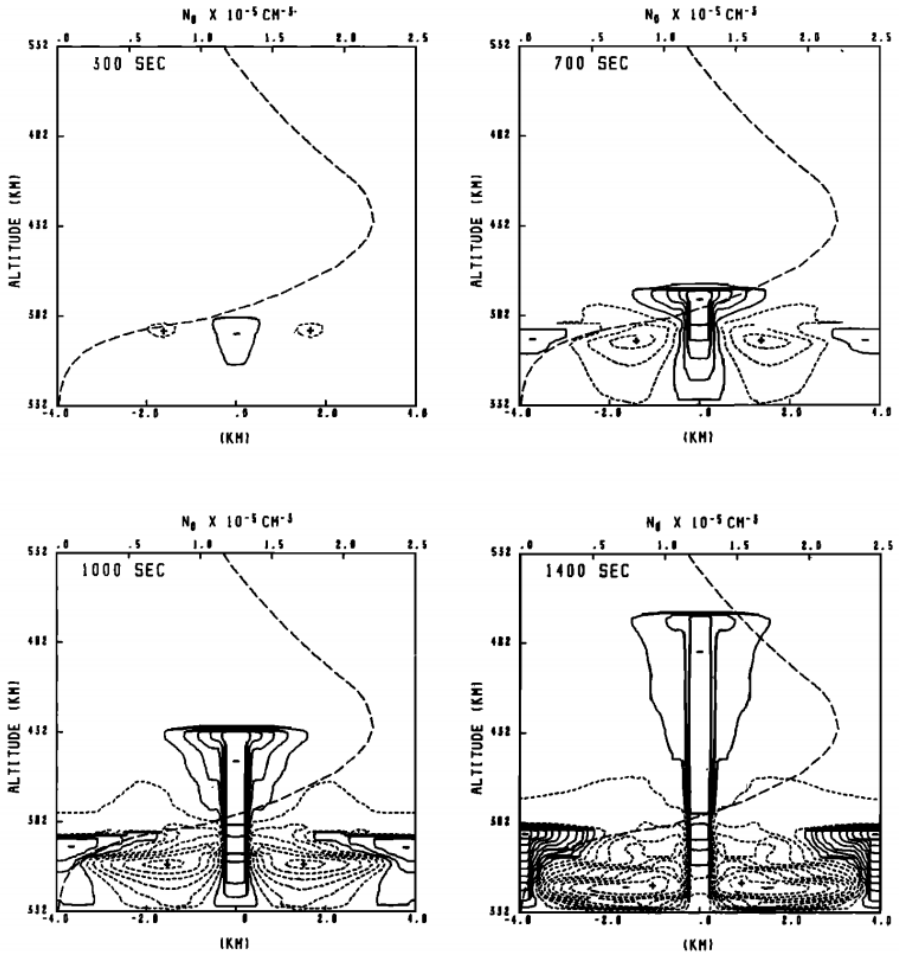

SOURCE: Ossakow et al. (1979).

In summary, they reported that under favorable conditions, e.g., the high altitude of the F peak (small effective ion-neutral collision frequency) and/or steep bottomside background electron density gradients, the collisional Rayleigh-Taylor instability causes linear growth on the bottomside of the F region. This is in turn causes plasma density depletions or bubbles to be formed on the bottomside which then steepen on their top and nonlinearly rise to the topside by polarization (induced) $\mathbf{E} \times \mathbf{B}$ motion. Lastly, they found that changing the altitude of the F peak from 300 km to 430 km can have dramatic effects on the evolution of equatorial spread F.

2.4.6 Causal relationship between plasma bubbles and plasma blobs

A good relationship has been found between the occurrence of plasma blobs associated with plasma bubbles (HUANG et al., 2014; KRALL et al., 2010; LE et al., 2003; OYA et al., 1986; PIMENTA et al., 2004; PIMENTA et al., 2007; WANG et al., 2019). Conversely, scientists have also observed plasma blobs in the absence of plasma bubbles or associated with other phenomena (CHOI et al., 2012; KIL et al., 2019; SHI et al., 2017).

Huang et al. (2014) demonstrated how plasma depletions (bubbles) are related to plasma enhancements (blobs). Figure 2.15 illustrates the growth of a plasma bubble and the formation of plasma enhancements. Plasma bubbles result from the nonlinear evolution of the Rayleigh-Taylor instability near the magnetic equator. Numerical simulations have shown that the Rayleigh-Taylor instability can be triggered by an initial plasma density perturbation, gravity waves, or electric field disturbances.

Figure 2.15 - (a - c) Illustration of the evolution of plasma depletions and the formation of plasma enhancements. The blue lines represent the geomagnetic field lines. The red lines represent the plasma density contours, and the heavy red line represents the F peak. The red arrows indicate the direction of the plasma flow.

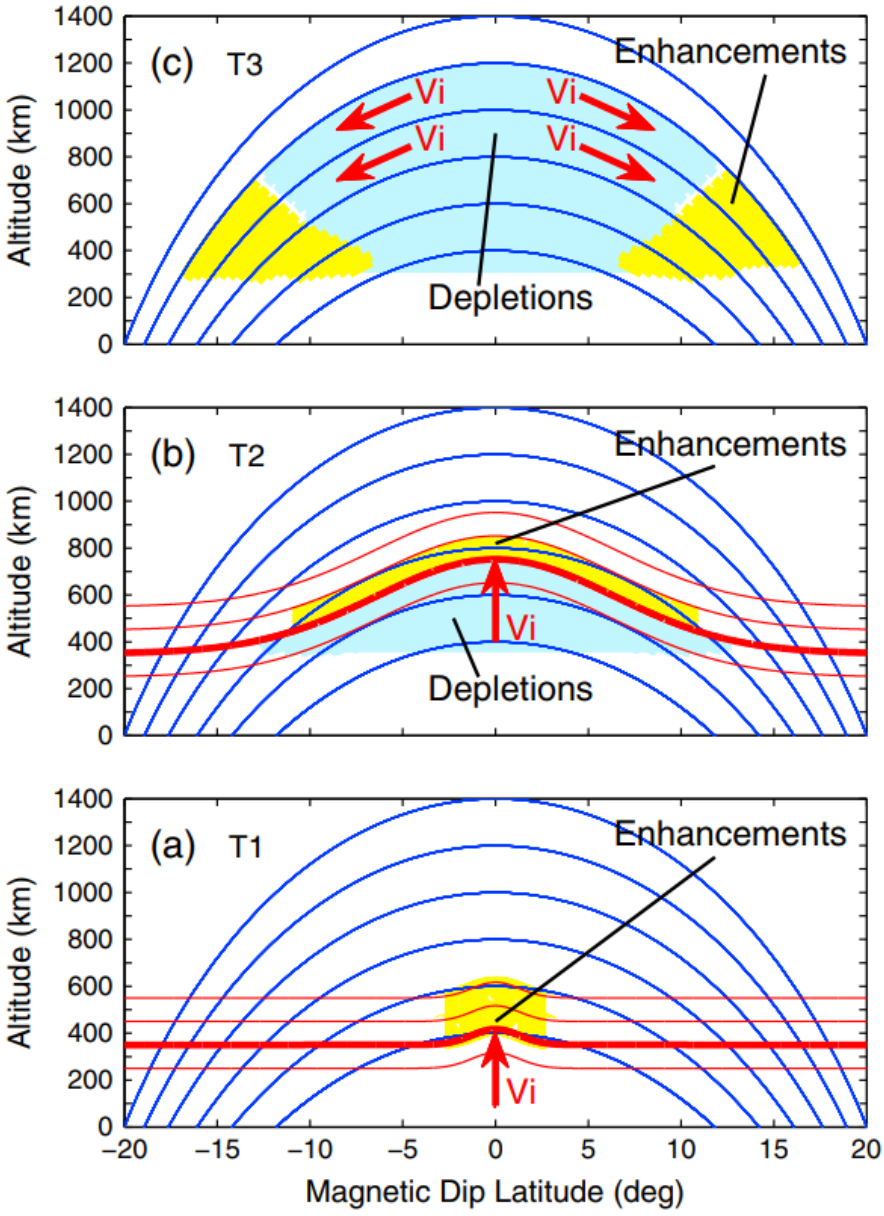

SOURCE: Huang et al. (2014).

When the Rayleigh-Taylor instability starts to grow, an eastward polarization electric field is generated and drives the plasma to move upward. Figure 2.15(a) rep-

resents the early stage of the Rayleigh-Taylor growth during which the eastward polarization electric field is developing. Because the $\mathbf{E}\times\mathbf{B}$ drift moves the F layer upward, the plasma density above the undisturbed F peak altitude is increased. Therefore, at the early stage of the Rayleigh-Taylor growth, plasma density enhancements occur in the topside F layer over the magnetic equator, as denoted by the yellow shading in Figure 2.15(a).

Figure 2.15(b) represents the intermediate stage of the formation of a plasma bubble. As the Rayleigh-Taylor instability continues to grow, a depleted region (or a plasma bubble) forms near the magnetic equator. Note that just above the upper boundary of the depleted region, the plasma density is still increased. The eastward polarization electric field inside the depleted region drives plasma particles to move upward and causes the plasma density enhancements over the depletions (KRALL et al., 2010). At this intermediate stage, plasma enhancements occur at higher altitudes, and plasma depletions occur at lower altitudes. Both plasma enhancements and depletions can exist over a relatively large latitudinal coverage.

Figure 2.15(c) represents a fully developed plasma bubble. At this late stage of bubble evolution, the plasma depletions have risen to the topside F-region but also exist at low altitudes, as shown in the simulations of Krall et al. (2010). The depletions extend to $10^o - 20^o$ magnetic latitudes along the magnetic field lines, as depicted by the blue shading. When plasma particles are moved by the $\mathbf{E}\times\mathbf{B}$ drift to a high altitude over the magnetic equator, they are driven by the gravitational force to flow down the magnetic field lines. The downward field-aligned plasma flow is depicted by the red arrows in Figure 2.15(c). The plasma particles accumulate at the location where the downward gravitational force is balanced by the upward diffusive force.

In other words, plasma enhancements form as the result of a balance between the gravitational and diffusive forces. The late stage of the bubble evolution is characterized by a depleted region at low latitudes, as denoted by the blue shadings, and plasma enhancements at higher latitudes, as denoted by the yellow shadings.

3 INSTRUMENTATION

3.1 Airglow and the ionosphere

The upper atmosphere of the Earth (above 80 km) is a rather rarefied gas medium whose basic components are atomic and molecular nitrogen and oxygen, along with hydrogen and helium. The so-called small components, such as nitric oxide NO, carbon oxide CO, carbon dioxide CO_2, nitrous oxide N_2O, vapors of water H_2O, ozone O_3, nitrogen dioxide NO_2, and metastable atoms and molecules, are important for the photochemistry, energetics, and emissions of the upper atmosphere. The ionizing solar ultraviolet radiation gives rise to numerous photochemical processes in the atmosphere which induce the airglow. This glow persists both in the daytime and at night, its intensity varying within considerable limits (KHOMICH et al., 2008).

Observations of the morphology and time evolution of large-scale airglow depletions and small-scale airglow enhancements using an all-sky imager in the OI 630.0 nm emission are very useful for studying the mechanisms related to the development and dynamics of F-region plasma irregularities. At tropical latitudes, the dissociative recombination of O_2^+ in the F-region is the dominant process for producing the excited oxygen atoms that give rise to the OI 630.0 nm nightglow. The major chemical reactions that generate the OI 630.0 nm airglow emission in the F-region are as follows (GARCIA et al., 1997):

$$O^+ + O_2 \rightarrow O_2^+ + O \tag{3.1}$$

$$O_2^+ + e \rightarrow O + O^*(^1D) \tag{3.2}$$

$$O^*(^1D) \rightarrow O + hv(630nm) \tag{3.3}$$

It is considered that production of $O(^1D)$ by dissociative recombination of NO^+ is unimportant (DALGARNO; WALKER, 1964). Therefore, the production of the OI 630.0 nm emission depends on the molecular oxygen density $[O_2]$ and the oxygen ion density $[O^+]$. The oxygen ion density $[O^+]$ is approximately equal to the electron density in the F-region. The height of the F-layer peak electron density occurs around $350 - 400km$, while the molecular oxygen density $[O_2]$ increases with decreasing height. Thus, the OI 630.0 nm emission peak occurs in the bottomside of the F-region around $220 - 300$ km. When the F-layer moves downward, the OI 630.0 nm emission is enhanced, so that the OI 630.0 nm emission intensity is a sensitive indicator of F-region vertical motions and plasma density variations (PIMENTA et

al., 2007).

The study of the upper atmosphere has drastically become more interesting since the invention of the All-Sky Imager. The understanding of the dynamics of this region has led to the observations of several physical phenomena in the upper atmosphere. The All-Sky Imager is an instrument to capture the atmospheric state by taking pictures. The imager used in measuring aeroluminescence (airglow) emissions is composed of an optical system and a Charge Coupled-Device (CCD) camera, which is capable of detecting variations in the intensity of airglow layers thereby recording them through images. The airglow emissions are important in studying ionospheric plasma irregularities and describing parameters of the phenomenon; size, altitude, drift velocity, temperature, and wave activities in the region of observation. The irregularities observed in the airglow emission are due to instability conditions of the ionospheric plasma which have been attributed to various other phenomena such as atmospheric gravity waves which are caused by restoration force between gravity and pressure gradient.

3.2 All-Sky Imager

3.2.1 Description of the all-sky imager

Figure 3.1 - Image of the all-sky imager at ZF-2. The imager has a CCD camera (130^o field of view), high resolution of 2048 $\times$ 2048 but binned down to 1024 $\times$ 1024 resolution to improve the signal-to-noise ratio. Developed at INPE by Alexandre A. Pimenta.

SOURCE: Author.

All-Sky Imager is an optical instrument used in the study of Luminescence (aurora and airglow). The instrument measures the intensity variation of different luminescence emission layers. As shown in Figure 3.1, the component of the All-Sky Imager used in this work is composed primarily of an optical system and a CCD camera, the "All-Sky" imager is able to detect variations of the night-time aeroluminescence and record them through images from digital files. The equipment can record complete images of the sky in several aeroluminescence emissions, monitoring in real-time the variations that occur in aeroluminescence.

The system has a fisheye lens that obtains a complete image of the entire sky, for the study site. After, the light goes through an optical system (telecentric lenses), and in sequence by a wheel of filters, where the system has the ability to change filters automatically via computer. Finally, the image after passing through the filters passes through another system (lenses) that rebuilds the image on the charge-coupled device (CCD).

3.2.2 Principle of Operation of All-Sky Imager

Figure 3.2 - Optical system of All-Sky Imager.

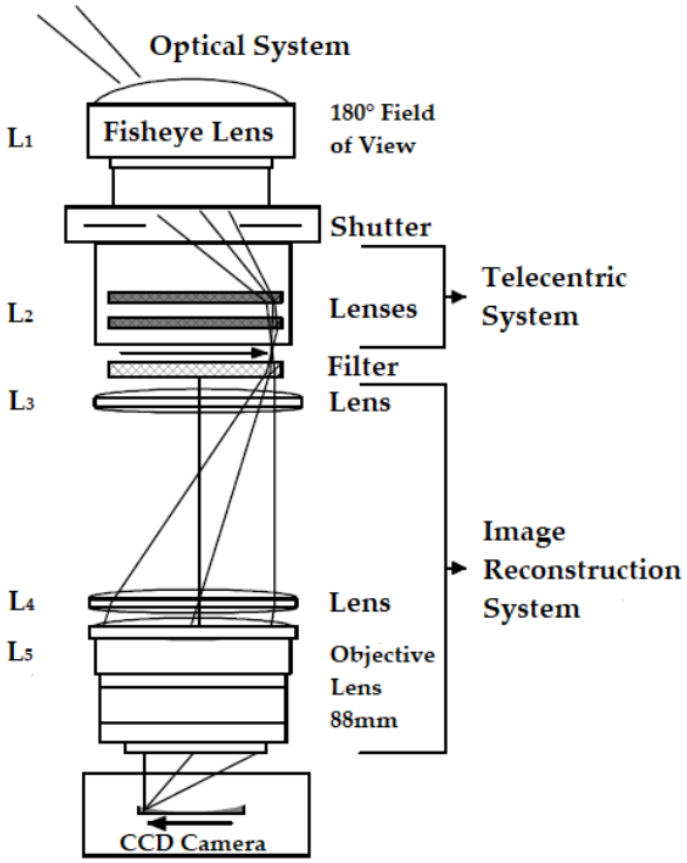

SOURCE: Wrasse (2004).

Consider the Figure 3.2, the incident light on the optical system through the fisheye lens (L_1) produces an image, called the primary image, which is equal to the size of the interference filter. The set of telecentric lenses (lens L_2) causes the rays of light from the main plane of the fisheye lens to be parallel to the axis of the optical system. To make this possible, the focal length of these lenses (L_2) must be equal to their distance from the main plane of the fisheye lens (L_1). The optical path is then encumbered by interference filters (which are five in all). Table 3.1 shows the main characteristics of the interference filter, the wavelength of the photochemical species, and the spatial location of the corresponding emission layers. The filtered light component then passes through another lens system (L_3, L_4 and L_5) where the size of the primary image is reduced to the size of the CCD detector without any

loss of light. Since the size of the CCD detector used is $24.6 \times 24.6mm$, the image should be reduced by a factor of three (3) over this area. Thus, the distance between the primary image formed in the interference filter and the main plane lens (L_4) should be three times the focal length of the lens L_5. This lens refers from the pupil of the entrance of the lens to the objective lens L_5, and its focal length is equal to the effective distance between the lens L_3 and this pupil. The primary image formed at the position of the filter is focused through the L_4 lens in the L_5 lens. Therefore, the light incident on the fisheye lens is projected throughout the area of the CCD detector, so that there is a better use of the entire optical system (WRASSE, 2004).

Table 3.1 - Filter characteristics and average height of all-sky imager at ZF-2.

Filter	Wavelength(nm)	Band (nm)	Height (km)
Background	598.50	2.0	95
OI	557.7	2.0	96 and 250
OI	630.0	2.0	250
Na	589.0	2.0	90

SOURCE: Author.

Three different all-sky imagers were used in this research.

- All-Sky imager 1 was the first all-sky to be installed at Cachoeira Paulista (CP: $22.7^o, 45^oW$) and operated from 1987 to 2000.
- All-Sky imager 2 was installed at the same location with the all-sky imager 1 but operated for a period of two years (October, 1998 - July, 2000). The high solar activity (HSA) data used in this work is obtained from this imager.
- All-Sky imager 3 (ZF-2) is installed at ZF-2, Amazon region of Brazil. And the low solar activity (LSA) data used in this work is obtained from this imager.

3.2.3 All-Sky imager 1 (CP)

The imaging system uses a 10 cm diameter interference filter in the OI 630.0 nm emission with a bandwidth of 1.35 nm and records intensified monochromatic images

on 35 mm film using a conventional single-lens reflex camera. The images were recorded at an interval of 20 min with 40 s exposure time. An important piece of information on the three imagers is the relationship between zenith angle and image size. A zenith angle of 90^o encompasses $\pm 16^o$ latitude/longitude from the zenith, which is equivalent to a horizontal diameter of approximately 3600 km through the zenith at 300 km altitude. Figure 3.3 shows the field of view of this system together with other relevant information.

The OI 630.0 nm emission, which comes from an altitude of about 250-300 km, can be used to map a depleted region along the field line to its height above the magnetic equator. The OI 630 nm emission is produced in the bottomside of the F-region by the dissociative recombination process ($O_2^+ + e \rightarrow O + O^*(^1D)$), followed by $O^*(^1D) \rightarrow O + hv(630nm)$ and has been widely used to monitor important ionospheric processes at F-region heights.

Figure 3.3 - Field of view at 75^o and 90^o zenith angles at 300 km for OI 630 nm all-sky imaging system at Cachoeira Paulista (22.7^oS, 45^oW). Also shown are relevant geomagnetic parameters and the location of diagnostic instrument at Fortaleza (ionosonde) and Cachoeira Paulista (ionosonde and GOES-3 satellite radio beacon F-region intersection point).

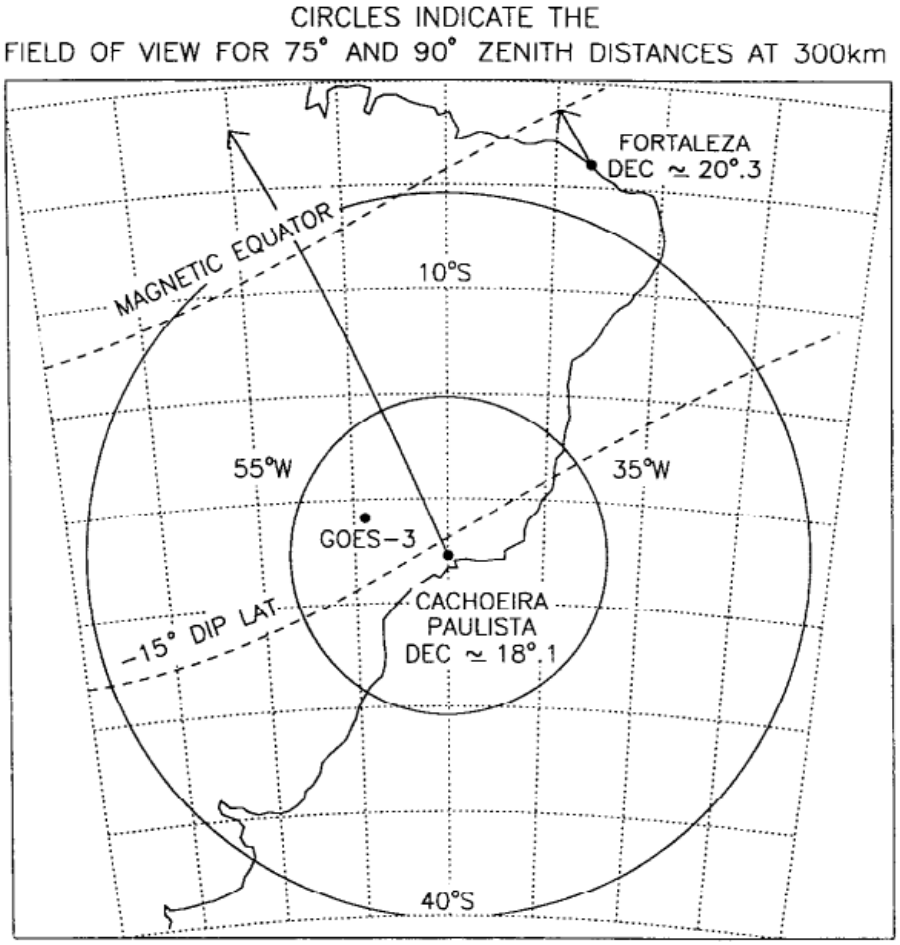

SOURCE: Sahai et al. (1994).

3.2.4 All-Sky imager 2 (CP)

In October 1998 a new all-sky imaging system with a CCD camera was put in operation at Cachoeira Paulista, in collaboration with the Utah State University. This new all-sky imager has a CCD detector and the images obtained from it have higher resolution when compared with the previous imager. The CCD imager consists of a large area (6.45 cm^2), high-resolution, 1024×1024 back-illuminated array with a pixel depth of 14 bits. The images were binned on-chip down to 521×512 resolution to enhance the signal-to-noise ratio and were recorded at intervals of 7 min with a

90 s exposure rate. The Figure 3.4 shows a sample of a plasma blob image recorded by this imager on April 06, 2000, at 21:36 LT. The center of the image corresponds to the location of the observing site.

Figure 3.4 - OI 630.0 nm emission all-sky image obtained at Cachoeira Paulista on April 06, 2000, at 21:36 LT, with its respective field of view (considering an emission height around 275 km).

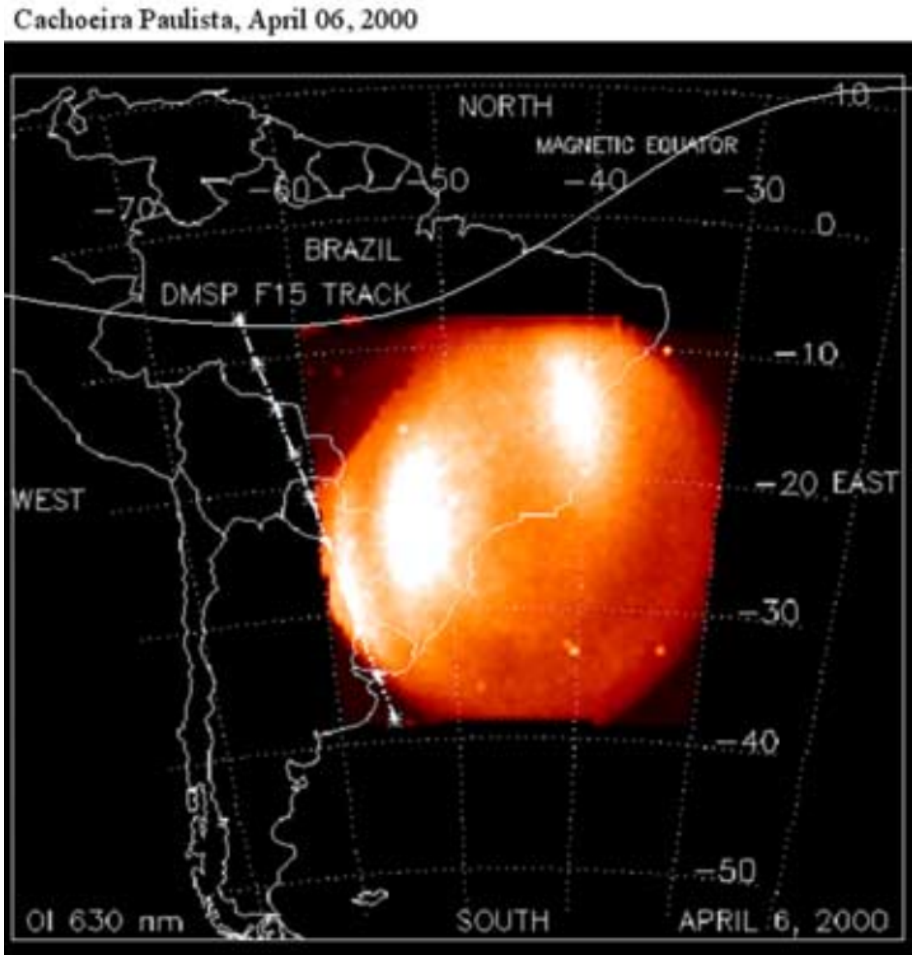

SOURCE: Pimenta et al. (2007).

3.2.5 All-Sky imager 3 (ZF-2)

Lastly, the observations of the OI 630 nm nightglow emission intensity using a wide-angle imager with a CCD camera (130^o field of view) have been carried out at the Amazona region, ZF-2 (2.58^oS, 60.22^oW), Brazil, since July 2015. The CCD imager

Figure 3.5 - One of the OI 630.0 nm emission all-sky image of plasma blobs (the bright region) obtained at ZF-2 on October 28, 2019, at 00:17:23 LT.

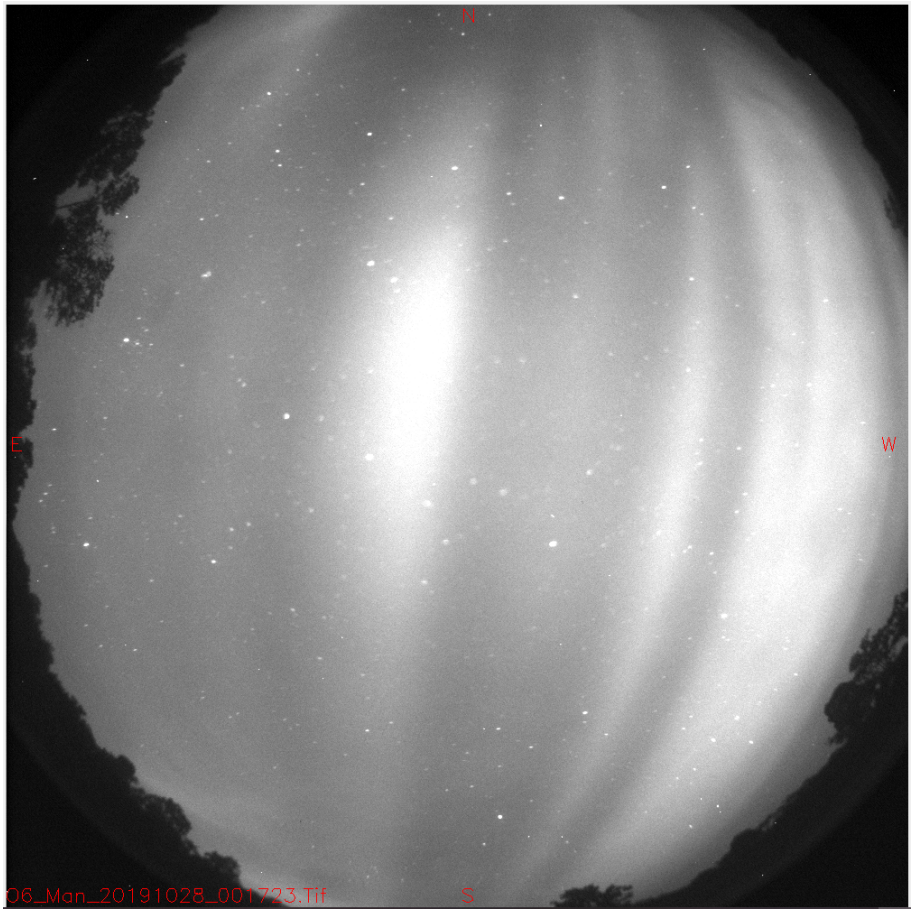

SOURCE: Author.

consists of a large area (6.45 cm^2), high resolution, 2048 × 2048 back-illuminated array with a pixel depth of 14 bits. The images were binned on-chip down to 1024 × 1024 resolution to enhance the signal-to-noise ratio and are recorded at intervals of 7 minutes with 90 seconds exposure time rate. The Figure 3.5 shows a sample of a plasma blob image observed by this imager at ZF-2 on October 28, 2019, at 00:17:23 LT. The center of the image corresponds to the location of the observing site.

3.3 Ionosonde

Complementary data from ionosondes (at CP) will be used to investigate the behavior of ionospheric parameters at the time of occurrence of plasma blobs. A Digisonde 256 (DGS256), located at the same site as the all-sky imager at CP, will be used to obtain vertical sounding data of the ionosphere. The Digisonde can be operated in

a number of modes, and during the events reported here was at vertical incidence. The vertical ionograms were automatically scaled by using the ARTIST inversion algorithm to obtain the true height profile and subsequently were checked manually and rescaled where necessary to remove obvious errors. Determining true height profiles by inversion of ionogram traces is a complicated procedure in which many factors, such as underlying ionization and E-F valley, must be taken into account. Consequently, the determination of a general procedure of error determination is not detailed in this work. Nevertheless, we can put limits on the errors in hmF2. Such errors arise primarily from experimental measurement errors in virtual height (minimum virtual height) and f0F2 (peak F-region frequency) and from the assumptions made concerning the base height of the ionosphere and E-F valley.

3.4 SWARM satellites

In this work, supplementary results were obtained from the SWARM constellation composed of three (A, B, and C, Figure 3.6) identical satellites, which were launched on 22 November 2013 (see SWARM Mission Webpage). The Electrical Field Instrument consists of two components: the Langmuir Probe (LP) and the Thermal Ion Imager (TII). The main purpose of the LPs is to provide estimates of the density and electron temperature, N_e and T_e, in the plasma around the satellites, as well as the electric potential of the spacecraft V_s. The actual probes are two spheres mounted on about 10 cm long stubs at the Earth-facing front edges of the satellites. Measured on board are probe currents and admittances as a response to a time varying bias that the LP electronics applies to the probes. On ground Ne, Te, and Vs are then estimated from the measured currents and admittances, the results are the main LP L1b product. All three satellites have near-circular orbits. A and C are orbiting at 87.35^o inclination and at similar altitudes of $\approx$ 460 km but B is orbiting at 87.75^o inclination and at an altitude of $\approx$ 530 km. The period of the spacecraft is fifteen (15) orbits daily. Moreover, only the electron density and electron temperature data from the A and C spacecraft were studied in this work. The data are available on a daily basis (00:00:00 to 23:59:59 UT) (see SWARM Mission Webpage).

Figure 3.6 - ESA SWARM satellites (A, B, and C).

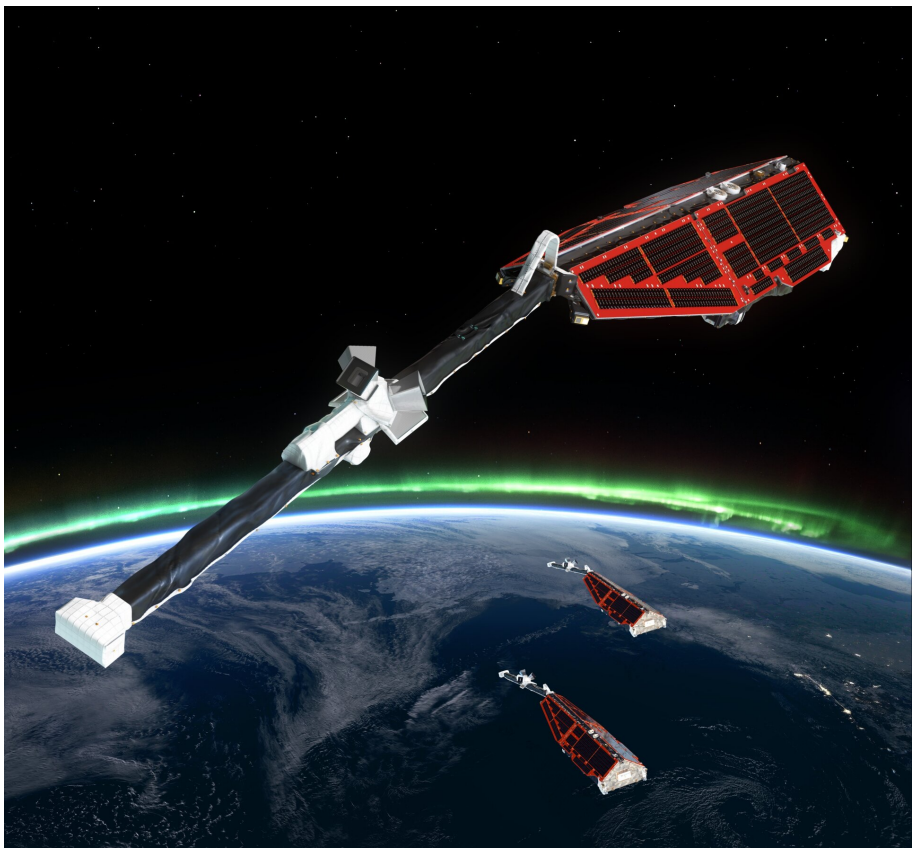

SOURCE: Adapted from SWARM mission page (2013).

4 DATA PROCESSING AND ANALYSIS

4.1 Data description

One of the first steps is to create an archive of periods of observation and occurrence of plasma blobs with and without plasma bubbles from OI 630.0 nm data for low and high solar activity (LSA and HSA respectively). Complementary data such as ionosonde and SWARM Constellation Satellites (A and C) is used to study these phenomena using some of the interesting cases from the first approach. The behavior of ionospheric parameters such as hmF2, foF2, and h'F are investigated during the occurrence of plasma blobs and plasma bubbles. The electron density, Ne, and electron temperature, Te, from satellites are also used to study the plasma blobs. The signature of plasma bubble and plasma blob has been reported as a decrease and increase in plasma density, respectively. In order to study the occurrence pattern of plasma blobs in the tropical region of Brazil, the airglow OI 630.0 nm emissions data at an altitude of about 300 km is used.

An existing IDL algorithm was used to animate the raw 'tif' and 'pmi' data from each station (Cachoeira Paulista and ZF-2) for high solar activity (HSA) and low solar activity (LSA).

Table 4.1 - OI 630 nm data Stations for HSA and LSA.

Stations Year	Geo. location (^{o})	Dip latitude (^{o})	Solar cycle
Cachoeira Paulista 1999-2000	22.7^oS, 45^oW	15.8^oS	HSA
Manaus, ZF2 2019	2.58^oS, 60.22^oW	6.50^oN	LSA

SOURCE: Author.

Figure 4.1 - The location (in red) of the stations on the South America map from Google Map.

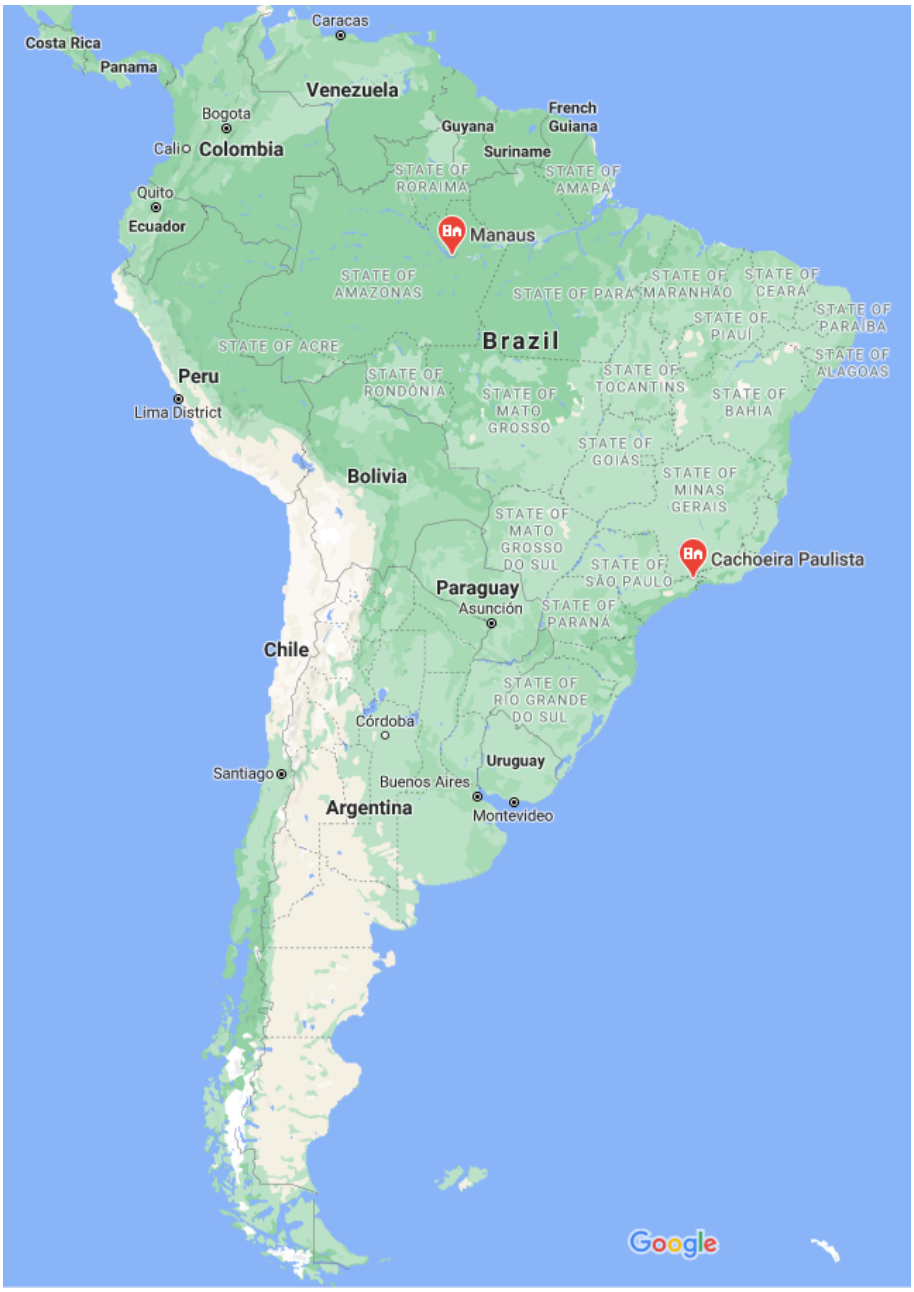

SOURCE: Google Map (2021).

4.2 Irregularities detection

The wide-angle imaging technique offers a unique capability to characterize simultaneously the morphology and dynamics of depleted flux tubes over regions spanning

several kilometers. Figure 4.2 presents a geomagnetic dipole field model along the magnetic meridian of Cachoeira Paulista. Airglow depletions attributed to a typical emission height of 300 km (MENDILLO et al., 1985) can extend from the magnetic equator at the northern edge of the field of view to a dip latitude of 35^o at the southern edge of the field of view. Given the geomagnetic flux-tube nature of the plasma depletions that account for the reduced airglow. The airglow signatures at 300 km can be used to map the depletion back along the field to their height above the geomagnetic equator. This is referred to as the 'apex height' of the depletion and has been used to study the altitude/latitude extent of the instability processes (ANDERSON; MENDILLO, 1983; MENDILLO; TYLER, 1983; ROHRBAUGH et al., 1989). Figure 4.3 gives an overlay pattern for CP images in which the apex altitudes are given in kilometers. Note that airglow depletions extending to the southern edge of the field of view relate to plasma depletions (bubbles, plumes) that extend to beyond 2500 km above the magnetic equator.

Figure 4.2 - A geomagnetic dipole field model along the magnetic meridian of Cachoeira Paulista. Airglow depletions at 300 km can extend from the magnetic equator near the northern edge of the field of view to a dipole latitude of 35^o at the southern edge.

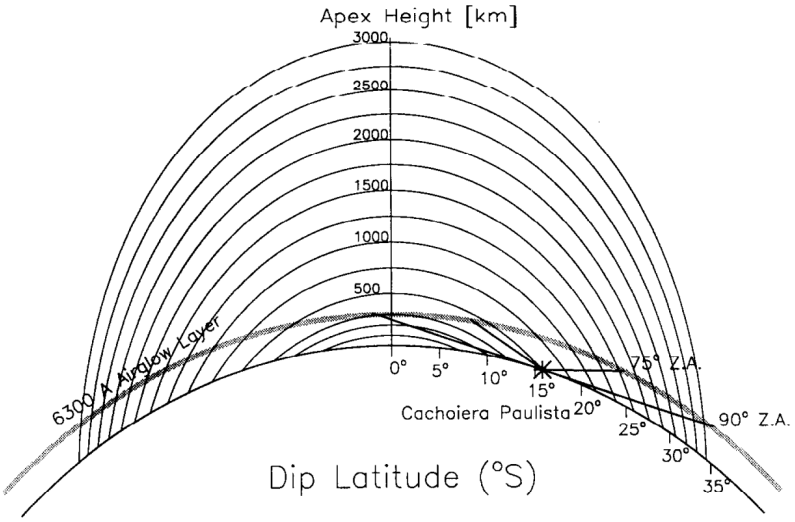

SOURCE: Sahai et al. (1994).

Figure 4.3 - An image overlay pattern where the depletions observed can be translated into altitudes above the magnetic equator (dotted line) with the assumption that the altitude of the background 630.0 nm is at 300 km. When the depletion continues beyond the southern edge of the image, the depletion is assumed to correspond to altitudes greater than 1500-2500 km above the magnetic equator. The dashed line corresponds to 75^o from the zenith.

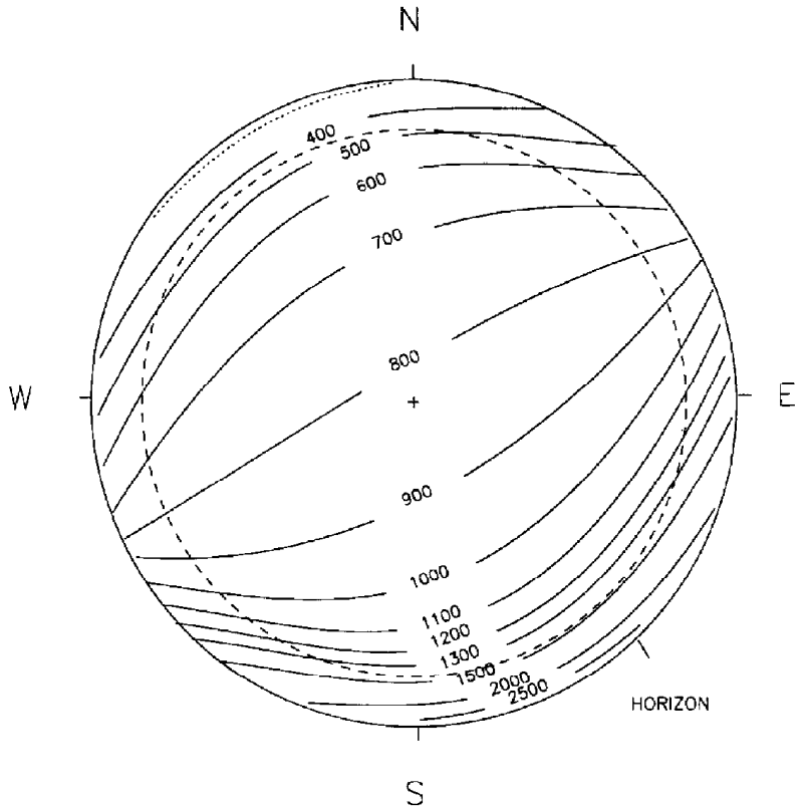

SOURCE: Sahai et al. (1994).

4.2.1 Plasma blobs detection

Plasma blobs are ionospheric plasma irregularities with plasma density enhancement and generally take place along $\pm 15^o$ geomagnetic latitude. Using data from the Hinotori satellite, Oya et al. (1986) reported the first observations of localized regions of plasma density enhancements in addition to plasma depletions in the nighttime tropical F-region. Their statistical study showed that the occurrence probabilities of plasma depletions and plasma blobs *appear to be complementary to each other*, and the occurrence region of the plasma blobs is limited to the adjacent parts of the plasma bubble occurrence region (WATANABE; OYA, 1986). However, some investigators have observed plasma blobs in the absence of plasma bubbles (CHOI et al.,

2012). This section explains how the plasma blobs were identified, both associated with/without plasma bubbles.

At the upper atmosphere, the dissociative recombination of O_2^+ in the F-region is the dominant process for producing the excited oxygen atoms that give rise to the OI 630.0 nm nightglow. The major chemical reactions that generate the OI 630.0 nm airglow emission in the F-region are as follows (GARCIA et al., 1997):

$$O^+ + O_2 \rightarrow O_2^+ + O \tag{4.1}$$

$$O_2^+ + e \rightarrow O + O^*(^1D) \tag{4.2}$$

$$O^*(^1D) \rightarrow O + hv\ (630nm) \tag{4.3}$$

Thus, plasma blobs have been studied as the intensity enhancements produced through the O_2^+ dissociative recombination process. In this work, plasma bubbles appear as a **dark region** in the OI 630.0 nm emission while plasma blobs appear as a **bright white region** in the OI 630.0 nm emission. However, not all bright regions seeing in the observation are considered to be plasma blobs. The filtration was carried out by visualizing the equivalent background data using the date and time of the suspected plasma blobs in the OI 630.0 nm emission for comparison as shown in Figure 4.4. This implies that if the pattern observed to be plasma blobs in the OI 630.0 nm was absent on the background data (see Figure 4.4C) then there is a tendency of it being plasma blobs because plasma blobs occur at higher altitude as shown in Table 3.1. More so, the complementary satellites and ionosonde data are to be used to study the behavior of electron density inside the plasma blobs. In Figure 4.4, note that the plasma blobs appeared only in the OI 630.0 nm and OI 557.7 nm, which are representative of F-region emissions by the dissociative recombination process.

Figure 4.4 - (a): Plasma blobs (the bright region) and plasma bubbles (dark band region) at OI 630.0 nm and OI 557.7 nm emission on March 2, 2019, at 00:22:23 LT and 00:29:08 LT, respectively. While the phenomena are absent on the BG data at 00:20:08 LT. (b): The error observation of blob on October 7, 2019 as the structure suspected to be blob (on OI 630.0 nm and OI 557.7 nm emission) also appears on the background data (BG).

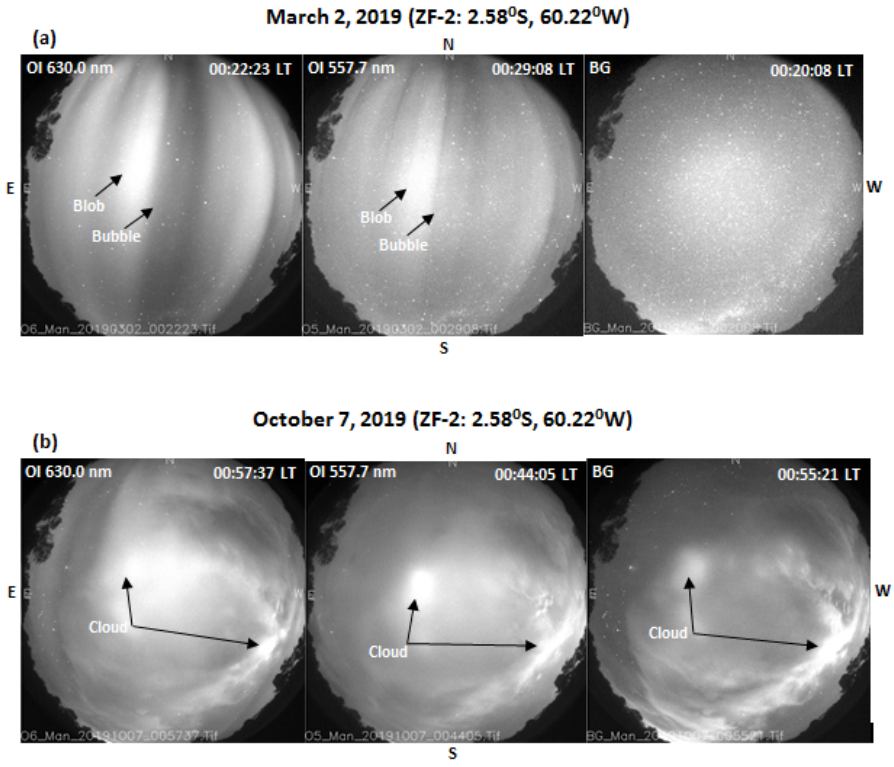

SOURCE: Author.

4.3 Data Analysis

4.3.1 Occurrence statistics

After the documentation of the hours of observation and occurrence for both the high solar activity (HSA) and low solar activity (LSA) data, the percentage of occurrence frequency for each month was computed using Equation 4.4 below:

$$\%\ occurrence = \frac{hours\ of\ occurrence}{hours\ of\ observation} \times 100 \tag{4.4}$$

For instance, in February 2019, there were 24 nights of all-sky imager observations. So, we analyzed the data for each day for the month and recorded the hours of observation (the total hours of operation for the all-sky imager) and the hours of occurrence (the total hours of plasma bubbles or blobs appearance) then apply Equation 4.4. This was done for the nocturnal, seasonal, and solar cycle occurrence frequency of plasma blobs and plasma bubbles.

4.3.2 Linearization technique

In this work, the East-West and North-South extension of selected plasma blobs were estimated by using the linearization method presented by Garcia et al. (1997). This is basically done by converting the pixels on the CCD covered by the plasma blobs into kilometers using an IDL algorithm.

A CCD (charged-coupled device) detector is a solid-state image sensor arranged in the form of a square array of regularly spaced rows and columns. The number of rows and columns defines the size of the CCD sensor, which can range from a few millimeters to tens of millimeters. Figure 4.5 below illustrates the structure of a CCD sensor. The CCD detector used mostly has 1024×1024 pixels, and each pixel has $20 \times 20 \mu m$. The resolution of a CCD camera is defined by the number and the quality of the pixels.

Figure 4.5 - Schematic diagram of an all-sky imager CCD.

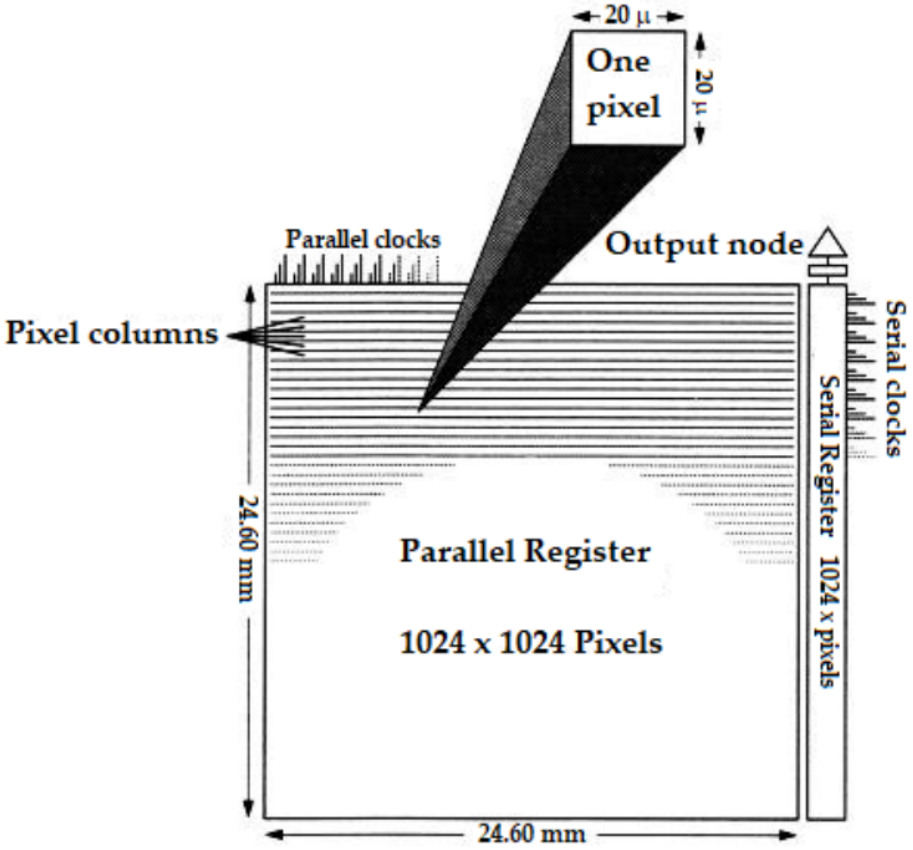

SOURCE: Wrasse (2004).

The image displayed on the CCD of the all-sky imager is compressed and curved at low elevation angles as appears on the Figure 4.6. The linearization method provided an opportunity to estimate the geographical extent and time history of the plasma blobs. The application of the linearization method involves basically few steps listed below:

- compilation of OI 630.0 nm emission data;
- selection of images with occurrence of plasma blobs;
- conversion of pixels covered by the plasma blobs into kilometers

To obtain an estimate of zonal drift velocities from the imaging data, we first scan the optical images from west to east to obtain a cross-section of the brightness

patterns for each plasma blobs. Then, these cross-sectional scans are subjected to a correlation analysis leading to the best fit spatial shifts required to match the time between images. A succession of such space and time shifts leads to a zonal velocity versus local time relation for the blobs and bubbles. Therefore, if we know the distance covered by the plasma blobs and the time taken, we can calculate the drift velocity of the structure by using the equation Equation 4.5.

$$Drift\ velocity = \frac{distance\ covered}{time\ taken} \tag{4.5}$$

Consider the application of the linearization method to the plasma blobs observed on March 2, 2000, at Cachoeira Paulista as shown in the Figure 4.6:

The linearized image resolution was $512 \times 512\ km$. The dimension of the linearized image gives $14.2 \times 14.2\ cm$. The image was grid to know the exact starting point of the plasma blobs and stopping point.

At $02:02:43$ UT - the plasma blob was located at $72\ km$ with the reference point of $0km$;

At $02:24:08$: the ending point of the plasma blob was at $126\ km$

Hence, the total distance covered by the plasma blobs was $126\ km - 72\ km = 54\ km$ and the time taken was $0.36hr$. Using Equation 4.5 we have the drift velocity to be

$$Drift\ velocity = \frac{54\ km}{0.36\ hr} = 150\ km/hr\ (41.7\ m/s)$$

Figure 4.6 - On March 2, 2000 (CP), plasma blobs associated with plasma bubbles were observed and the linearization method was carried to estimate its drift velocity. Its drift velocity was estimated to be 41.7 m/s.

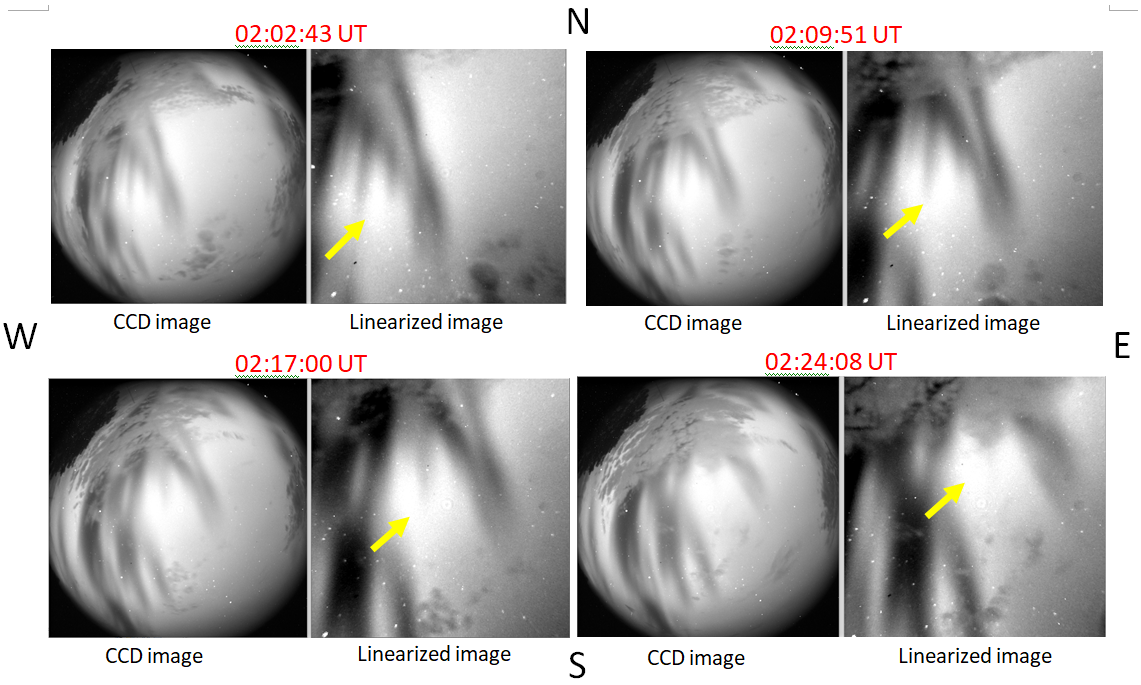

SOURCE: Author.

4.3.3 Pearson correlation analysis

The Pearson correlation coefficient is a measure of the strength of a linear relationship between two variables and is denoted by r (SOONG, 2004). In this work, we applied Pearson correlation to some of the analyses which required us to study the linear relationship between the variables of concern. For instance, this analysis was applied to the plasma blobs and plasma bubbles' duration of occurrence. Also, it was applied to the electron density measurements from sensors on board SWARM satellites (A and C). The Pearson correlation is carried out using the Equation 4.6 theoretically but Python algorithm was used on the data:

$$r_{XY} = \frac{\sum_{i=1}^{n}(X_i - \bar{X})(Y_i - \bar{Y})}{\sqrt{\sum_{i=1}^{n}(X_i - \bar{X})^2}\sqrt{\sum_{i=1}^{n}(Y_i - \bar{Y})^2}} \tag{4.6}$$

where X and Y denotes the variables;

The Pearson correlation coefficient, r, can take a range of values from +1 to -1. A value of 0 indicates that there is no association between the two variables. A value greater than 0 indicates a positive association; that is, as the value of one variable increases, so does the value of the other variable. A value less than 0 indicates a negative association; that is, as the value of one variable increases, the value of the other variable decreases (SOONG, 2004).

4.3.4 SWARM constellation

Figure 4.7, the electron density, Ne, from A and C satellite (version number 0301) was investigated, when the satellites simultaneously passed over near the all-sky imager location ($2.58^oS,\ 60.22^oW$), on the day that plasma blobs and plasma bubbles were observed by the all-sky imager. We considered a range of latitude (10^oN to 10^oS) because of the geographical latitude and longitude covered by the all-sky imager at about 300 km. Also, the range of latitude was selected so as to observe the latitudinal extension of both the plasma blobs and plasma bubbles. The inclination of the spacecraft is a unique opportunity that enables us to study plasma blobs in the equatorial region. Considering the day that the plasma blobs were observed on the all-sky imager, the satellite data at the close range of time was obtained through VRE (Virtual Research Environment for SWARM mission) platform (see Pedrosa and Triebnig (2016) for more details). Then, each time the satellites passed over the stated latitudinal range was archived regardless of the longitude. And for every single time that the spacecraft passed over the geographical coordinates corresponding to the all-sky imager location, was selected; only once. Notice that all the variables measured by the satellites; Ne, latitude, and Longitude were timestamps. Hence, we studied the electron density and electron temperature behavior, at different geographical locations for that day, in comparison with the suspected plasma blobs associated with plasma bubbles.

Figure 4.7 - Screenshotted image, from Virtual Research Environment for SWARM mission, of A and C SWARM constellation satellites on March 2, 2019, at 21:34:10 - 21:39:23 LT passing over near the all-sky imager's location. The two satellites have 1.4^o separation in longitude.

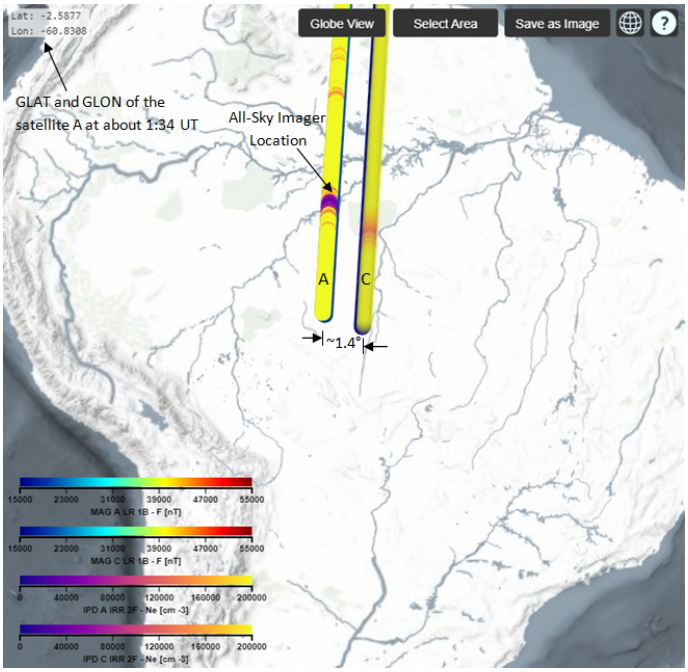

SOURCE: Author.

Figure 4.8 - On several occasions, the SWARM constellation path was observed on the field of view of all-sky imager at ZF-2 and one of the clearer ones was on March 10, 2019, at around 23:41:22 LT. The thin white line on the field of view is one of the satellites passing over the location of the all-sky imager.

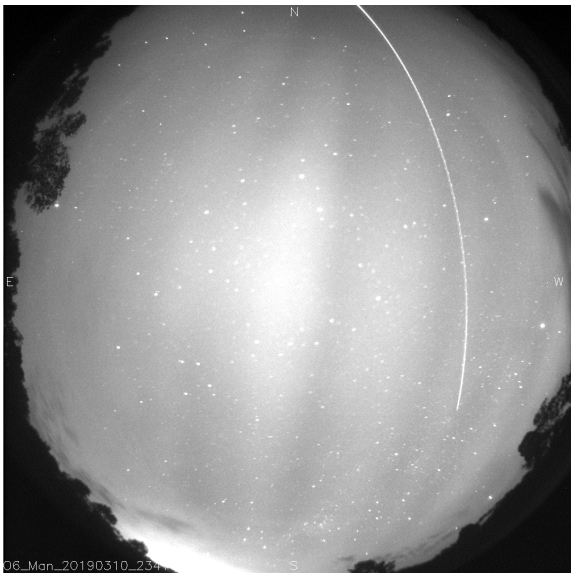

SOURCE: Author.

5 OBSERVATIONS AND RESULTS

In this chapter, we present the observations and the results obtained using the OI 630.0 nm emission, ionosonde, and satellite data over the tropical region (Cachoeira Paulista and ZF-2). The results are presented in five sections. In the first section, we discussed the plasma blobs variation such as the solar cycle, monthly, seasonal and nocturnal variations. The second section is about the plasma blobs features such as the physical dynamics, statistical results; correlation between the plasma blobs and plasma bubbles, temporal east-west and north-south extensions of the plasma blobs, merging and detachment of plasma blobs, etc. In the third section, ionosonde results are discussed. In the fourth section, plasma blobs associated with plasma bubbles observed by SWARM constellation satellites are discussed. And lastly, a blob observed by the first all-sky imager installed at Cachoeira Paulista in August 1987 is discussed in this work and the likely mechanism for the generation of plasma blob associated with plasma bubble is proposed.

Table 5.1 - Results of observations of OI 630.0 nm during high (HSA) and low (LSA) activities.

	HSA	LSA
Period	July 1999 - June 2000	Jan 2019 - Dec 2019
Average solar flux ($F10.7$)	173.9 $\pm$17.6	69.7 $\pm$1.7
Total hours of observation	500.16 hours	705.57 hours
Total hours of blob occurrence	25.93 hours (5.2%)	29.31 hours (4.2%)
Total hours of bubble occurrence	98.79 hours (19.8%)	112.08 (15.9%)
Blobs without bubbles events	1	None
Bubbles without Blobs events	4	11

SOURCE: Author.

Figure 5.1 - A sequence of OI 630.0 nm all-sky images obtained from 22:09:56 to 23:07:02 LT on the night of January 9, 2000, showing the evolution of plasma blobs (bright regions) at Cachoeira Paulista ($22.7^oS, 45.0^oW$).

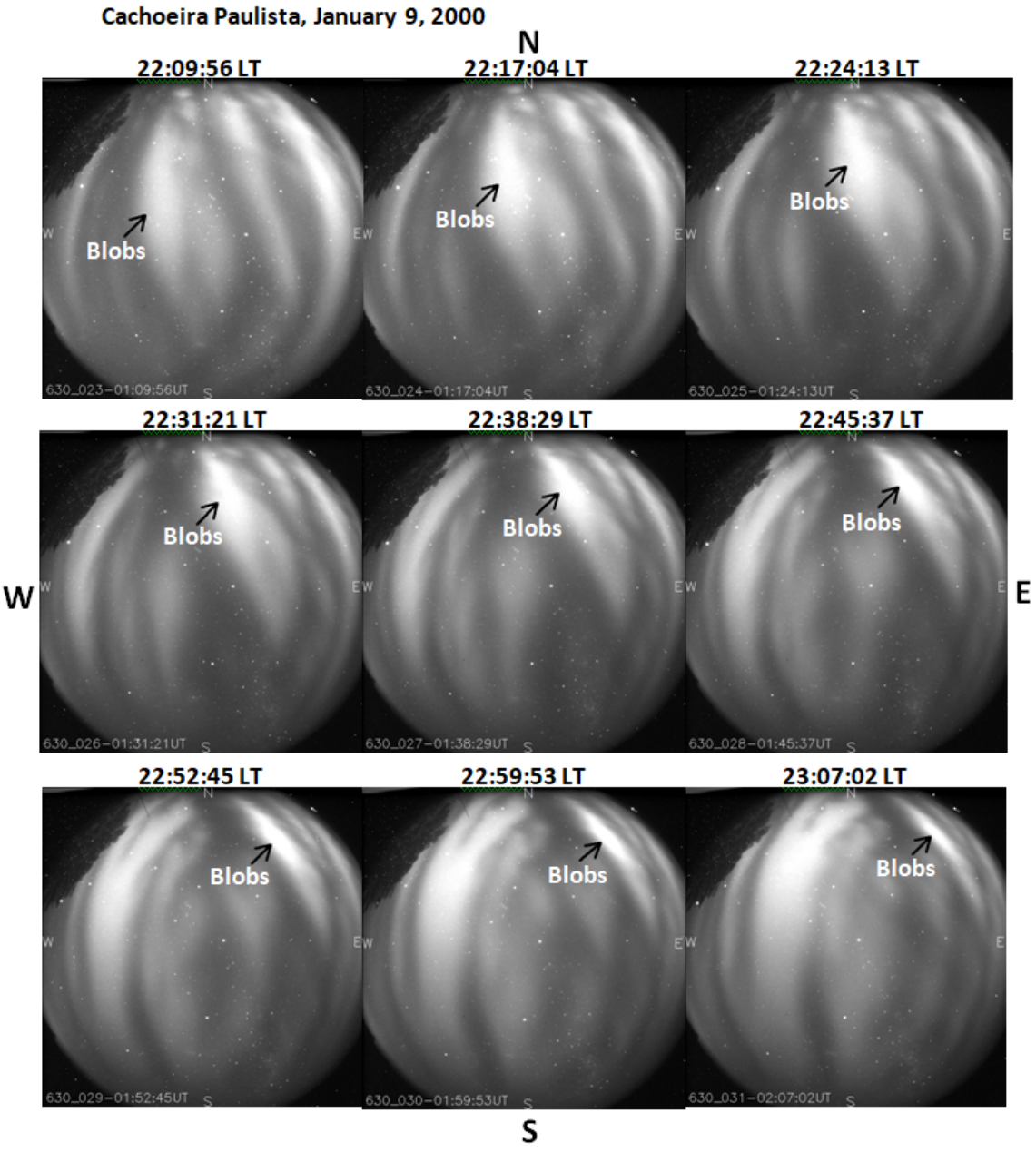

SOURCE: Author.

5.1 Seasonal variations

The statistical study of plasma blobs occurrence was carried out for the low solar activity (LSA, 2019) and the high solar activity (HSA, 1999-2000) in the tropical regions (CP: $22.7^oS, 45.0^oW$, and ZF-2: $2.58^oS, 60.22^oW$). The OI 630.0 nm emission data was analyzed using the method presented in chapter 4. Results from the OI 630.0 nm imaging observations carried out at ZF-2 during the periods January 2019 to December 2019 relating to low solar activity (LSA; average 10.7 cm solar flux $< 73 \times 10^{-22} Wm^{-2}Hz^{-1}$) and July 1999 to June 2000 relating to high solar activity (HSA; average 10.7 cm solar flux $> 137 \times 10^{-22} Wm^{-2}Hz^{-1}$) are presented and discussed in this work. Observations available during the hours 19:00 LT to 05:00 LT have been used in this study. Figure 5.1 shows a typical example of the raw plasma blobs observed on January 9, 2000, by all-sky imaging in the OI 630.0 nm. The center of the images corresponds to the location of the station - Cachoeira Paulista. The bright regions are associated with intensity enhancements in OI 630.0 nm and OI 557.7 nm, which are related to F-region ionization enhancements.

5.1.1 Plasma blobs in LSA

Figure 5.2(A) shows the monthly occurrence pattern of plasma blobs. Three main patterns are evident: (1) January through March, (2) April through July, and (3) August through December. In the first pattern, the occurrence of plasma blobs seems to be steady i.e there is high likelihood of observing plasma blobs during these months. In the second pattern, and the winter period in southern hemisphere, there is approximately zero occurrence probability of plasma blobs. In the third pattern, the occurrence frequency of plasma blobs increases gradually from (late) August through November which later decreases. In this pattern, the rate of change of occurrence frequency of plasma blobs is gradual and monotonic in nature unlike in the first pattern (which is almost steady). For the whole patterns, two peaks can be clearly spotted: March and November. Sahai et al. (1994) reported May-August as the period of low-spread and October-March as the spread F season. In LSA, every single plasma blob observed was associated with plasma bubbles. During LSA, there was 705.57 hrs of observation of OI 630.0 nm and plasma blobs occurred for total hours of 29.31 hrs; approximately 4%.

Similarly, Figure 5.2(B) shows the monthly occurrence pattern of plasma bubbles. It also displays typically three patterns: (1) January through April, (2) May through July, and (3) August through December. In the first pattern, the occurrence frequency increases rapidly from January through March and later decreases rapidly

in April. In the second pattern, the occurrence of plasma bubbles is zero. The winter period in southern hemisphere is May through August and this implies that the occurrence of plasma bubbles in winter is approximately zero. In the third pattern, the occurrence frequency increases from August through October and later decreases in November and December. In LSA, there were eleven (11) events of plasma bubbles without plasma blobs. During LSA, there was 705.57 hrs of observation of OI 630.0 nm and plasma bubbles occurred for total hours of 112.08 hrs; approximately 16%.

Figure 5.2 - The ZF-2 ($2.58^oS,\ 60.22^oW$) monthly occurrence of plasma blobs and plasma bubbles during low solar activity (LSA): (A) shows the occurrence pattern of the plasma blobs during low solar activity (LSA) with 29.31 hrs total hours of occurrence corresponding to 4.15% of total hours of OI 630.0 nm emission observation (705.57 hrs). (B) shows the occurrence pattern of plasma bubbles during low solar activity (LSA) with 112.08 hrs of occurrence corresponding to 15.89% of total hours of OI 630.00 nm emission observation (705.57 hrs).

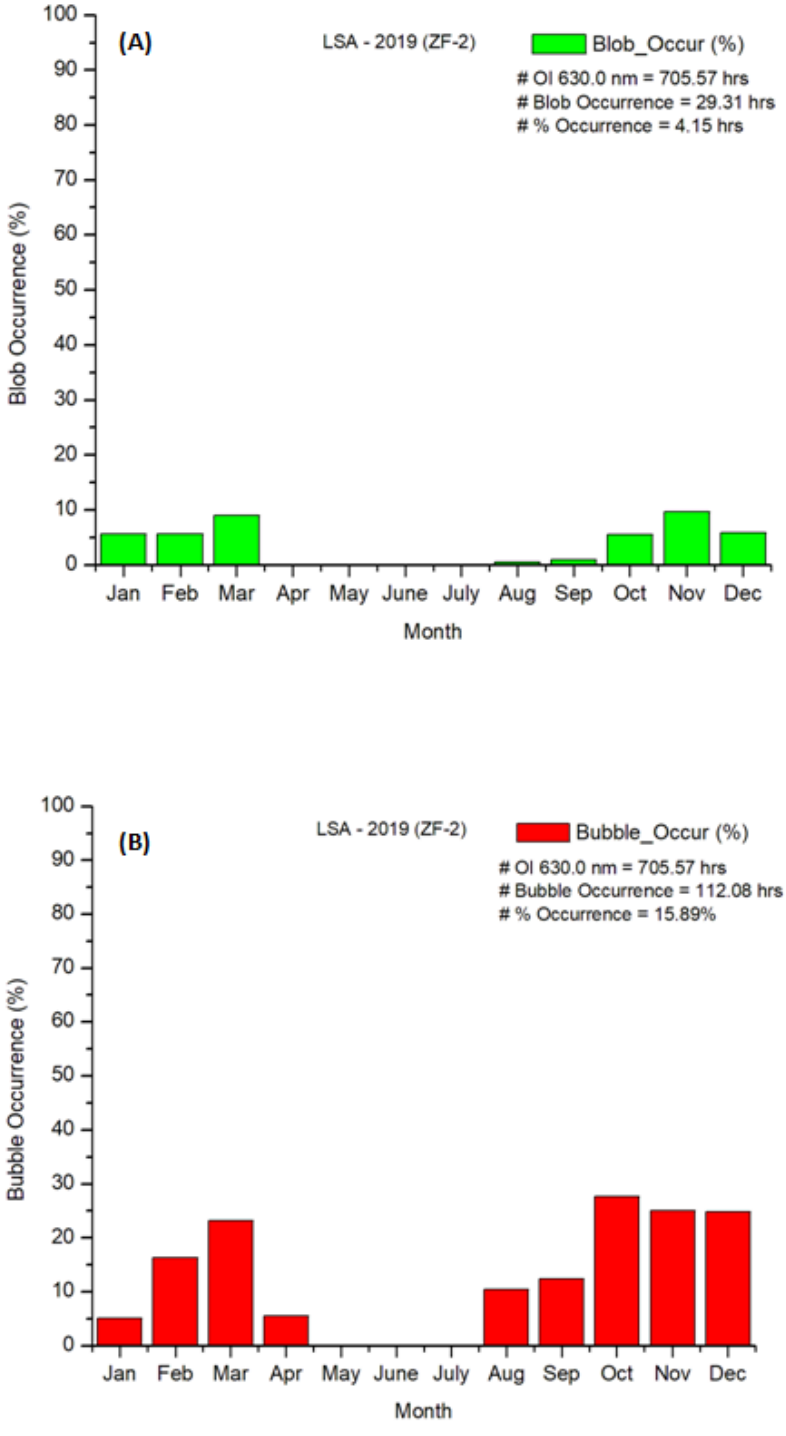

SOURCE: Author.

Figure 5.3 shows the comparison of the occurrence pattern of plasma blobs and plasma bubbles in low solar activity (LSA) at ZF-2. The two phenomena have three types of pattern. In the first pattern (January through April), both have their highest occurrence frequency in March. There was an occurrence of plasma bubbles without plasma blobs in April and this was due to geomagnetic storms. In the second pattern (May through July), the occurrence frequency of both plasma bubbles and plasma blobs is zero. Including August to the second pattern, we have the winter period of the southern hemisphere, and this implies that the occurrence frequency of plasma blobs during winter is approximately zero but that of plasma bubbles is relatively significant in August. In the third pattern (August through December), the rate of change of occurrence frequency of plasma bubbles is faster than that of plasma blobs, and in the first and third pattern plasma bubbles have the highest occurrence frequency. Plasma bubbles seasonal pattern observed in this work is in agreement with the seasonal pattern reported by Abdu et al. (1985) for range equatorial spread-F in the Brazilian sector and also Pimenta et al. (2001), Sahai et al. (1994), Sahai et al. (2000) reported similar seasonal pattern for plasma bubbles occurrence.

Figure 5.3 - The comparison of occurrence pattern of plasma blobs and plasma bubbles during low solar activity (LSA).

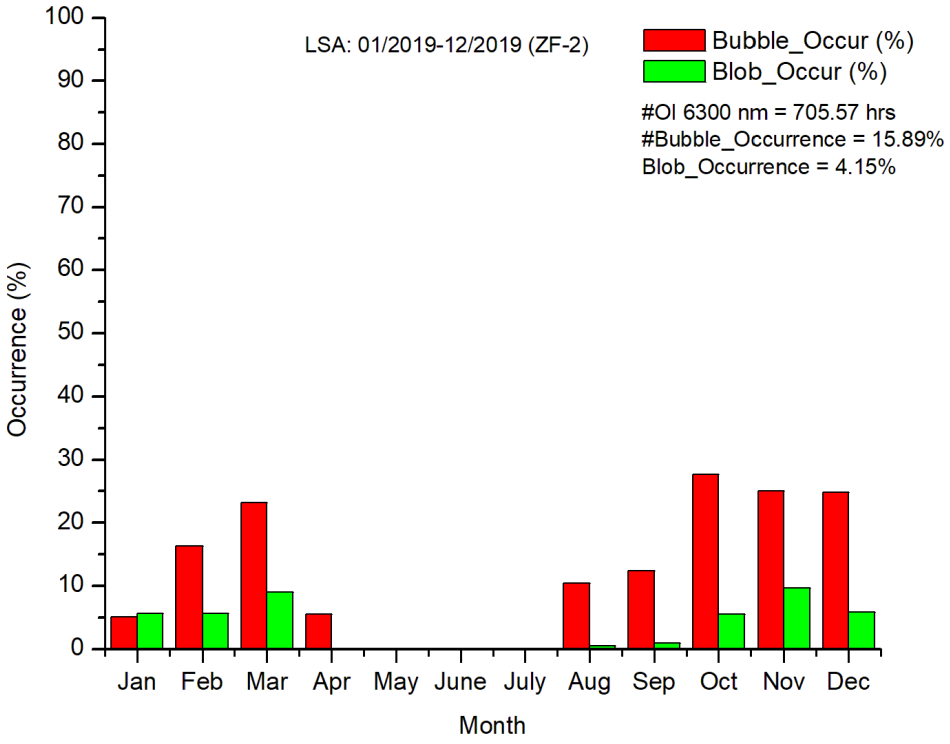

SOURCE: Author.

This is the first observation of plasma blobs occurrence characteristics over the Brazilian sector and as a result, there is no much work to cite for the comparison of occurrence pattern of plasma blobs in this work, unlike plasma bubbles. Meanwhile, observations have been reported that the occurrence of blobs has a complementary nature with that of the equatorial and low-latitude plasma depletions (bubbles) (PARK et al., 2003; WATANABE; OYA, 1986) and that there is some similarity in the seasonal-longitudinal distributions of blobs and bubbles (PARK et al., 2003; PARK et al., 2008). The mechanism leading to the formation of the blob has not been completely understood yet. In this work, during low solar activity (LSA), the occurrence pattern of plasma blobs has been found to be closely similar to that of plasma bubbles.

5.1.2 Plasma blobs in HSA

Figure 5.4(A) shows the monthly occurrence pattern of plasma blobs during high solar activity (HSA). Three patterns can be seen evidently in the figure: (1) January through April, (2) May through July, (3) August through December. In the first pattern, the occurrence frequency of plasma blobs exhibits a month-to-month variations and with the maximum in January. In the second pattern, no occurrence of plasma blobs was observed. In the third pattern, the occurrence frequency increases gradually from August through December with maximum in November and December. There appears to be a frequent occurrence of plasma blobs in the first three months of the year and the last three months of the year. Two main peaks can be seen in January and in November-December. In HSA, only one event of plasma blobs without plasma bubbles was observed and that was in late August 1999. There was a 500.16 hrs of total observation of OI 630.0 nm and 25.93 hrs of occurrence of plasma blobs; approximately 5%.

Figure 5.4(B) shows the occurrence pattern of plasma bubbles during HSA. Similarly, three patterns can be observed in the figure: (1) January through April, (2) May through August, (3) September through Decmeber. In the first pattern, the occurrence frequency of the plasma bubbles exhibits a month-to-month changes, and with the highest in March. In the second pattern, the occurrence of plasma bubbles is zero except in June which was a result of geomagnetic storm. Normally, the occurrence of plasma bubbles during winter of the southern hemisphere is approximately zero except there is a geomagnetic storm. In the third pattern, the occurrence frequency of the plasma bubbles starts in September and increases rapidly in October and later gradually decreases from October through December. Two main peaks are evident, and occur in March and October. Likewisely, there appears to be a frequent occurrence of plasma bubbles in the first three months and the last three months of the year. This result is in agreement with the occurrence characteristics reported by Sahai et al. (1994). Abdu et al. (2003) reported that the plasma bubble occurrence as well as the vertical rise velocity increase with the increase in solar flux; they attain larger values in summer months (centered around December) than in equinoctial months (March and September). There were four (4) events of plasma bubbles without plasma blobs during high solar activity (HSA). There was a 500.16 hrs of total observation of OI 630.0 nm and 98.79 hrs of occurrence of plasma bubbles; approximately 20%.

Figure 5.4 - The monthly occurrence of plasma blobs and plasma bubbles during high solar activity (HSA). (A) shows the plasma blobs occurrence pattern from July 1999 through June 2000. It has its highest in January 2000. (B) shows the plasma bubbles occurrence pattern in the same period and with its highest in both October and March.

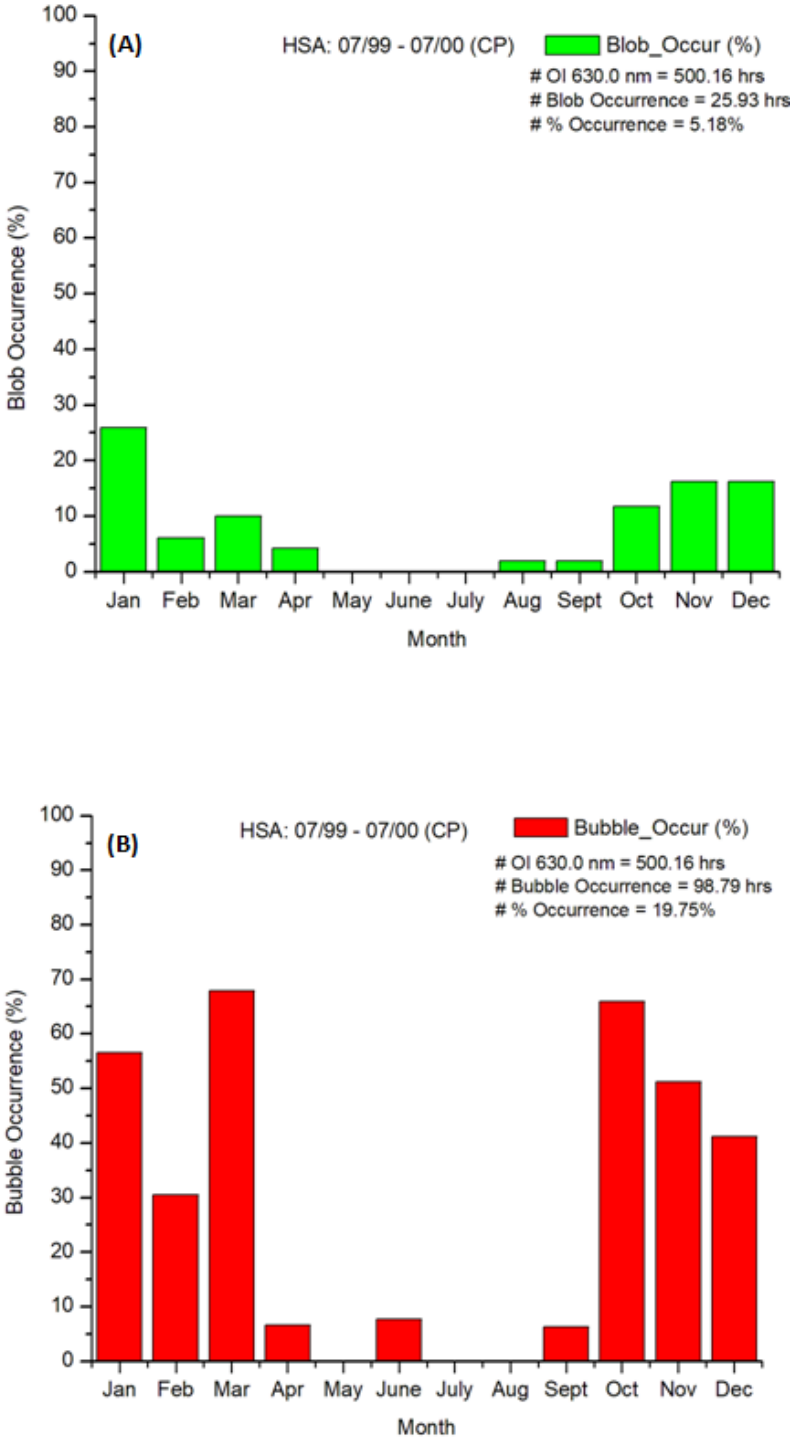

SOURCE: Author.

Figure 5.5 shows the comparison of the occurrence pattern of plasma blobs and plasma bubbles in high solar activity (LSA) at Cachoeira Paulista. First and foremost, plasma bubbles have higher occurrence frequency through out the whole year. Three patterns can also be observed: (1) January through April, (2) May through August, and (3) September through December. In the first pattern, both plasma bubbles and plasma blobs exhibit similar occurrence frequency and it changes from month-to-month. As one increases/decreases, the other also increases/decreases. In the second pattern, for May and July, the two phenomena were not observed, whereas, in June, plasma bubbles without plasma blobs were observed as a result of geomagnetic storm (Dst > -72.92, Sahai et al. (1998) have attributed this occurrence of plasma bubbles to the abrupt changes in the F-region vertical drifts in the equatorial region resulting from prompt penetration of high latitude electric fields generated during magnetic disturbances); in August, plasma blob was observed without plasma bubble. In the third pattern, occurrence of both plasma bubbles and plasma blobs are quite small in September. While the occurrence frequency of plasma bubbles increases in October, that of plasma blobs also increases. But as the occurrence frequency of plasma bubbles drops gradually through December, that of plasma blobs remains nearly constant.

Figure 5.5 - The compared monthly occurrence pattern of plasma blobs and plasma bubbles during high solar activity (HSA).

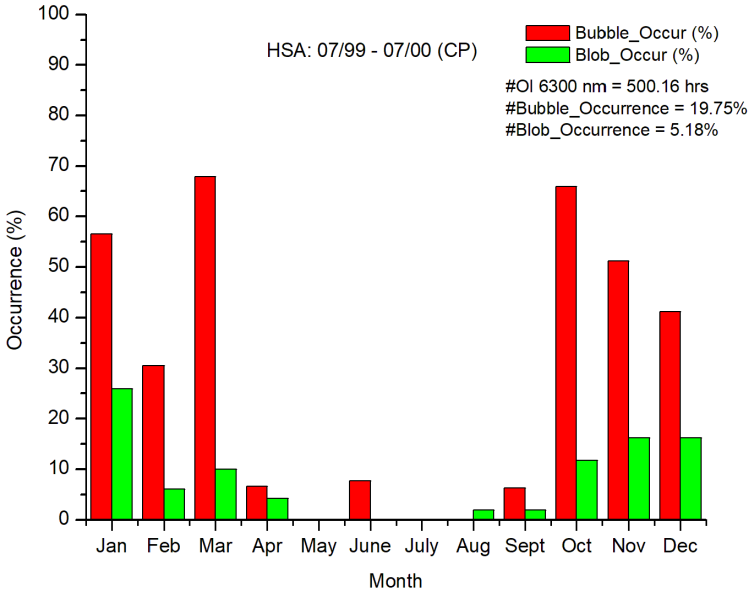

SOURCE: Author.

Figure 5.6 - (A) shows the OI 630.00 nm emission hours of observation for LSA and HSA. For the LSA, 705.57 hrs were the total hours of observation. For the HSA, 500.16 hrs were the total hours of observation. (B) shows the average daily solar flux during the LSA and HSA.

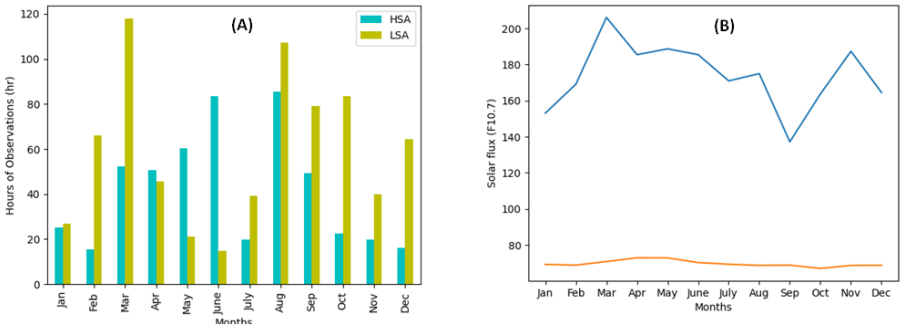

SOURCE: Author.

Figure 5.6(A) is the monthly hours of OI 630.0 nm emission observation for high solar activity (HSA) and low solar activity (LSA). During HSA, there was 500.16 hours of observation, and during LSA, there was 705.57 hours of observation. Besides, there were more observations of OI 630.0 nm during LSA than HSA. Figure 5.6(B) shows the daily average of solar flux during HSA and LSA. The LSA average solar flux has a quite steady pattern but reverse is the case for HSA.

In summary, Figure 5.7(A and B) shows the monthly variations of both plasma bubbles and plasma blobs as a function of solar cycle; high solar activity and low solar activity. In Figure 5.7(A), three patterns can be observed: (1) January through April, (2) May through August, and (3) September through December. In the first pattern, plasma bubbles occurrence frequency exhibits month-to-month changes during HSA, whereas during LSA, the occurrence frequency appears as a Gaussian function with little positive skewness and having its peak in March. Plasma bubble has it maximum occurrence frequency in March for both LSA and HSA. In the second pattern, plasma bubbles were observed in June during HSA but none in LSA, there were also events of plasma bubbles in August during LSA but none in HSA. In common, no events of plasma bubbles were observed in May and July during HSA and LSA. In the third pattern, the occurrence frequency increases rapidly from September to October for both HSA and LSA. The occurrence of plasma bubbles drops gradually from October through December for both HSA and LSA, with that of HSA more significant.

For plasma blobs Figure 5.7(B), apparently the occurrence frequency is lower than that of plasma bubbles. Similarly, three patterns can be observed: (1) January through April, (2) May through July, and (3) August through December. In the first pattern, the occurrence frequency is quite similar for both LSA and HSA with an occurrence of plasma blob in April of HSA but none in LSA. In the second pattern, no occurrence of plasma blob was observed. In the third pattern, the occurrence frequency is similar for both HSA and LSA as they both progressively increases from August through November. The occurrence of plasma blob drops in December of LSA while remains nearly uniform in HSA. In other words, in the third pattern, the pattern appears as a Log-Normal distribution for both HSA and LSA with negative skewness. It must be said that the plasma blobs event without plasma bubbles observed was not due to geomagnetic storms as the Dst $>$ -22.83 nT.

Figure 5.7 - The solar cycle occurrence pattern of plasma blobs and plasma bubbles. (C) shows the occurrence pattern of plasma bubbles during HSA and LSA and it has approximately occurrence time relative to the total time of OI 630.00 nm observation of 99 hrs (19.8%) and 112 hrs (15.9%) respectively. (D) shows the occurrence pattern of plasma blobs during HSA and LSA and it has approximately occurrence time relative to the total time of OI 630.00 nm observation of 26 hrs (5.2%) and 29 hrs (4%) respectively.

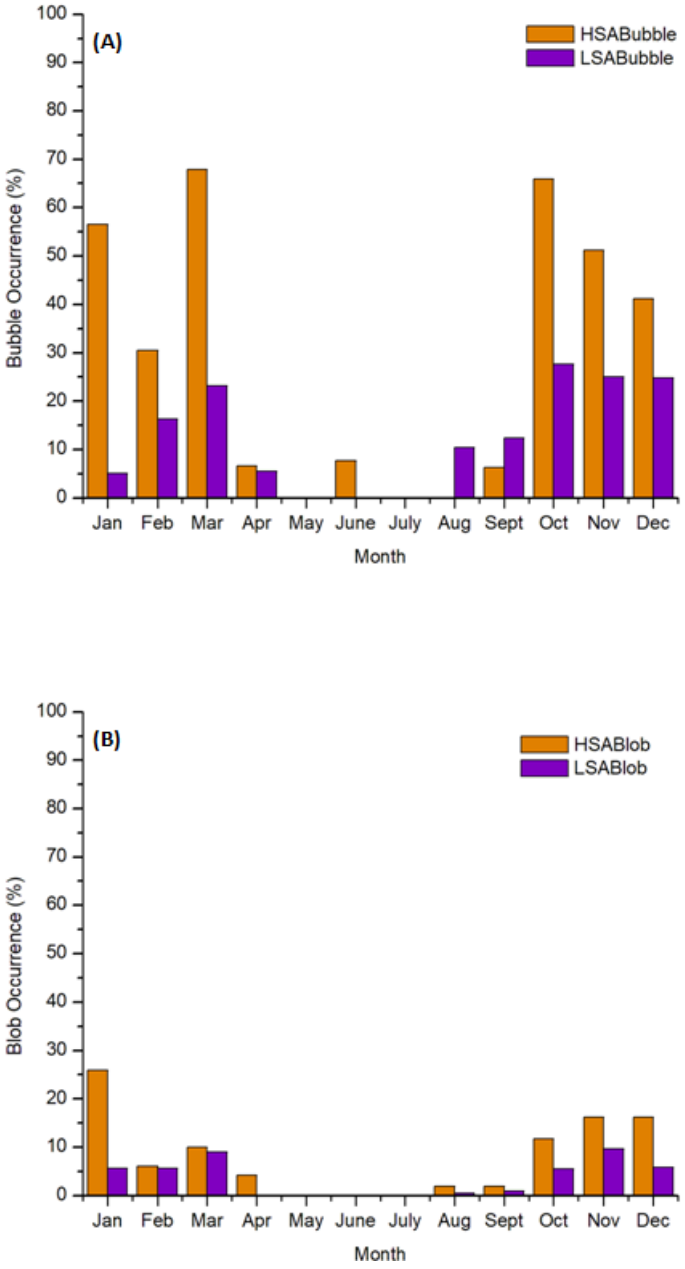

SOURCE: Author.

Figure 5.8 and Figure 5.9 show the total hours of the occurrence of plasma blobs and plasma bubbles during low solar activity and high solar activity. For both the plasma blob and plasma bubble their occurrence frequency peaks during the summer of LSA and HSA. The lowest occurrence frequency was recorded during winter for the blob and bubble. The total hours of the occurrence of plasma blobs during LSA is higher than during HSA (excluding the winter period) and this could be a result of the location of the all-sky imager which is an equatorial region (2.58^{o}S, 60.22^{o}W); a region associated with the frequent occurrence of plasma irregularities, or the larger data obtained from this location - ZF-2. The same trend is observed for the plasma bubbles (excluding the autumn period). From these figures, we can infer that the occurrence of bubbles and blobs are seasonal-dependent. The total occurrence frequency decreases from summer through the winter and later peaks up again in spring, which is the season preceding summer in the southern hemisphere. This is in agreement with Abdu et al. (2003) which reported that the rate of increase in bubble occurrence with increasing solar flux is higher during the November-December period (summer) than during the March-September equinox.

Figure 5.8 - The seasonal dependence of plasma blobs during low solar activity (LSA) and high solar activity (HSA).

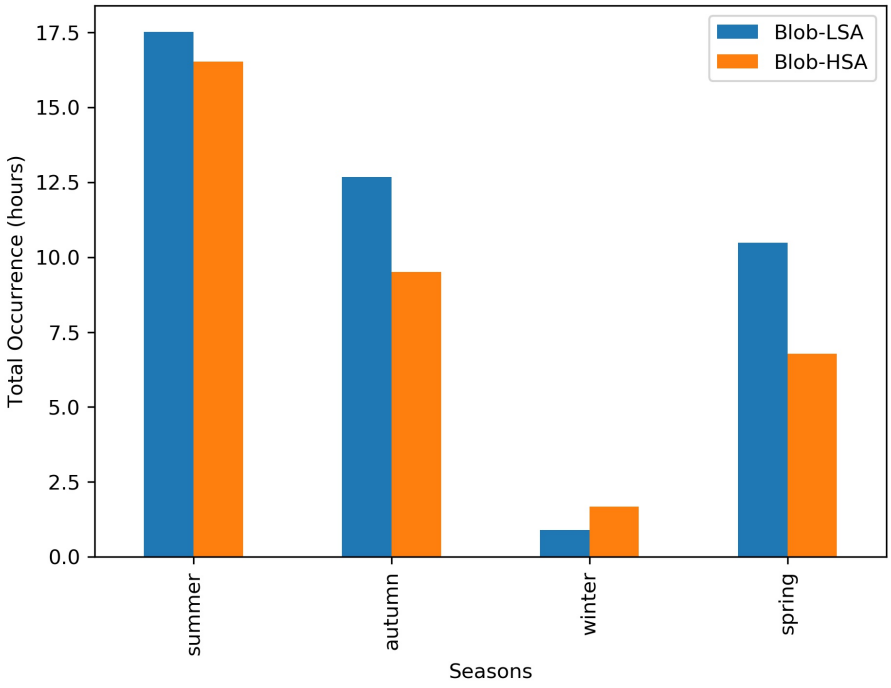

SOURCE: Author.

Figure 5.9 - The seasonal dependence of plasma bubbles during low solar activity (LSA) and high solar activity (HSA).

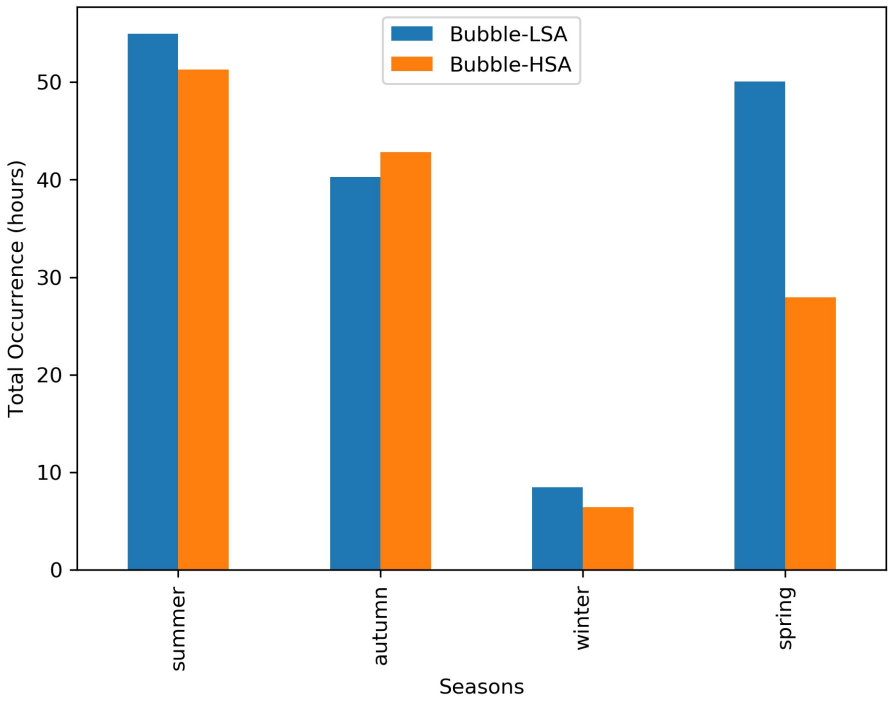

SOURCE: Author.

5.2 Nocturnal variations

5.2.1 Plasma blobs nocturnal variations

The nocturnal variations of plasma blobs in low solar activity (LSA) and high solar activity (HSA) have been studied based on the first time of appearance of blobs on the field of view of the all-sky imagers and their time of disappearance from the field of view of the imagers. The time of occurrence of each event was rounded up to the nearest hour. The occurrence frequency of both the appearance and disappearance with respect to local time is plotted. The nocturnal variations show different patterns between the years of low and high solar activities. During HSA, in Figure 5.10, the appearance occurrence frequency of plasma blobs increases rapidly at the post-sunset and decreases rapidly after (the peak) 22:00 LT. Whereas, during LSA, the appearance occurrence frequency increases gradually at the post-sunset and decreases gradually after (the peak) 23:00 LT. From the figure, it is obvious that the occurrence percentage of plasma blobs appearing on the field of view at

20:00 LT during HSA is higher than during LSA. This could be a result of an increase in ion production (O_2^+) during HSA because of the larger solar flux reaching the ionosphere during the day. There is 0% occurrence frequency at 18:00 and 19:00 LT. During sunset 18/19 hr at the equator and low-latitude region, airglow emission is very low because the plasma is very high. Thus, irregularities are not visible in OI 630.0 nm airglow emission. But at post-sunset, altitude of F-region decreases due to the reversal (downward) of vertical drift thereby resulting into bright airglow which enables us to observe the irregularities. Therefore, if plasma blobs can be seen on the field of view at around 20:00 LT, then, we can infer that plasma blobs are formed just after the sunset together with the plasma bubbles. The occurrence percentage of plasma blobs appearing at exact midnight and post-midnight is very low. Thus, from the physical observations, there is a high tendency of plasma blobs getting fully developed during pre-midnight.

Figure 5.10 - The nocturnal variations of plasma blobs based on the occurrence frequency of their time of appearance on the field of view of the images during HSA and LSA.

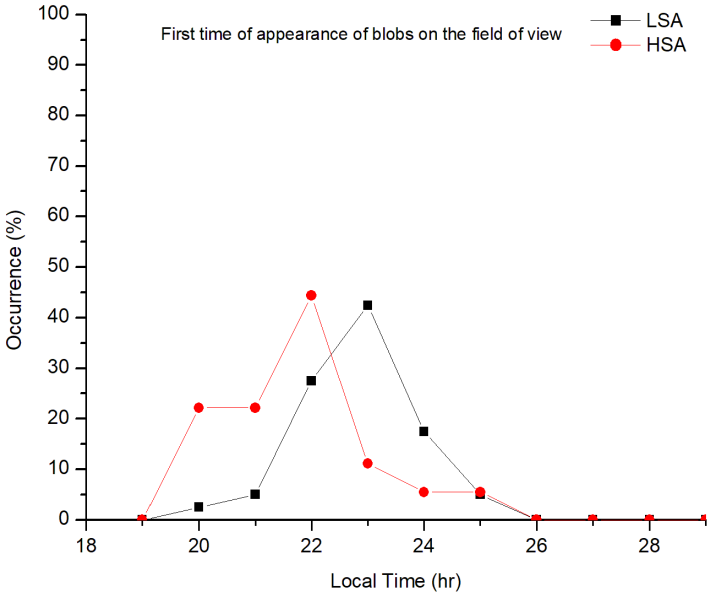

SOURCE: Author.

For the disappearance of plasma blobs in Figure 5.11, during HSA, occurrence per-

centage increases gradually and decreases gradually after (the peak) 23:00 LT. This is approximately one hour after its appearance. Whereas, during LSA, it increases slightly and maintains a flat at about 21:00 through 23:00 LT which later rapidly increases with its peak at 24:00 LT, then gradually decreases. This is also approximately one hour after its appearance. In addition, the occurrence frequency of plasma blobs vanishing from the field of view of all-sky imagers during post-sunset and pre-midnight is higher during HSA than LSA, but reverse is the case at the post-midnight. The average visibility time of plasma blobs on the field of view of the imagers during HSA and LSA was 1.08 hr and 0.57 hr respectively. Whereas, the average visibility time of plasma bubbles on the field of view of the imagers during HSA and LSA, was 4.01 hr and 2.19 hr respectively. Hence, plasma blobs have a shorter visibility time than plasma bubbles and most of the plasma blobs disappeared from the field of view at about pre-midnight hours and just after the midnight hour for HSA and LSA, respectively.

Figure 5.11 - The nocturnal variations of plasma blobs based on the occurrence frequency of their time of disappearance from the field of view of the images during HSA and LSA. The '2' added to the LSA and HSA were just used to differentiate the columns of the data during analysis.

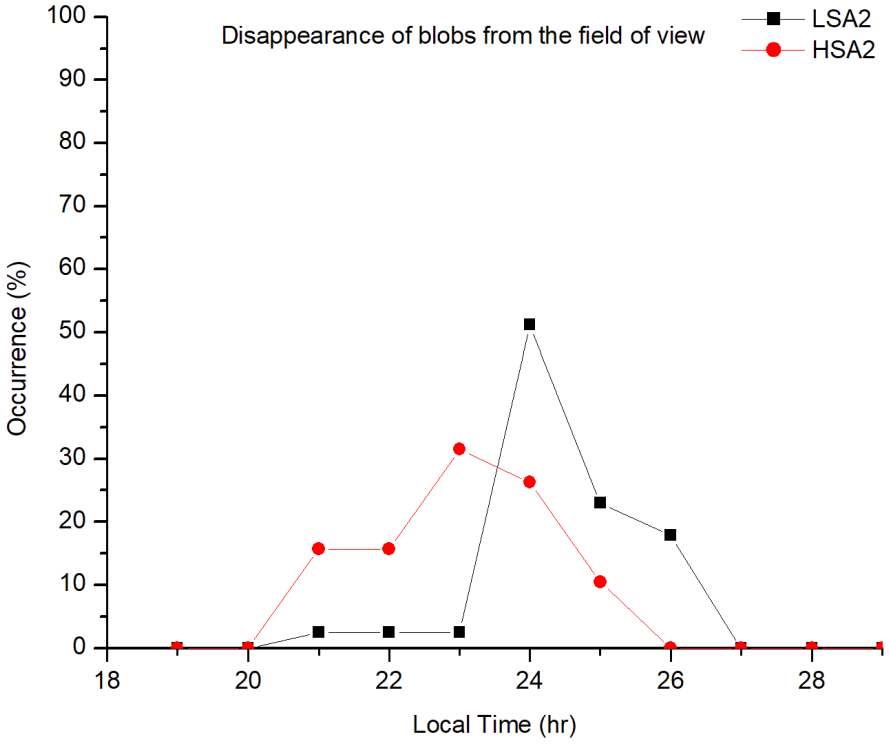

SOURCE: Author.

5.2.2 Plasma bubbles nocturnal variations

Figure 5.12 - The nocturnal variations of plasma bubbles based on the occurrence frequency of their time of appearance on the field of view of the images during HSA and LSA.

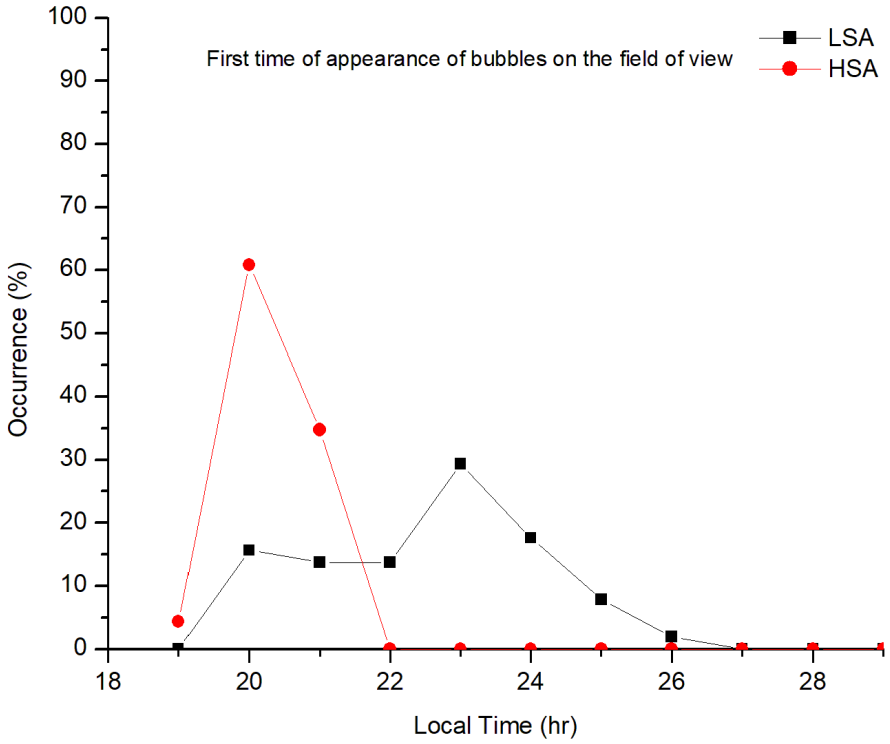

SOURCE: Author.

The nocturnal variations of plasma bubbles have been studied based on the first time of appearance on the field of view and the time they disappear (or vanish) from the field of view in OI 630.0 nm emission. In this work, each time of plasma bubbles' appearance and disappearance were rounded up to the nearest hour, and their occurrence percentage was calculated to produce the results shown in Figure 5.12 and Figure 5.13. In Figure 5.12, during LSA, the nocturnal variation of plasma bubbles based on their first time of appearance increases gradually at post-sunset (20:00 LT); slightly decreases through 22:00 LT, and later increases reaching its peak at 23:00 LT, then decreases gradually at post-midnight. Thus, appearance of plasma bubbles has two peaks; post-sunset and pre-midnight. Whereas during HSA, the nocturnal

variation of plasma bubbles appears earlier at post-sunset (19:00 LT) than during LSA (20:00 LT). It increases rapidly reaching its peak at around 20:00 LT and then decreases rapidly. We can infer from this result that (1) there is higher tendency of development of multiple plasma bubbles (MPBs) during LSA than HSA, (2) development of plasma bubbles are restrained to the post-sunset hours during HSA. This result is in agreement with the nocturnal variations of plasma bubbles reported by Sahai et al. (2000), Pimenta et al. (2001) where they both reported the plasma bubbles reaching their maximum occurrence frequency in earlier time during HSA than LSA. The earlier appearance of plasma bubbles during HSA could be attributed to the stronger F-region vertical plasma drift during high solar activity (HSA) as reported by Batista et al. (1996). Oya et al. (1986) carried out occurrence probability of plasma bubble and they reported the major peak at 22 LT and the sub-peak at 20 LT. They associated these peaks with the occurrence of multiple plasma bubbles (MPBs) as observed by the Hinotori satellite.

Figure 5.13 - The nocturnal variations of plasma bubbles based on the occurrence frequency of their time of disappearance from the field of view of the images during HSA and LSA.

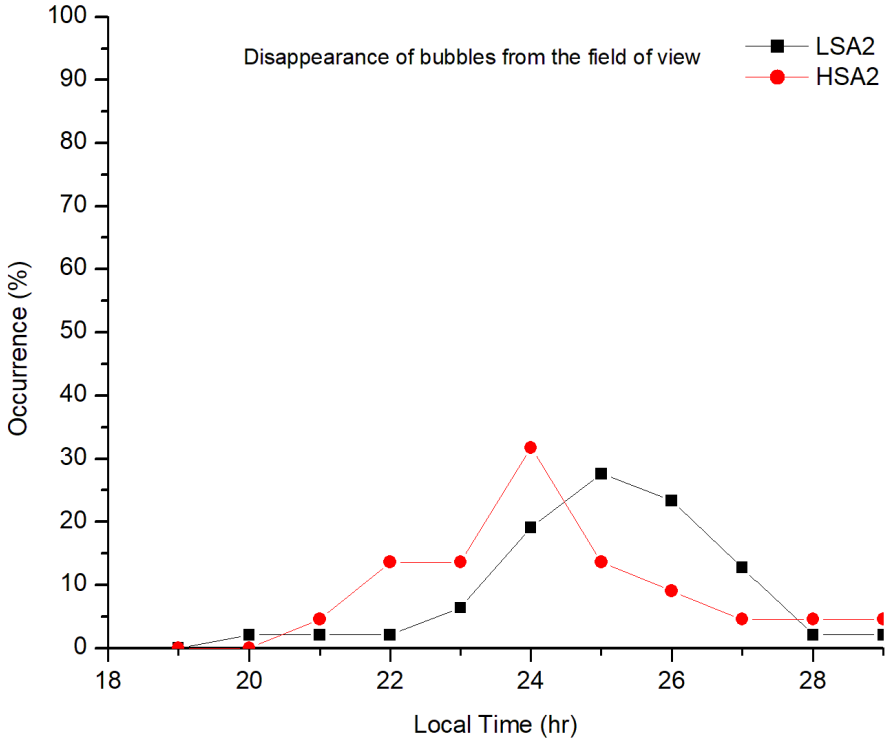

SOURCE: Author.

Figure 5.13 shows the time of disappearance of plasma bubbles from the field of view for both LSA and HSA. During LSA, the plasma bubbles disappearance pattern increases gradually with a flat in 20:00 through 22:00 LT, reaches the peak at 25:00 LT, and then decreases gradually. The vanishing occurrence of plasma bubbles at post-sunset through pre-midnight hours is really small but substantially significant at post-midnight hours. Thus, plasma bubbles, during LSA, disappear (or vanishes) from the field of view mostly at post-midnight hours. Whereas, during HSA, the plasma bubbles disappearance pattern increases gradually (of course higher than LSA), reaches its peak at 24:00 LT, and then decreases gradually with a flat at 27:00 LT through 29:00 LT. Thus, plasma bubbles that developed at post-sunset hours, during HSA, disappear from the field of view mostly at about midnight hours (considering their visibility time duration). Sinha et al. (2001), using an all-

sky optical system, estimated that plasma depletion takes typically, about 2 h 40 min to come to a fully developed stage. The disappearance of plasma bubbles at the later time supports the existence of MPBs (Multiple Plasma Bubbles) as reported by Oya et al. (1986).

5.3 Plasma blobs features

5.3.1 Physical dynamics

Figure 5.16 shows a sequence of OI 630.0 nm all-sky unwarped images obtained from 23:03:28 to 00:11:07 LT at ZF-2, showing plasma bubbles and the associated plasma blobs. In this image sequence, 2 blobs can be clearly seen with the density depletion bands at the middle and drifting towards the North-East of the view. On this day, plasma blobs appeared on the view firstly and thereafter, the depletion bands. It was observed that as the plasma blob drifts, its brightness and scale sizes increase simultaneously at the initial stage. Then, after passing through the zenith of ZF-2, the plasma depletion tends to have been shrinking the blob resulting in the gradual decrease of its sizes but brightness relatively remains constant as it vanishes. In some other occasions, the formation of the blob was observed as though there were two opposite forces acting (Figure 5.14), and where they met was where the 'bright regions' occur i.e an accumulated region of plasma for a specific short period of time and vanishes thereafter. Some of the plasma blobs were observed to be formed very close to the northern edge of the view (equator) then drifted from west to East while still at the northern edge of the field of view.

Figure 5.14 - Formation of blobs by the action of two opposite forces. Wind towards NW acting against the $\boldsymbol{E}\times\boldsymbol{B}$ drift.

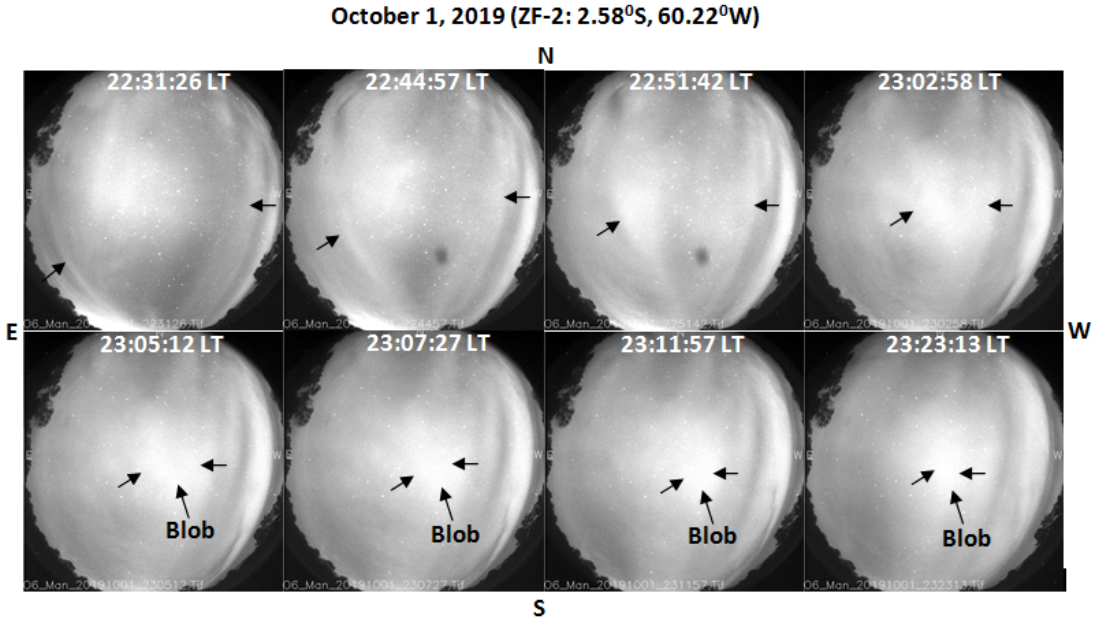

SOURCE: Author.

On the other hand, at Cachoeira Paulista, Figure 5.1, plasma bubbles appeared on the field of view firstly then followed by plasma blobs. But in this case, plasma blobs outlived the plasma bubbles. Plasma blob being trapped between plasma bubbles drifts from the west towards northeast tilting westward as it drifts. The westward tilting of the plasma blob here seems to have been a result of high magnetic declination at the location of the all-sky imager. However, Park et al. (2015) and Park et al. (2010), observed a westward tilt of plasma blobs and they suggested that blobs are contained within tilted shells of geomagnetic flux tubes, which are similar to the shell structure of equatorial plasma bubbles. Le et al. (2003) suggested that during the upward motion of the plasma bubble, the field-aligned plasma pressure gradient at the poleward edges of the depletions produces an equatorward force that drives the plasma particles towards the equator. Therefore, the density depletions cannot extend to higher latitudes and remain limited to the region of the anomaly crests. The polarization electric field that is generated within the bubble can be mapped along the magnetic field lines to higher latitudes, beyond the limited density depletion structure. In this way, the polarization electric field within the flux tube

moves the high-density plasma, near the anomaly crests, upward, so that density increments occur just above the flux tube. Ossakow et al. (1979) reported that the growth of the collisional Rayleigh-Taylor instability exhibited plasma density depletions moving upward, as well as plasma density enhancement regions in the F-region bottomside. Their calculations of the electric potential distribution indicate that the upper part of the bubble is acted on by an induced eastward electric field, causing the bubble to rise with a velocity $(-c/B)\nabla\phi \times \overrightarrow{z}$, where c is the speed of light, ϕ is the induced or polarization electric field, and B is the ambient geomagnetic field in the z-direction. However, the lower portion of the bubble (F-region bottomside) is acted on by an induced westward electric field, causing the localized plasma density enhancements to move downward along with the lower altitude depletions. Thus, they reported that isolated depletions and enhancements should move up and down, respectively, at the equator. However, this concept is altered when depletions are surrounded by enhancements or vice versa (OSSAKOW et al., 1979). Notice that in this research, both during LSA and HSA, none of the plasma blobs had been observed to be formed at the southern edge of the view and none extends towards the southern edge of the field of view. We don't have clear explanation for this observation and why plasma blobs do not extend upto the southern edge of the field of view. Whereas, plasma bubbles do.

Finally, we have observed, physically, a strong dependence of the formation of plasma blobs on the magnitude of plasma bubbles development. The intensity of the plasma blob's brightness has been observed to be proportional to the extent to which plasma bubbles have developed. For instance, the plasma bubbles without plasma blobs events observed, Figure 5.15, contained plasma bubbles residing and drifting at the northern edge of the view i.e. the black structure not fully covering the N-S of the view (unlike Figure 5.21). Or the black structure being relatively fainty. In these two cases, plasma bubbles weren't intense as can be seeing on the all-sky imager. Also, fully developed plasma blobs have been observed besides fully developed plasma bubbles, see Figure 4.4(A). Thus, the formation and dynamics of plasma blobs appear to be closely related to the activity of the induced polarized electric field inside the plasma depletions originated at the bottomside of the F-region, and the restorative forces such as the gravitational force and pressure gradient. Krall et al. (2010) reported circumstances in which the density on or above the ESF crests leads to a plasma blob. In one case, slowly growing ESF produces upward $\boldsymbol{E} \times \boldsymbol{B}$ drifts that move density upward faster than gravity moves it downward, with the result that densities on ESF crest field lines, at or above the density crests, have densities that are enhanced relative that of the background ionosphere. The second circumstance

in which an ESF density crest becomes a density enhancement occurs in the presence of mild meridional wind. Hence, extensive study of the onset development of bubbles and their interaction with the plasma may provide a clearer mechanism responsible for the formation of blobs associated with bubbles.

Figure 5.15 - The plasma bubble without blob event on June 26, 2000 at 22:21:25 LT in the field of view of the imager deployed at Cachoeira Paulista.

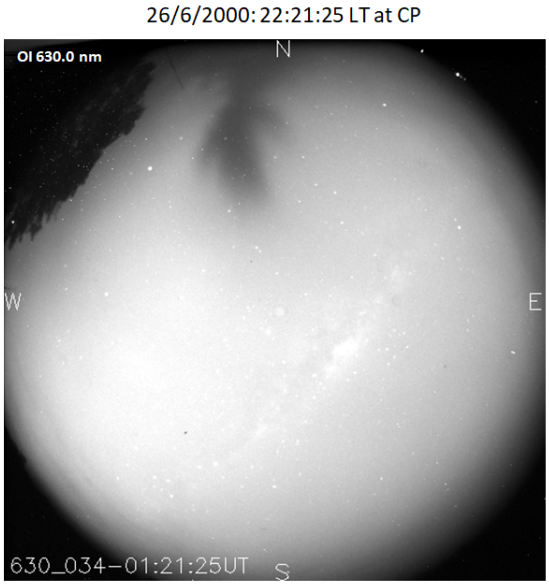

SOURCE: Author.

5.3.2 Statistical results

Consider Table 5.2, the average visibility time of plasma blobs in hours, during HSA and LSA, were 1.08 hr (64.8 mins) and 0.57 hr (34.2 mins), respectively. But due to the presence of outliers in the data i.e. data far different from the majority, the median hours are quite different and seem to be more reliable and they are 0.83 hr and 0.38 hr for HSA and LSA respectively. This implies that plasma blobs have a longer visibility time during HSA than LSA. Recall that plasma blobs are being associated with the ionization enhancement in the bottomside of the F-region in the ionosphere (PIMENTA et al., 2004) and greater solar flux reaching the ionosphere during HSA increases the chance of this enhancement, thereby, perhaps, sustaining the occurrence of plasma blobs longer during HSA than LSA. Pimenta et al. (2004), reported at least 20 minutes visibility time for plasma blobs. Hence, this work is in

Table 5.2 - Plasma blobs statistical results based on the hours of occurrence during high (HSA) and low (LSA) activities.

	High Solar Activity (HSA)	Low Solar Activity (LSA)
Average hours	1.08 ($\approx$ 65 *mins*)	0.57 ($\approx$ 34 *mins*)
Median hours	0.83 ($\approx$ 50 *mins*)	0.38 ($\approx$ 23 *mins*)
Standard Deviation	1.04	0.68
Average Modal hours	0.80	0
Pearson Correlation	+0.738	+0.870
Outliers	4.76	3.12
Maximum	4.76	3.12
Minimum	0	0

SOURCE: Author.

agreement with the earlier work observations. Also, the Pearson correlation between plasma bubbles and plasma blobs' monthly hours of occurrence, during HSA and LSA, was different. The correlation during HSA was lower (+0.738) than during LSA (+0.870). This implies that they are more likely to be linearly related during LSA than HSA. It must be said that the Pearson Correlation coefficient was lower when carried out on the individual events rather than monthly. It was positive and strong (+0.602) for LSA but positive and weak (+0.217) for HSA.

5.3.3 Plasma blobs zonal drift

To obtain an estimate of zonal drift velocities from the imaging data: firstly, the images are linearized, and we scan the optical images from west to east to obtain a cross-section of the brightness patterns for each plasma blobs. Then, these cross-sectional scans are subjected to a correlation analysis leading to the best fit spatial shifts required to match the time between images. A succession of such space and time shifts leads to a zonal velocity versus local time relation for the blobs and bubbles. In this work, only the zonal drift velocities of plasma blobs are considered.

In this work, Table 5.3, four (4) events of plasma blobs, each from different months for both LSA and HSA were used to estimate the mean zonal drift velocity of plasma blobs and their E-W and N-S spatial extensions. The mean eastward speed of the plasma blobs in LSA and HSA was, approximately, 67 ± 27 m/s and 61 ± 21 m/s, respectively. Furthermore, blobs displayed, typically, east-west and north-

Table 5.3 - Plasma blobs motional characteristics during high (HSA) and low (LSA) activities.

	HSA	LSA
Events	4	4
Months	Jan, Mar, Oct and Dec	Jan, Mar, Oct and Dec
Average Drift Vel.	61 $\pm 21 m/s$	67 $\pm 27 m/s$
E-W extension	54-83 km	41-81 km
N-S extension	87-129 km	110-230 km

SOURCE: Author.

south extensions of 41-81 km and of 110-230 km, respectively, during LSA. But during HSA, plasma blobs displayed east-west and north-south extensions of 54-83 km and 87-129 km. Tardelli-Coelho et al. (2017), in their work, estimated the mean zonal drift velocity of blobs to be 61 ± 6 m/s and its east-west and north-south extensions to be 263 km and 591 km over a low latitude station São José dos Campos (SJC) ($23.21^oS,\ 45.86^oW$; *dip latitude* 18.3^oS) in the Brazilian sector. Pimenta et al. (2007), during a major geomagnetic disturbance at Cachoeira Paulista ($22.7^oS,\ 45.0^oW$), Brazil, estimated the mean westward speeds of the plasma blobs to be 30 m/s and its east-west and north-south extensions to be 110-160 km and 200-450 km, respectively.

Figure 5.16 - The sequence of OI 630.0 nm all-sky images obtained from 23:03:28 to 00:11:07 LT, on the night of March 1, 2019, showing airglow depletion bands and blobs during the midnight. Unwarped images which correspond to a mapped area of the processed image $1024 \times 1024 km^2$ in the OI 630.0 nm airglow layer, assuming an emission altitude around 275 km. The dark region in the upper right and lower-left corner is due to trees in the view image.

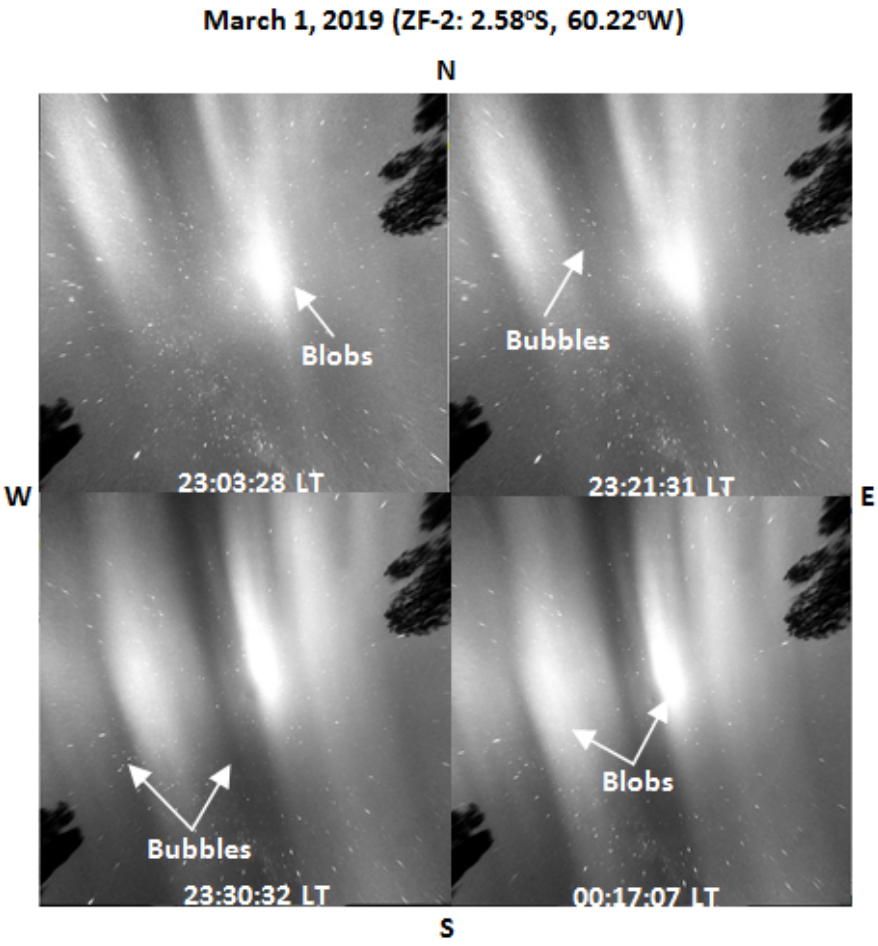

SOURCE: Author.

5.3.4 Plasma blobs merging

Figure 5.17 - Sequential all-sky images of plasma blobs merging on October 25-26, 2019. The images show two bright regions merging as they drift towards the east of the field of view. B represents blob.

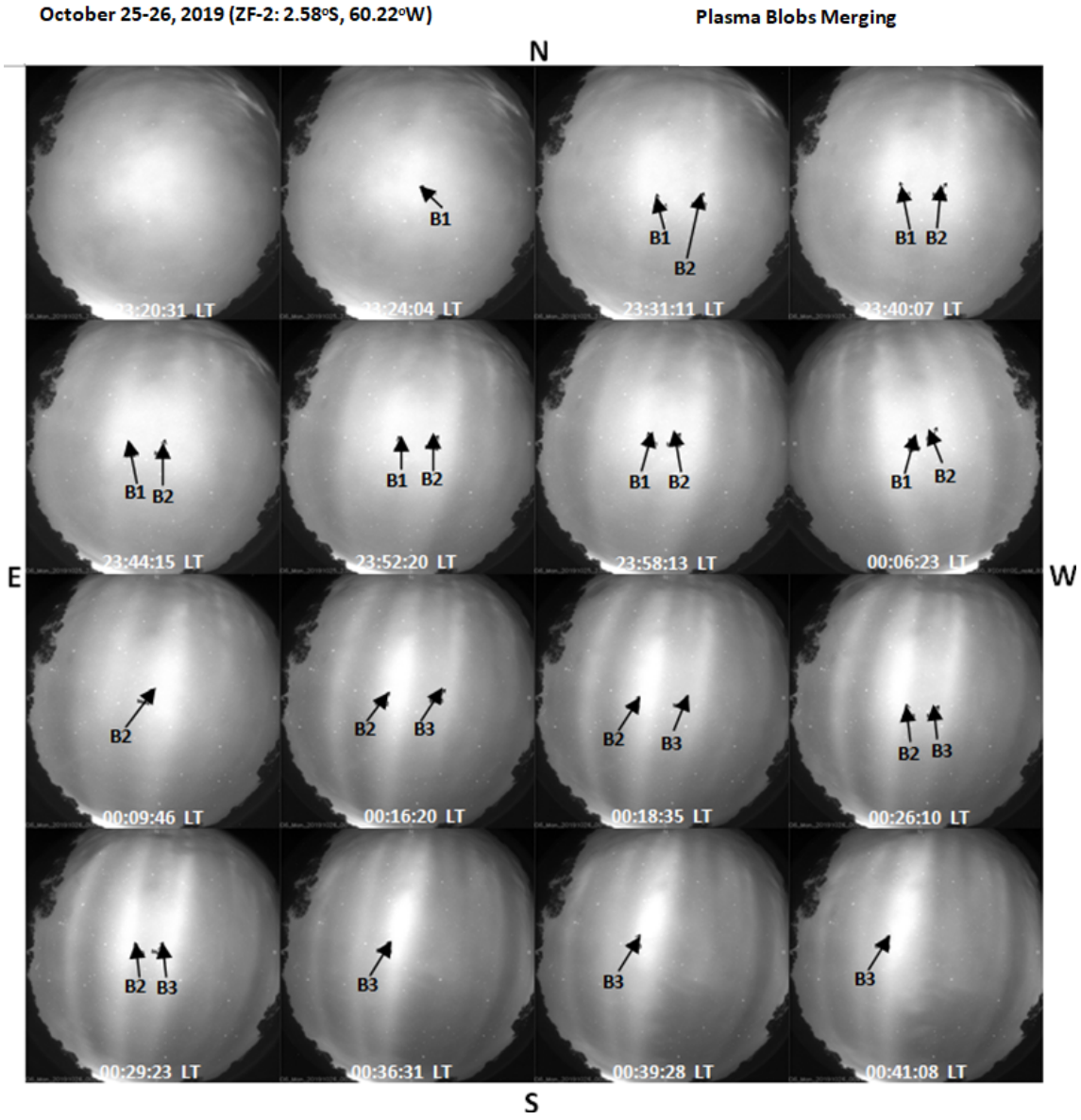

SOURCE: Author.

Figure 5.17, on October 25-26, 2019, for the first time, plasma blobs were observed to be merging together as they drift towards the east. At the initial, at 23:24:04 LT only

one blob (B1) was appearing and later another one appeared (B2) at 23:31:11 LT. Both blobs were drifting separately and moving closer to each other. At 00:09:46 LT, B1 and B2 merged together and the initial two structures became one and drift eastward. Later, another blob, B3, appeared and drifts eastward towards blob, B2. The two blobs drift separately for a while before merging together at 00:36:31 LT. Eventually, no other blobs showed up after the B2 and B3 merging, therefore, B3 drifts eastward alone. Notice that before they merged the space between them became indistinct (see 00:06:23 LT and 00:29:23 LT). More or less like plasma attracting one another. Using the linearization technique as described in chapter 3, we studied the temporal-spatial extension of blobs during the merging process and we found out that, for instance, from 00:09:46 LT through 00:41:08 LT in Figure 5.18, B2 E-W extension decreases (97 km, 91 km, 78 km, 65 km, 64 km) as it drifts before finally merged with B3. In contrast, the B3 E-W extension increases (44 km, 47 km, 49 km, 52 km, 84 km, 84 km, 81 km) as it drifts before merging with B2 but decreases after merging. B2 loses its E-W extension rapidly with an average scale length of about 8 km but B3 before merging gains E-W extension gradually with an average scale length of about 3 km. After the merging process successfully, the B3 E-W extension increased by almost twice of its onset E-W extension; confirming the addition of another blob. Plasma blobs are field-aligned structures and they possess 2D FAC (field aligned current) sheet structures at the walls Park et al. (2010). So we propose that a big plasma blob along the magnetic field lines would merge with another succeeding smaller blob when its scale size (E-W extension) is above a certain threshold, and the decrease in zonal neutral wind velocity with time and gravity could be responsible for this process. The study of the behavior of geomagnetic field lines topology, the strength of the zonal neutral wind, and gravity during this occurrence could reveal a more accurate mechanism responsible for plasma blobs merging. This feature of plasma blobs is planned to be examined properly in future works to detect the threshold scale size of blobs liable for merging. However, Park et al. (2010) reported low-latitude plasma blobs (at 00:00 LT similar to the merging time in this work - 00:09 LT) in which perpendicular magnetic deflections were linearly polarized (tilted toward the west from the magnetic meridian). This kind of behaviour of magnetic field lines can cause merging. Gurav et al. (2019) reported plasma bubbles merging at around the pre-midnight period and concluded that plasma bubbles merging occurred due to the tilt changes as well as the non-linear evolution at the top portions of EPBs. Hence, plasma blobs merging appears to be the principle behind a fully developed plasma blob observed in this work.

Figure 5.18 - The figure shows the east-west scale-size of the blobs during the merging process on October 25-26, 2019 at ZF-2 in Amazona region. B2 and B3 (B denotes Blob) were studied to observe their E-W extension during the merging process.

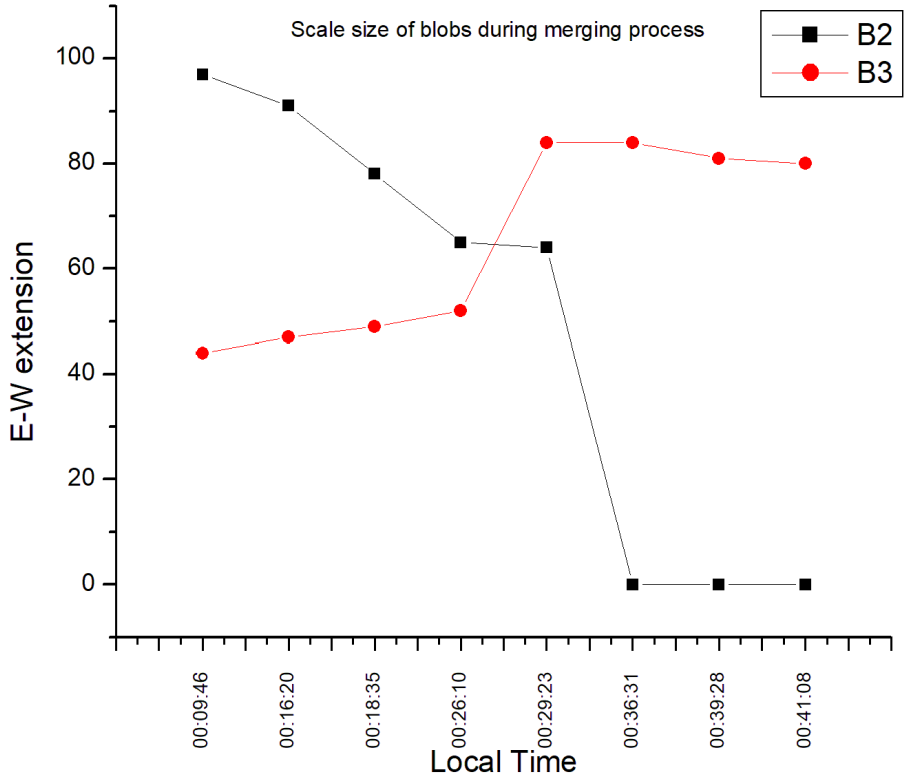

SOURCE: Author.

5.3.5 Plasma blobs detachment

Figure 5.19 - Sequential all-sky images of plasma blobs detachment on March 1-2, 2019 at ZF-2 (2.58^{o}S, 60.22^{o}W). The detachment of a plasma blob from another has been associated with a developing plasma bubble.

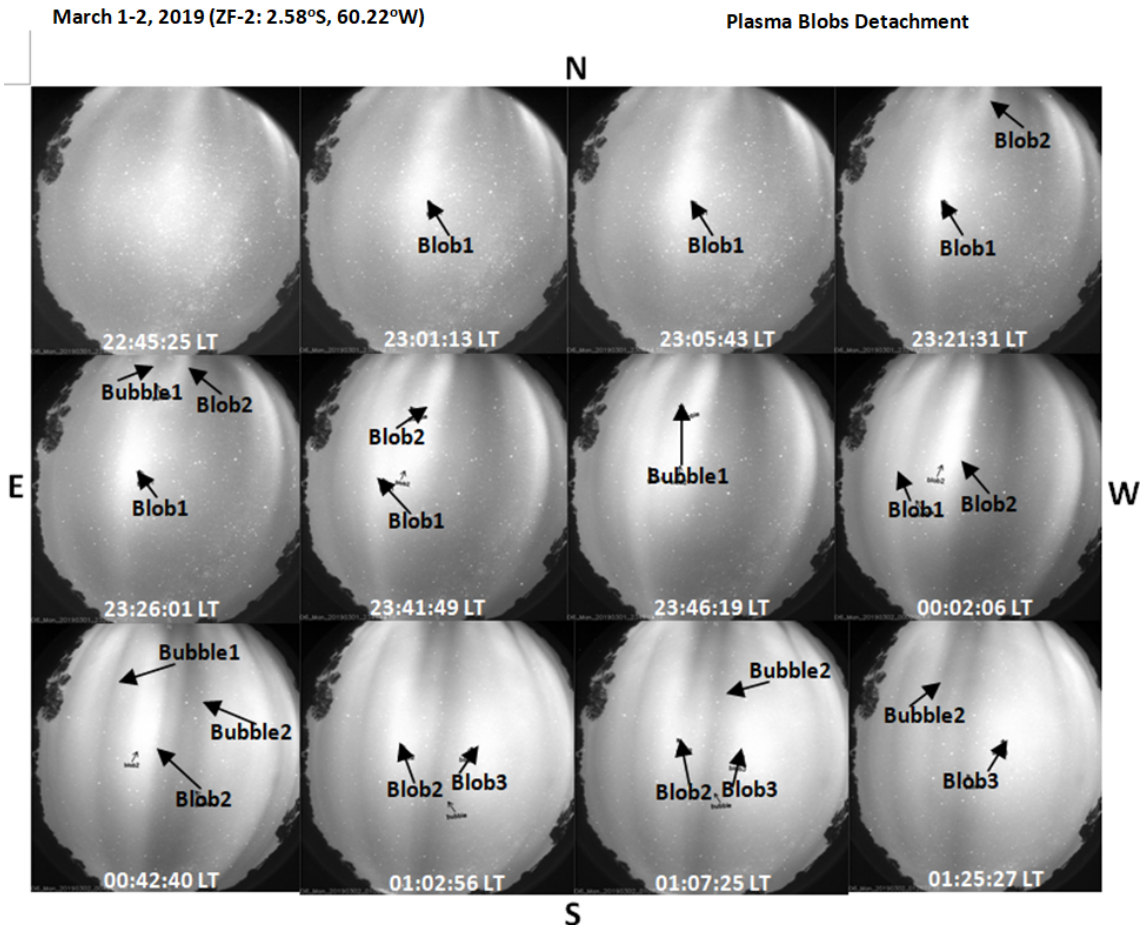

SOURCE: Author.

Figure 5.19, on March 1-2, 2019 at ZF-2 (2.58^{o}S, 60.22^{o}W) at around midnight plasma blobs, for the first time, were observed to be detaching into two pieces of blobs by the development of midnight equatorial plasma bubbles. At 23:01:13 LT plasma blob almost at the zenith of the all-sky imager was drifting alone eastward at the initial. The blob has its origin at the north of the view and extends to the middle of the image. As the blob (Blob1) drifts eastward for a while, there appeared another blob (Blob2), detaching from the north of the view. Simultaneously with the

appearance of Blob2 was a small plasma bubble (Bubble1) also developing at the north of the view. As the 'Blob1' drifts closer to the East of the view, its East-West extension increases, and this could be linked to the growing plasma bubble (Bubble1) which appears to have been dividing the 'Blob1' into two parts (see 23:46:19 LT of the image). Eventually, after a while, the bubble (Bubble1) successfully divided the blob (Blob1) into two parts; Blob1 and Blob2. At this time the bubble (Bubble1) has already extended to about 2/3 of N-S of the field of view (see 00:02:05 LT of the image) and the two blobs (Blob1 and Blob2) can be seen separately with 'Blob1' fading away. Furthermore, at 00:42:40 LT, after about 40 minutes that 'Blob1' divided into two, 'Blob1' was no longer appearing on the field of view but only the 'Blob2' staying right beside a fully developed plasma bubble (Bubble2). And notice that as at the time 'Blob1' was no longer visible, the initial plasma bubble, 'Bubble1', was already covering the full N-S of the view. Then, as the fully developed plasma bubble, 'Bubble2', drifts eastward towards the 'Blob2', the intensity of its blackness decreases, the 'Blob2' intensity decreases, and another fainter blob, 'Blob3', appears at the opposite side of 'Bubble2' (see 01:07:25 LT of the image). Thus, 'Bubble2' divides 'Blob2'. After a while, 'Blob2' was no longer appearing on the field of view, 'Bubble2' had lost almost half of its intensity, and 'Blob3' was already formed. In summary, we have observed the detachment of plasma blobs as a consequence of (1) the substantial scale size of the blob, (2) the development of post-midnight EPBs, and (3) the greater drift velocity of the bubble than the blob.

Figure 5.20 - The sequential unwarped all-sky images of plasma blobs detachment on March 1-2, 2019 at ZF-2 (2.58^{o}S, 60.22^{o}W). The figure shows a dark structure bubble - developing at the northern edge of the view, splitting the white structure blob. The black structures at the top right and bottom left is the image of trees at the location of the imager.

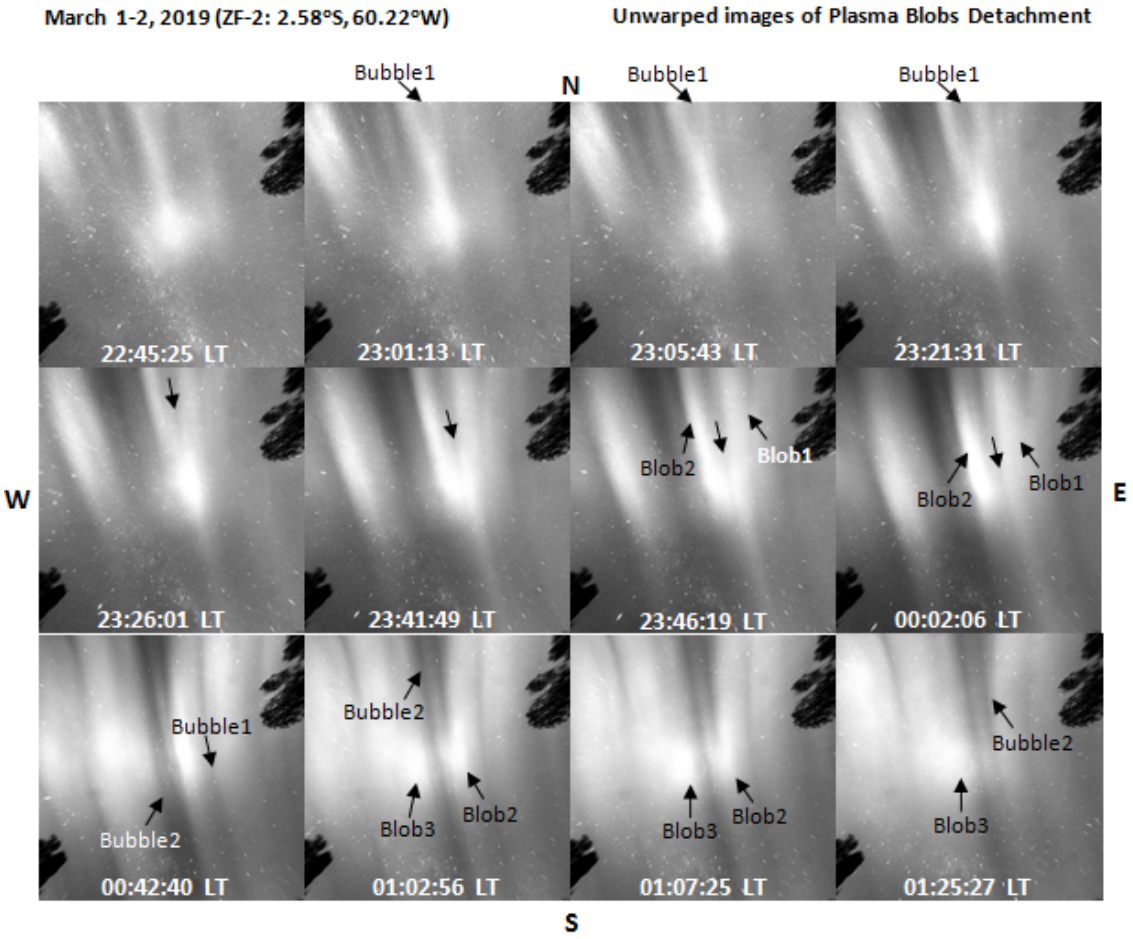

SOURCE: Author.

Figure 5.20 is the unwarped sequential images of plasma blobs detachment and it corresponds to the 1024 × 1024 km at the altitude of about 300 km. It shows the development of the bubble causing the blob to split and eventually detached another blob from the main blob. The Blob1, as shown in Figure 5.20, starts to show a 'fork-like' with two legs shape at 23:21:31 LT and this is as a result of the growing 'Bubble1' at the northern edge of the field of view. As this bubble grows bigger, the two legs of 'Blob1' experiences a wider separation angle and the 'Bubble1' becomes more glaring on the field of view - see 23:46:19 LT. At 00:02:06 LT, we can

see the two blobs separately - 'Blob1' and 'Blob2'.

5.4 Ionosonde results

On October 6-7, 1999, during HSA (22.7^{o}S, 45.0^{o}W), plasma blobs associated with plasma bubbles were observed, Figure 5.21, and the behavior of ionospheric parameters during the occurrence was investigated. From Figure 5.22, blobs and bubbles started around 23:00:00 UT and this shows a decrease in both the F-region minimum virtual height (h'F) and F-region peak height, hmF2, but an increase in F-region critical frequency (foF2). The ionosonde has a threshold critical frequency which is 17 MHz at night period, and above which the frequency is cut-off. This is because frequency above is not expected at the night period. Consequently, during the occurrence of plasma blobs and bubbles, there were many cut-off frequency and this shows as a flat top in the figures. Having checked through the normal behavior of these parameters in the absence of irregularities by visualizing data of days without plasma blobs, we have observed a common trend of behaviour of these parameters to the presence of plasma blobs and plasma bubbles in the F-region ionosphere. When the critical frequency, foF2 is low, both the minimum virtual height, h'F, and peak height, hmF2 increases. Whereas, when the critical frequency, foF2, is very high, both the minimum virtual height, h'F, and peak height, hmF2 decreases rapidly. During the occurrence of plasma blobs and plasma bubbles the critical frequency, foF2, increases beyond the threshold. The arrow at Figure 5.22(c) indicates the period when both plasma bubbles and plasma blobs drifted away from the field of view momentarily but later appeared again which is the increment just at the right side of the arrow.

Figure 5.21 - Sequential unwarped all-sky images obtained during October 6-7, 1999, showing the occurrence of a plasma blob event in the OI 630.0 nm emission.

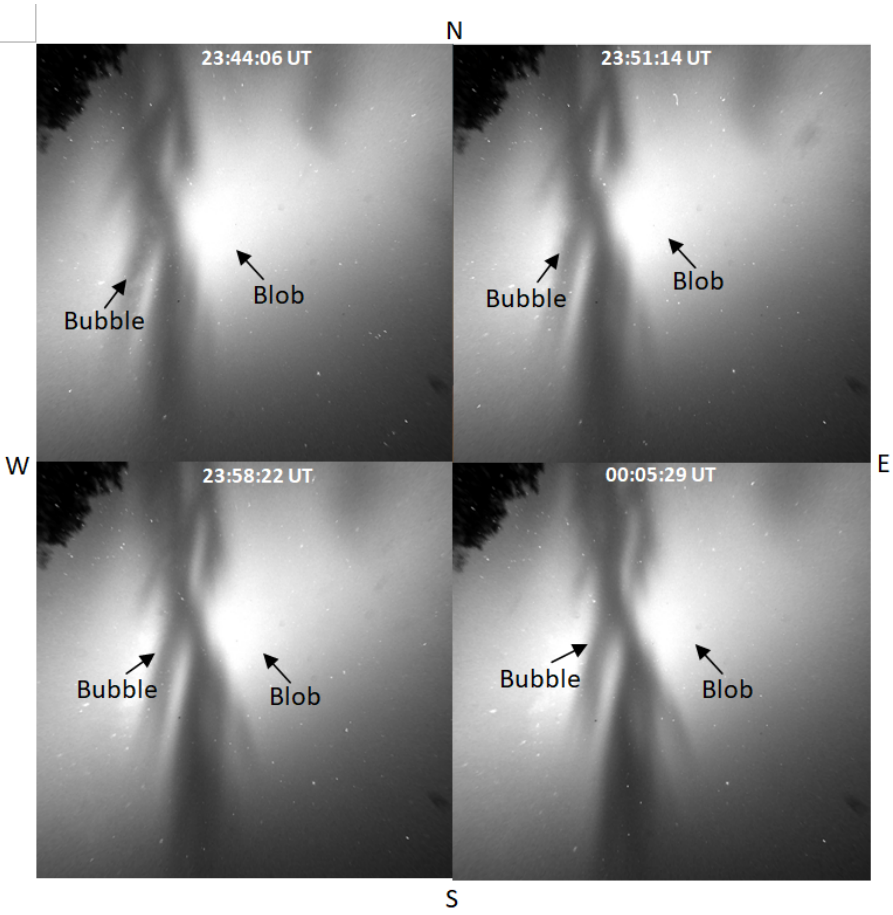

SOURCE: Author.

Figure 5.22 - The behavior of ionospheric parameters on October 6-7, 1999 during the occurrence of plasma blobs associated with plasma bubbles. The dotted line represents the time of occurrence of the irregularities. (a) F-region peak height (hmF2); (b) F-region minimum virtual height (h'F); and (c) critical frequency of the F-layer (foF2).

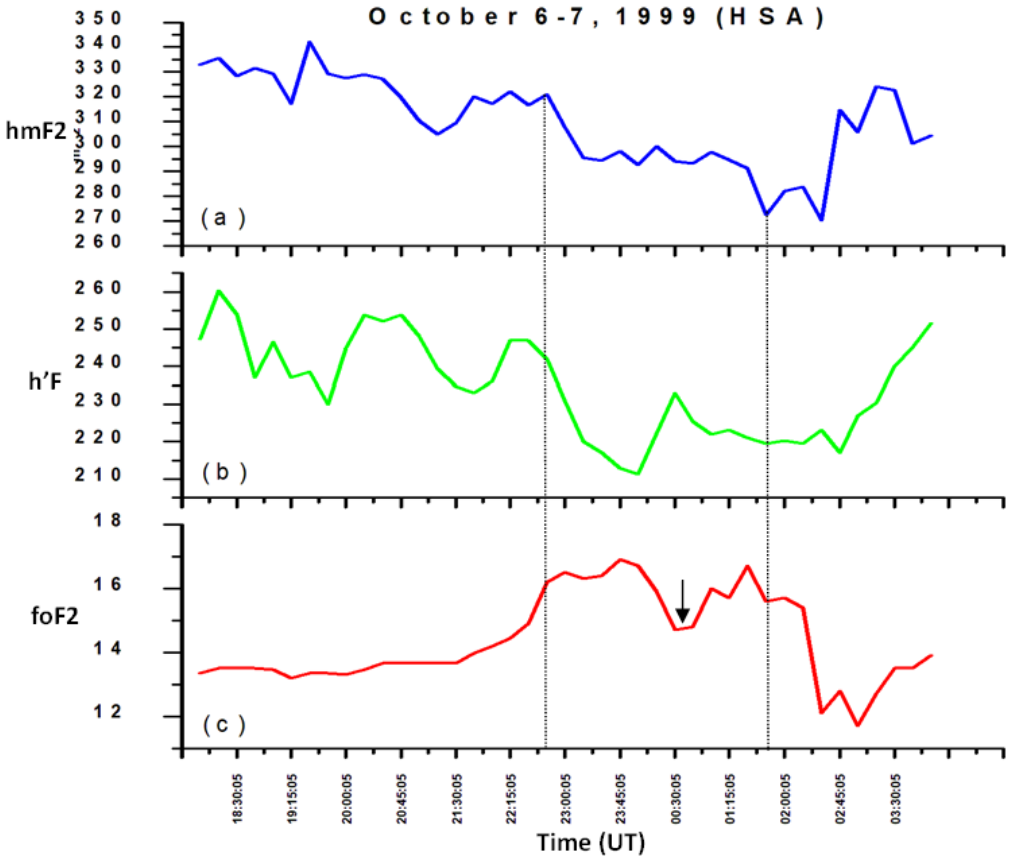

SOURCE: Author.

Similarly, on March 4-5, 2000, at around 22:30:00 UT to 02:00:00 UT, during HSA (22.7^{o}S, 45.0^{o}W), intense plasma bubbles and plasma blobs were observed and the behavior of the ionospheric parameters during these periods was investigated. The F-region peak height, hmF2, and minimum virtual height, h'F, decreases while the critical frequency of the F region, foF2, maintains a flat around the threshold frequency. This implies that if the critical frequency, foF2, were to be without the threshold the extent to which the presence of plasma bubbles and plasma blobs affect this parameter could have be seen clearly. Pimenta et al. (2004), using radio technique to study plasma blobs and the first observation over the Brazilian sector, reported an out-of-scale critical frequency, foF2, during the occurrence of plasma

blobs.

Figure 5.23 - The behavior of ionospheric parameters on March 4-5, 2000 during the occurrence of plasma blobs associated with plasma bubbles. The dotted line represents the time of occurrence of the irregularities. (a) F-region peak height (hmF2); (b) F-region minimum virtual height (h'F); and (c) critical frequency of the F-layer (foF2).

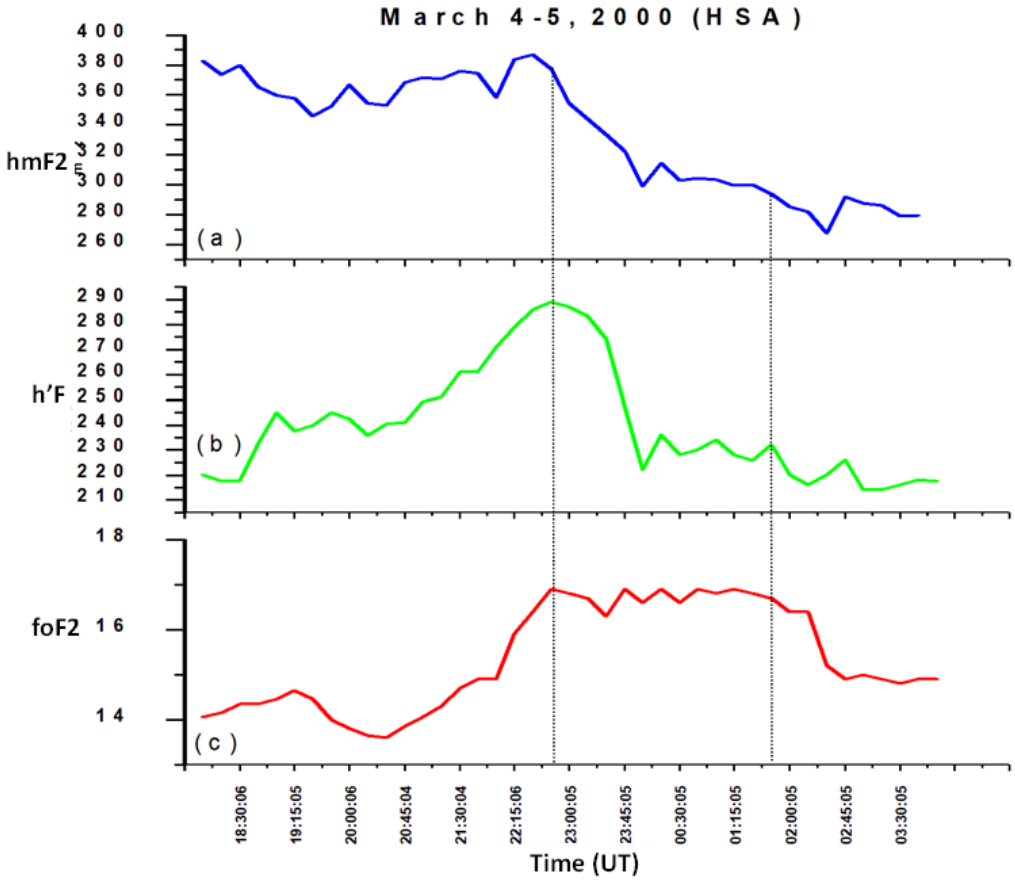

SOURCE: Author.

5.5 Satellite observations

On March 1, 2019, at 21:40:04 - 00:51:40 LT, plasma bubbles and plasma blobs were observed on the all-sky imager at ZF-2 ($2.58^oS,\ 60.22^oW$) during low solar activity. This location is 4 hours behind the Universal Time (UT). Hence, converting the timezone we got satellite data for March 2, 2019, at 21:34:10 - 21:39:23 LT. Satellite A and C move from North to South spending 5.22 minutes over the latitudinal range

of 10^{o}N to 10^{o}S and longitudinal range of 60.35^{o}S to 60.72^{o}S, respectively. Figure 5.24 shows the trajectory of satellite A on March 2, 2019. The temporal position of the satellite while at 10^{o}N to 10^{o}S was tracked and shown in the right image below. The image is a screenshotted image of the Virtual Research Environment (VRE) for SWARM mission (PEDROSA; TRIEBNIG, 2016).

Figure 5.24 - The figure shows the trajectory of SWARM satellite A on March 2, 2019, at 21:34:10 - 21:39:23 LT. The image shows the web interface of Virtual Research Environment (VRE) for the SWARM mission and presents a unique opportunity to track the trajectory and visualize the satellite's geographical location at a particular time.

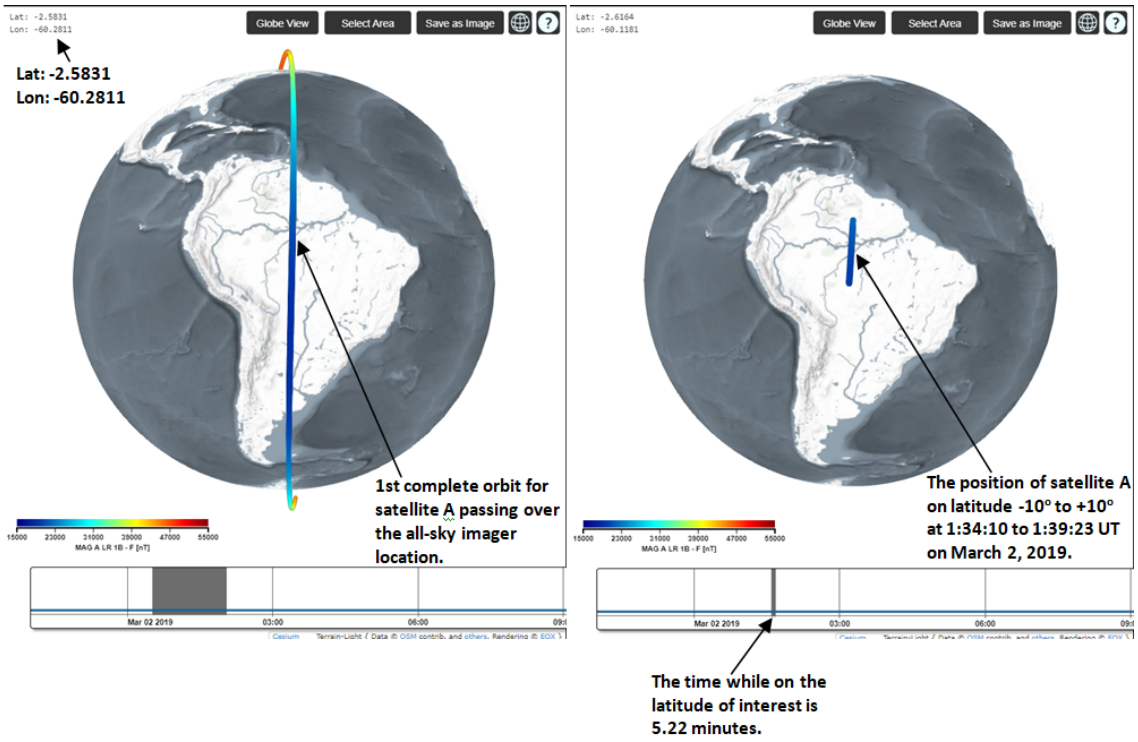

SOURCE: Author.

Figure 5.25 - The figure shows the corresponding plasma bubbles and plasma blobs observed on the all-sky imager on March 1, 2019, at 21:40:04 - 21:44:33 LT. (a) and (b) are the early-stage development of both plasma bubble and plasma blob as they both drift at the northern edge of the field of view. (c) and (d) are the fully developed phase of both this bubble and blob on this day.

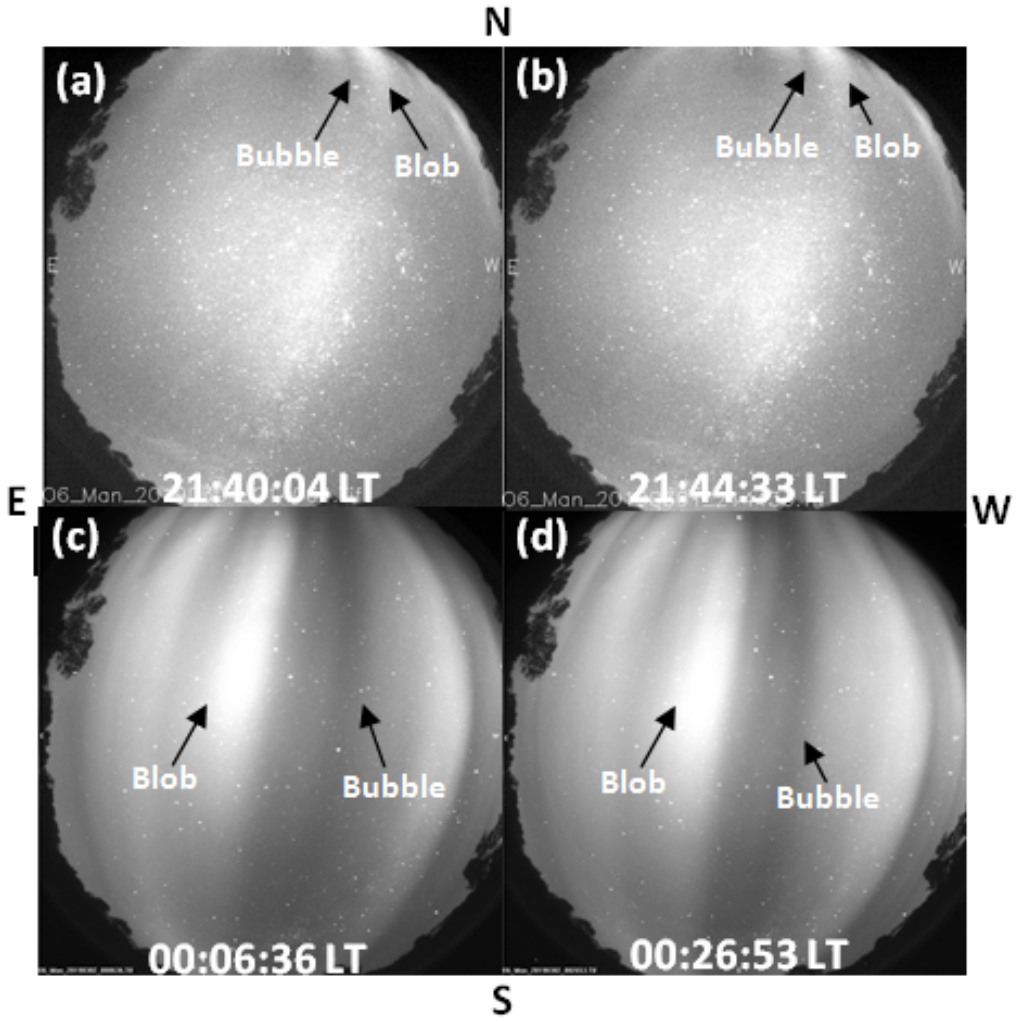

SOURCE: Author.

Figure 5.26 - Plasma enhancements, blobs, associated with plasma depletions, bubbles, observed by SWARM satellite A on March 2, 2019, at 21:34:10 LT - 21:39:23 LT corresponding to the all-sky imager observation on March 1, 2019, at 21:28:47 LT - 21:44:33 LT. Electron density inside the blobs is twice above the background electron density.

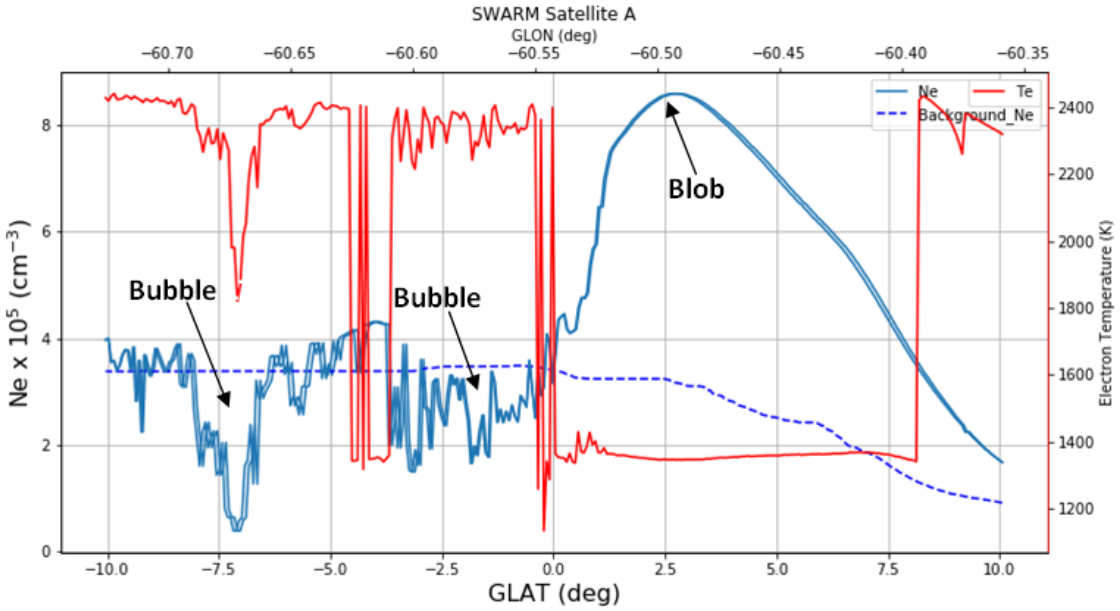

SOURCE: Author.

Figure 5.26 shows the electron density, Ne, and electron temperature, Te, from SWARM satellite (A) data on March 2, 2019 at 21:34:10-21:39:23 LT. The magnetic activity was weak with an average Dst > -21.45 nT. From the figure, we can clearly see the plasma depletion and enhancements. Plasma depletion shows a latitudinal spread but plasma enhancements show a peak at about 2.5^{o}N geographic latitude (MLT: 21.50^{o}N, around the equatorial ionization anomaly region). Considering the trajectory of the satellites (see Figure 5.24), North to South, the satellite observed the enhancements firstly thereafter the depletions. An approximately 2.2 (225%) increase in electron density above the background density was observed by the satellite for the enhancements, and the electron temperature decreases and also fluctuates inside the bubbles but decreases with no fluctuation inside the blob. compared to the background temperature. In other words, bubbles display non-homogeneity while blob displays homogeneity. This kind of observations should be further investigated. However, Le et al. (2003) reported a decrease in electron temperature for both

plasma bubble and plasma blob using KOMPSAT-1 and DMSP F15 satellite data. This spatial extension behaviour of plasma blobs is in agreement with their feature observed on the all-sky imager; their N-S extension almost doubles their E-W extension. The electron density inside blobs has been reported to be increased by a factor of 2 or 3 (WATANABE; OYA, 1986; LE et al., 2003; PARK et al., 2003; PIMENTA et al., 2004).

Figure 5.27 - Plasma enhancements, blobs, associated with plasma depletions, bubbles, observed by SWARM satellite C with the same nomenclature as Figure 5.26.

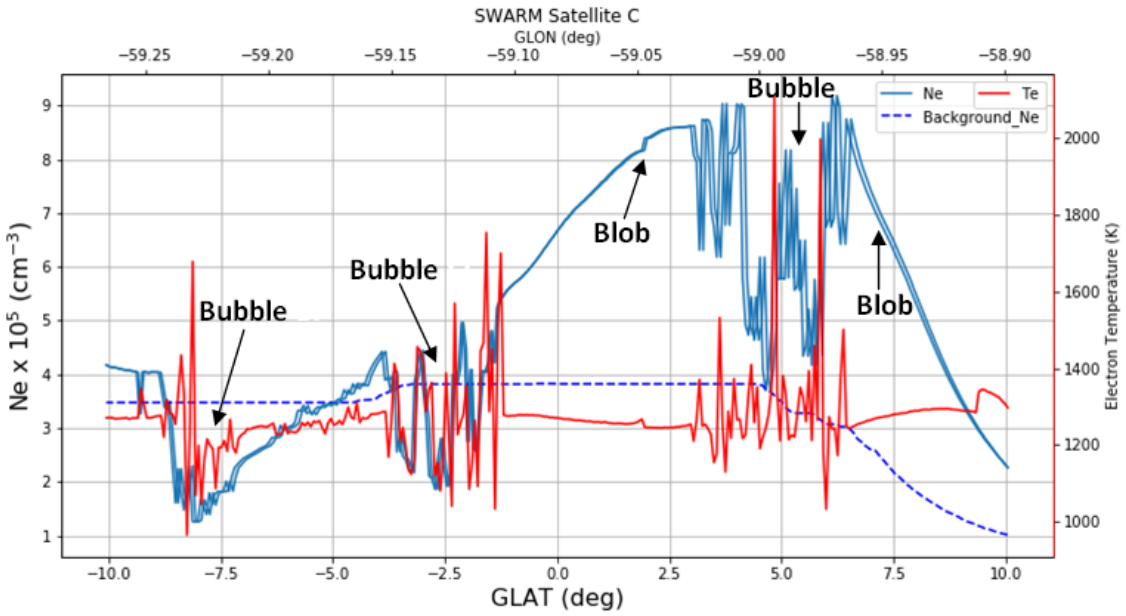

SOURCE: Author.

Simultaneously orbiting with Satellite A was Satellite C with a zonal separation of 1.4^o. The satellite observed similar results to that of A. They both have their highest enhancements at 2.5^{o}N but satellite C appeared to have detected another plasma depletions at around 5.0^{o}N while satellite A decline slowly to the background electron density. An approximately 2.3 (229%) increase in electron density above the background density was observed by this satellite for the enhancements and the electron temperature is quite similar to Satellite A with fluctuations of electron temperature inside the bubble but a steady drop in electron temperature inside the blob. The background electron temperature is lower, around 1300 K, than the

background electron temperature of Satellite A.

Figure 5.28 - The normal behavior of electron density at the latitudinal range of interest in the absence of plasma bubbles and plasma blobs on March 2, 2019, at Indian (10:57 AM), Amazona (9:14 AM), and Chad (9:14 PM). None of the figures shows the magnitude of the electron density as observed during the irregularities.

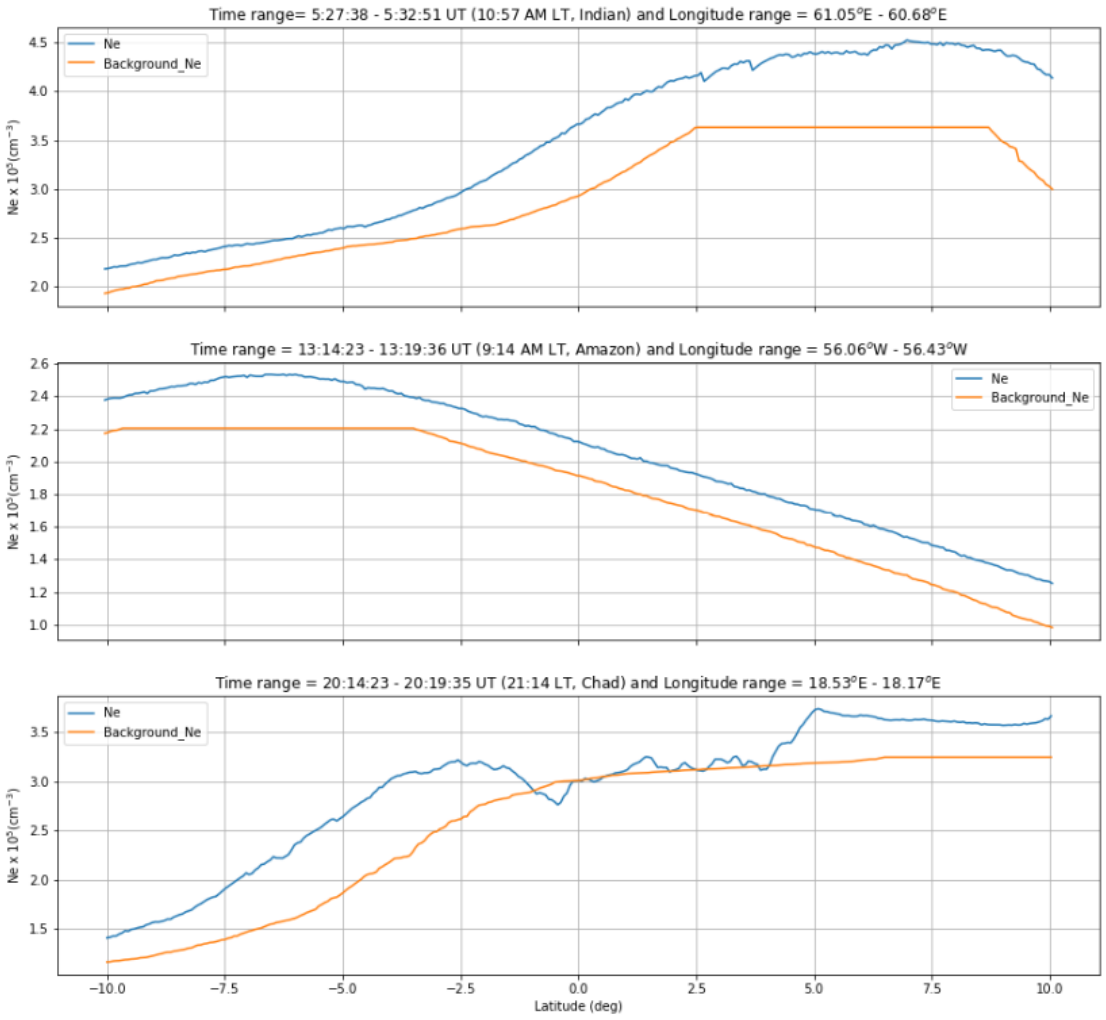

SOURCE: Author.

Having evaluated the behavior of electron density for the same range of latitude of interest at different times on the same day, we have come to conclude that the phenomena observed are indeed plasma depletions, bubbles, and plasma enhance-

ments, blobs, as seen on the all-sky imager. Figure 5.28 shows an example of three cases at different times and locations on the same day that the phenomena were observed. At 10:57 AM LT, the electron density is quite close to the background electron density during the period of the irregularities at the same latitudinal range. The maximum electron density at this time at $2.5^{o}N$ was around $4.1 \times 10^{5}\ cm^{-3}$. Whereas, the electron density at this same latitude during the occurrence of plasma blobs was $8.5 \times 10^{5}\ cm^{-3}$; about twice increment. Also, the electron density behavior was examined at another location (Amazon, 9:14 AM LT), the electron density was lower as compared to the Indian at 10:57 AM LT. This is reasonable because in the morning there is lower ionization and, hence, lower electron density. And lastly, at 9:14 PM LT in Chad, the maximum electron density was about $3.8 \times 10^{5}\ cm^{-3}$ with little distortion in electron density.

Figure 5.29 - The SWARM satellites A and C with separation in longitude of 1.4^{o}. Thus, the satellites observed similar results but at different geographical longitude due to their zonal separation. The Pearson correlation on the electron density for both satellites was +0.787 and it shows a good positive linear relationship between the two satellites.

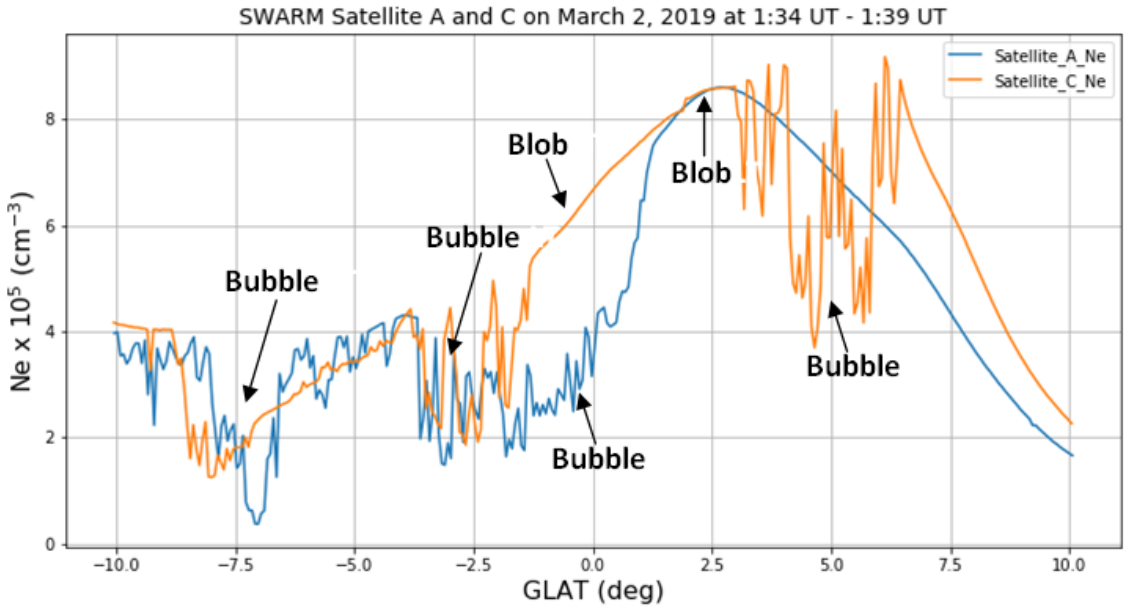

SOURCE: Author.

From Figure 5.29, the behavior of electron density on March 2, 2019, as observed

by SWARM constellation satellites (A and C) can be seen clearly. The two satellites were on the same geographical latitude (10^oN to 10^oS) at 21:34:04 - 21:39:23 LT with 6 seconds different in time but different longitude with difference of 1.4^o: A (60.35^oW to 60.72^oW) and C (58.89^oW to 59.26^oW) as seen in Figure 4.7. In this work, the North-South spatial extension of plasma blobs, during LSA, had been averagely estimated to be 110-230 km ($\approx 1^o$-2^o). It takes 6 seconds for the adjacent satellites to cross the same geographical latitude. Therefore, if the two satellites observe plasma blobs and plasma bubbles at the same geographical latitude, it is highly probable that they encounter different parts of the same plasma blobs and plasma bubbles structure. The two phenomena drift side by side together (longitudinally), as seen on the all-sky imager, then it is probable that one satellite observes better a phenomenon than the adjacent satellite or one observing the opposite phenomenon of the other due to the zonal separation. The plasma bubbles have a full North-South extension and wider East-West extension compared to plasma blobs. Therefore, plasma bubbles cover longer latitude and longitude than plasma blobs. The Pearson correlation on the two satellites' electron density data was +0.787; quite high.

Now, from Figure 5.29, for satellite A, the depletions spread over longer latitude but the enhancements possess a shorter latitude coverage. Similarly, satellite C encountered an enhancement from around 10^oN through around 6.0^o after which it encountered big depletions with its electron density dropping to twice its initial peak. And just after coming out of the depletion, it encountered another enhancement because the electron density is not, suddenly, back to the background density but instead, very slowly, drops in electron density before encountering another depletions. I suppose the plasma enhancements encountered by Satellite C had the same 'ridge-like' structure as Satellite A but probably, a depletion developed underneath which eventually split the enhancement into two parts, seeing as both enhancements besides the depletion. This observation is quite similar to the mechanism for the relationship between plasma depletions and enhancements proposed by Huang et al. (2014) where they reported plasma depletion, as it grows, splitting plasma enhancement into two parts to North and South of magnetic dip latitude. Le et al. (2003) reported plasma blobs in situ observed by ROCSAT-1 in the EIA crest region coexisting with EPB observed by DMSP near the magnetic equator. They suggested that blobs in the EIA regions are caused by the polarization electric field, which was generated within EPBs and mapped to the EIA regions along the magnetic field lines.

5.6 Blobs observed over Cachoeira Paulista

On August 27-28, 1987 with the all-sky imager 1, as stated earlier in chapter 3, plasma blob without plasma bubble, was observed from 25:30 LT through 27:20 LT (PIMENTA et al., 2011). The sequential image, Figure 5.30, shows the plasma developing at around 23:30 LT and drift eastward of the field of view. On this night the geomagnetic activity was moderately disturbed with Dst > -70 nT. Plasma blobs generate from the northern edge of the view (equator) and drift towards the zenith of the all-sky imager location. But, probably, plasma mapping along the geomagnetic field lines from the equator towards low-latitudes experience an opposite force by the meridional wind blowing from South towards the equator which, as a result, causes the plasma to scatter as seen in Figure 5.30. In the earlier observed blob, for instance, Figure 4.4, they are properly aligned with the field lines due to the absence of geomagnetic storm (which causes the wind to blow against the plasma along the field lines). Moreover, nocturnal variation is quite similar to the time of appearance of plasma blobs as observed during LSA in this study.

Figure 5.30 - The figure shows the sequential image of plasma blobs observed at Cachoeira Paulista in August 27-28, 1987.

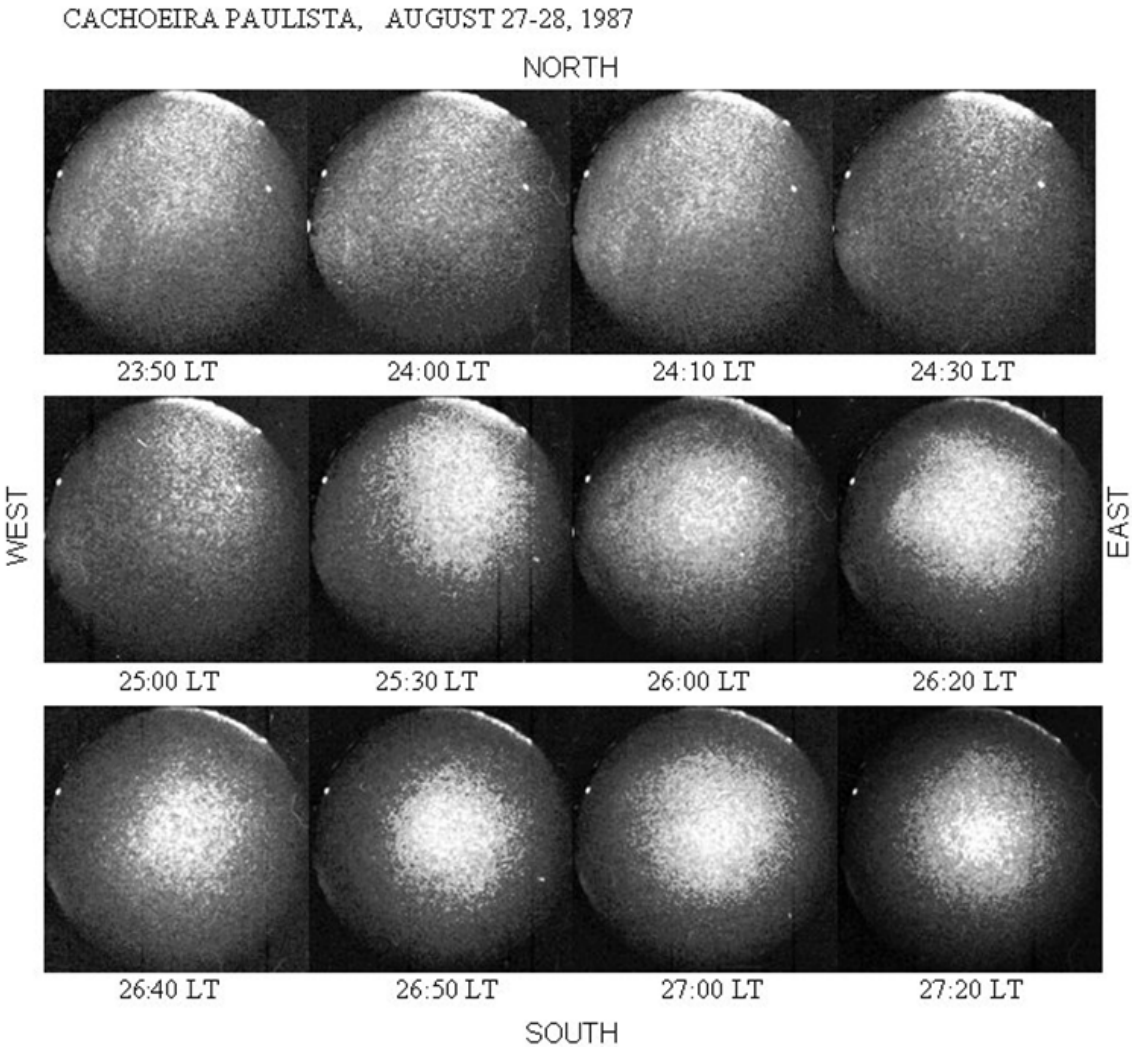

SOURCE: Pimenta et al. (2011).

During the occurrence of this plasma blob, August 27-28, 1987, ionosonde data was used to verify the behavior of the ionospheric parameters; critical frequency, foF2, F-region peak height, hmF2, and virtual base height, h'F. From Figure 5.31 the critical frequency, foF2, increased but both the F-region peak height, hmF2, and virtual base height, h'F decreased during the occurrence of plasma blobs in the ionosphere. This result is in agreement with our earlier results obtained for HSA where these parameters displayed the same pattern.

Figure 5.31 - The figure shows the behaviour of ionospheric parameters during the occurrence of plasma blobs observed over Cachoeira Paulista in August 27-28, 1987.

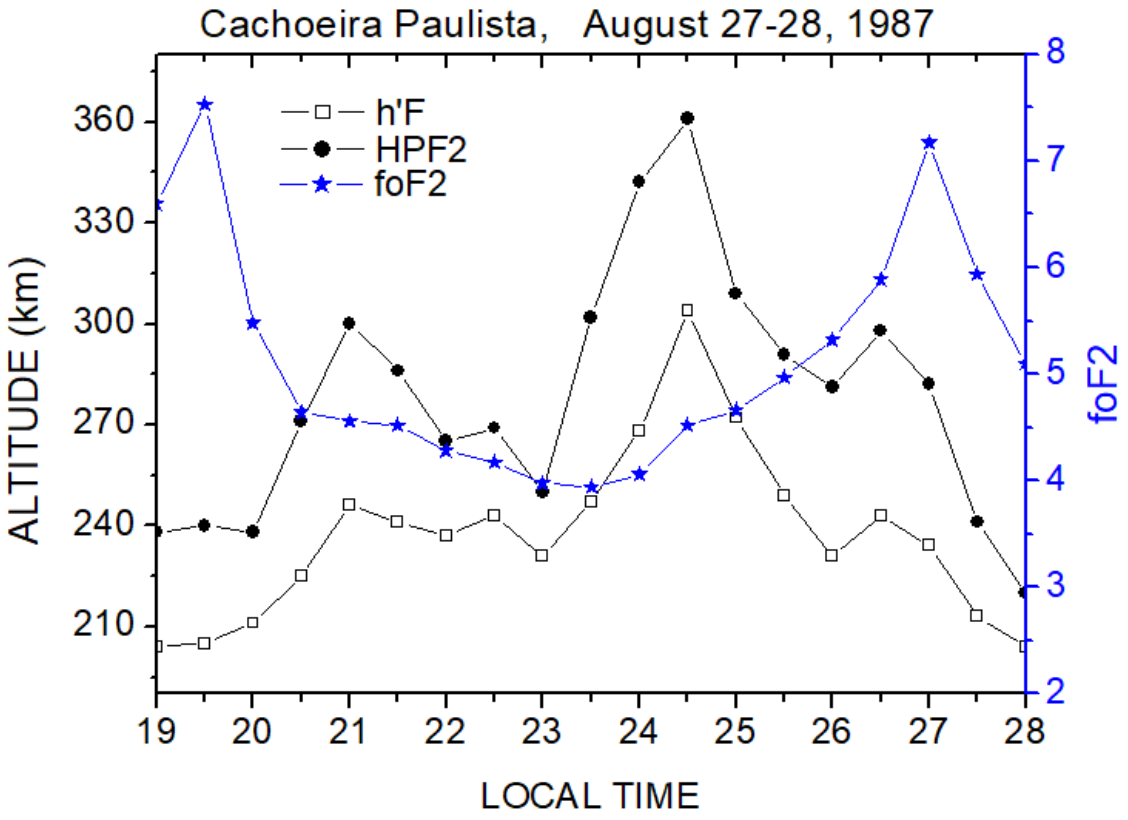

SOURCE: Pimenta et al. (2011).

6 CONCLUSIONS

In this research we have studied the occurrence pattern of plasma enhancements, blobs, and their association with the plasma depletions, bubbles, using all-sky imagers, ionosonde, and SWARM constellation satellite during high solar activity (HSA) and low solar activity (LSA). More than 3000 images were analyzed and the occurrences of plasma blobs and plasma bubbles were studied. These occurrences were used to study the solar cycle, seasonal, nocturnal, and monthly variations, and some evolutionary features of plasma blobs. In addition, ionosonde data and SWARM constellation data (satellite A and C) were used as complementary data to the all-sky imager. Considering some discrepancies about the relationship between these two phenomena, we have discovered a strong relationship between the plasma bubbles and plasma blobs using various instrumentation for the accuracy of the work. Plasma blobs have been discovered to be related strongly to the equatorial plasma bubbles. These two phenomena have been observed together simultaneously with all-sky imagers, ionosonde, and multisatellites.

Two different all-sky imagers, observing OI 630.0 nm, located at different parts of Brazil, both in the tropical region, were used to study the occurrence pattern of plasma blobs during HSA and LSA. This occurrence pattern was carried out for both HSA and LSA by considering the hours of observation and the hours of the occurrence of plasma blobs for each day, month, and season. Plasma blobs seasonal occurrence pattern is highest during summer followed by autumn, spring and lowest during winter for both LSA and HSA. Exceptionally, occurrence pattern of blob in winter during HSA is higher than LSA, and this was due to geomagnetic storm that occurred in this period. Similarly, for plasma bubbles, the seasonal occurrence pattern is highest during summer followed by autumn, spring and lowest during winter for both LSA and HSA. There were two cases of plasma bubbles in June 2000 and one of them was observed during a moderate geomagnetic storm of Dst $>$ -75 nT. And also there was a severe geomagnetic storm on one of the events observed on April 6, 2000, with Dst $>$ -292 nT. The occurrence frequency of plasma bubbles is very low during winter of the Southern hemisphere and this is closely similar to the previous works.

To study the nocturnal variation of plasma blobs and plasma bubbles we considered the time of their appearance and disappearance from the field of view of the all-sky imagers. Each time of the occurrence of plasma blobs and bubbles was rounded up to the nearest hour. Plasma blob had the highest occurrence frequency of its ap-

pearance at 22:00 LT and 23:00 LT during HSA and LSA, respectively. And had its disappearance occurrence frequency highest at 23:00 LT and 24:00 LT during HSA and LSA respectively. Just an approximately one-hour difference, implying a short lifetime of the blob. Whereas plasma bubbles had their highest occurrence frequency of appearance at 20:00 LT and 23:00 LT during HSA and LSA, respectively. And had its highest disappearance occurrence frequency at 24:00 LT and 25:00 LT respectively. The average hours of the occurrence of plasma blobs on the imager's field of view were 1.08 hours and 0.57 hours during HSA and LSA, respectively, while the average hours of the occurrence of plasma bubble were 4.01 hours and 2.19 hours during HSA and LSA, respectively. Thus, plasma blobs have a shorter lifetime compared to plasma bubbles and they are both likely to be formed just after the post-sunset; plasma blob, through the physical observation, seems to get fully developed at midnight hours (around 24:00 LT).

The zonal drift velocity and spatial extension of plasma blobs during HSA and LSA were estimated using the average value of four different months in January, March, October, and December. The average zonal drift velocity of plasma blobs was 61 $\pm$ 21 m/s and 67 $\pm$ 27 m/s during HSA and LSA, respectively. While its E-W extension was 54-83 km and 41-81 km during HSA and LSA, respectively, and its N-S extension was 87-129 km and 110-230 km during HSA and LSA, respectively. Thus, plasma blobs have almost the same zonal drift velocity but extended more longitudinal (N-S) than latitudinal (E-W). The bigger scale-size of blob in N-S could be result of easier movement of ions and electrons along the geomagnetic field lines (meridional motion) than perpendicular to these field lines (zonal motion).

For the first time, we have observed some relevant evolutionary aspects of plasma enhancements with all-sky imagers and these were plasma blobs merging and plasma blobs detachment. Plasma blobs are confined at a lower altitude, unlike plasma bubbles that rise to higher altitude. We propose that plasma blobs drifting eastward would experience various retarding forces such as gravity, pressure gradient, and east to west induced polarized electric field. Consequently, they tend to slow down momentarily until the succeeding blobs meet up and merge together because the succeeding blobs appear to have been drifting with an increasing momentum; smaller blobs merge with bigger blobs. We have observed this mechanism to be responsible for the fully developed plasma blobs in this research. We also proposed that, a big plasma blob along the magnetic field lines would merge with another succeeding smaller blob when its scale size (E-W extension) is above a certain threshold and the decrease in velocity of zonal neutral wind with time and gravitational force

could be responsible for this process. Plasma blobs were observed to be splitting and eventually detached from one another. This detachment has been attributed to a developing plasma bubble underneath the plasma blob. The plasma blob splits as the plasma bubble, observed to be responsible, grows in magnitude from the northern edge towards the southern edge of the field of view. Eventually divided the blob into two parts. As this is the first observation of these kinds of features of plasma blobs, further investigations should be carried out for proper understanding of plasma blobs. These kinds of studies are important and possess a great potential for revealing the mechanism responsible for the formation of blobs in the nighttime ionosphere. Also, numerical simulation of plasma blobs, considering some factors observed in this work, may reveal accurate mechanism responsible for these features of ionopsheric plasma blobs.

Plasma enhancements associated with plasma depletions were also observed by SWARM constellation (A and C) simultaneously with the all-sky imager observation. The two satellites were at around 460 km altitude and zonal separation of 1.4^o. They moved from North to South and spent 5.22 minutes at the latitudinal range of 10^oN and 10^oS. The Pearson correlation analysis (+0.787) on the two satellites confirmed that they were both observing similar structures. Having verified the structures observed by the SWARM constellation with their reported characteristics, we concluded that the structures were plasma blobs and plasma bubbles as observed on the all-sky imager. The plasma depletions covered a wider latitude (full north-south structure on all-sky imager) but plasma enhancements covered a shorter latitude. Electron density inside the enhancement increased above twice of the background value. And the electron temperature decreases inside both the blob and the bubble. However, we noticed that plasma bubbles are non-homogenous as observed by the fluctuations of the electron temperature inside the bubbles while plasma blobs are homogenous as observed by the steady-state nature of the electron temperature inside the blob. Further investigations should be carried out to study this kind of the behaviour of electron temperature inside both the bubbles and blobs.

Finally, we have come to conclude that plasma blobs have a close and causal relationship with the equatorial plasma bubbles and the occurrence of plasma blobs at the tropical is as a result of the presence of plasma bubbles. Thus, plasma blob can be defined as a region of abrupt accumulated plasma in the F-region nighttime ionosphere caused mainly by the interaction between the evolution of large-scale plasma irregularity (bubbles) and the restorative forces.

REFERENCES

ABDU, M.; SOBRAL, J.; NELSON, O.; BATISTA, I. Solar cycle related range type spread-f occurrence characteristics over equatorial and low latitude stations in Brazil. **Journal of Atmospheric and Terrestrial Physics**, v. 47, n. 8-10, p. 901–905, 1985. 68

ABDU, M.; SOUZA, J.; BATISTA, I.; SOBRAL, J. Equatorial spread f statistics and empirical representation for iri: a regional model for the brazilian longitude sector. **Advances in Space Research**, v. 31, n. 3, p. 703–716, 2003. 70, 76

ABDU, M. A.; BHATTACHARYYA, A.; PANCHEVA, D. **Aeronomy of the Earth's Atmosphere and Ionosphere**. [S.l.]: Springer Science & Business Media, 2011. 17

ANDERSON, D.; MENDILLO, M. Ionospheric conditions affecting the evolution of equatorial plasma depletions. **Geophysical Research Letters**, v. 10, n. 7, p. 541–544, 1983. 52

BANKS, P. **G. Kockarts, Aeronomy**. [S.l.]: New York: Academic Press, 1973. 13, 14

BARROS, D.; TAKAHASHI, H.; WRASSE, C. M.; FIGUEIREDO, C. A. O. Characteristics of equatorial plasma bubbles observed by tec map based on ground-based gnss receivers over south america. In: **Annales Geophysicae**. [S.l.: s.n.], 2018. v. 36, n. 1, p. 91–100. 3, 16, 20, 22

BASU, S.; GROVES, K.; BASU, S.; SULTAN, P. Specification and forecasting of scintillations in communication/navigation links: current status and future plans. **Journal of a Atmospheric and Solar-Terrestrial Physics**, v. 64, n. 16, p. 1745–1754, 2002. 16

BATISTA, I.; MEDEIROS, R. D.; ABDU, M.; SOUZA, J. D.; BAILEY, G.; PAULA, E. D. Equatorial ionospheric vertical plasma drift model over the brazilian region. **Journal of Geophysical Research: Space Physics**, v. 101, n. A5, p. 10887–10892, 1996. 82

BAUMJOHANN, W.; TREUMANN, R. **Basic space plasma physics**. [S.l.]: World Scientific, 1996. 13, 14, 15

BITTENCOURT, J. A. **Fundamentals of plasma physics**. [S.l.]: Springer Science & Business Media, 2013. 1, 8, 10, 13

BOOKER, H.; WELLS, H. Scattering of radio waves by the f-region of the ionosphere. **Terrestrial Magnetism and Atmospheric Electricity**, v. 43, n. 3, p. 249–256, 1938. 17

CAMPBELL, W. H. **Introduction to geomagnetic fields**. [S.l.]: Cambridge University Press, 2003. 6, 7

CHOI, H.-S.; KIL, H.; KWAK, Y.-S.; PARK, Y.-D.; CHO, K.-S. Comparison of the bubble and blob distributions during the solar minimum. **Journal of Geophysical Research: Space Physics**, v. 117, n. A4, 2012. 2, 9, 36, 54

DALGARNO, A.; WALKER, J. C. The red line of atomic oxygen in the day airglow. **Journal of the Atmospheric Sciences**, v. 21, n. 5, p. 463–474, 1964. 39

GARCIA, F.; TAYLOR, M. J.; KELLEY, M. Two-dimensional spectral analysis of mesospheric airglow image data. **Applied Optics**, v. 36, n. 29, p. 7374–7385, 1997. 3, 39, 54, 56

GURAV, O.; NARAYANAN, V.; SHARMA, A.; GHODPAGE, R.; GAIKWAD, H.; PATIL, P. Airglow imaging observations of some evolutionary aspects of equatorial plasma bubbles from indian sector. **Advances in Space Research**, v. 64, n. 2, p. 385–399, 2019. 1, 2, 92

HOFMANN-WELLENHOF, B.; LICHTENEGGER, H.; WASLE, E. **GNSS–global navigation satellite systems: GPS, GLONASS, Galileo, and more**. [S.l.]: Springer Science & Business Media, 2007. 15, 22

HUANG, C.-S.; LE, G.; BEAUJARDIERE, O. de L.; RODDY, P.; HUNTON, D.; PFAFF, R.; HAIRSTON, M. Relationship between plasma bubbles and density enhancements: observations and interpretation. **Journal of Geophysical Research: Space Physics**, v. 119, n. 2, p. 1325–1336, 2014. 2, 24, 36, 37, 107

KAMIDE, Y.; CHIAN, A. C.-L. **Handbook of the solar-terrestrial environment**. [S.l.]: Springer Science & Business Media, 2007. 5

KELLEY, M. C. **The Earth's ionosphere: plasma physics and electrodynamics**. [S.l.]: Academic Press, 2009. 1, 12, 13, 17, 21, 22

KHOMICH, V. Y.; SEMENOV, A. I.; SHEFOV, N. N. **Airglow as an indicator of upper atmospheric structure and dynamics**. [S.l.]: Springer Science & Business Media, 2008. 39

KIL, H. The morphology of equatorial plasma bubbles–a review. **Journal of Astronomy and Space Sciences**, v. 32, n. 1, p. 13–19, 2015. 2

KIL, H.; CHOI, H.-S.; HEELIS, R.; PAXTON, L.; COLEY, W.; MILLER, E. Onset conditions of bubbles and blobs: aa case study on 2 march 2009. **Geophysical Research Letters**, v. 38, n. 6, 2011. 2

KIL, H.; PAXTON, L. J.; JEE, G.; NIKOUKAR, R. Plasma blobs associated with medium-scale traveling ionospheric disturbances. **Geophysical Research Letters**, v. 46, n. 7, p. 3575–3581, 2019. 2, 26, 36

KRALL, J.; HUBA, J.; JOYCE, G.; YOKOYAMA, T. Density enhancements associated with equatorial spread f. **Annales Geophysicae**, v. 28, n. 2, 2010. 2, 24, 25, 36, 38, 86

LE, G.; HUANG, C.-S.; PFAFF, R.; SU, S.-Y.; YEH, H.-C.; HEELIS, R.; RICH, F.; HAIRSTON, M. Plasma density enhancements associated with equatorial spread f: Rocsat-1 and dmsp observations. **Journal of Geophysical Research: Space Physics**, v. 108, n. A8, 2003. 24, 25, 36, 85, 103, 104, 107

LUO, W.; XIONG, C.; ZHU, Z.; MEI, X. Onset condition of plasma density enhancements: a case study for the effects of meridional wind during 17–18 august 2003. **Journal of Geophysical Research: Space Physics**, v. 123, n. 8, p. 6714–6726, 2018. 2

MARUYAMA; TAKASHI. Ionosphere and thermosphere. **Journal of Communications Research Laboratory**, v. 49, n. 3, p. 163, 2002. 18, 19, 20

MARUYAMA, T. Observations of quasi-periodic scintillations and their possible relation to the dynamics of e s plasma blobs. **Radio Science**, v. 26, n. 03, p. 691–700, 1991. 25

MENDILLO, M.; SPENCE, H.; ZALESAK, S. Simulation studies of ionospheric airglow signatures of plasma depletions at the equator. **Journal of Atmospheric and Terrestrial Physics**, v. 47, n. 8-10, p. 885–893, 1985. 52

MENDILLO, M.; TYLER, A. Geometry of depleted plasma regions in the equatorial ionosphere. **Journal of Geophysical Research: Space Physics**, v. 88, n. A7, p. 5778–5782, 1983. 1, 2, 52

MILLER, E.; KIL, H.; MAKELA, J.; HEELIS, R.; TALAAT, E.; GROSS, A. Topside signature of medium-scale traveling ionospheric disturbances. In: **Annales Geophysicae**. [S.l.: s.n.], 2014. v. 32, n. 8, p. 959–965. 2

MOORE, J.; WEBER, E. Oi 6300 and 7774 Å airglow measurements of equatorial plasma depletions. **Journal of Atmospheric and Terrestrial Physics**, v. 43, n. 8, p. 851–858, 1981. 1, 2

ONDOH, T.; MARUBASHI, K. **Science of space environment**. [S.l.]: IOS Press, 2001. 20

OSSAKOW, S.; ZALESAK, S.; MCDONALD, B.; CHATURVEDI, P. Nonlinear equatorial spread f: Dependence on altitude of the f peak and bottomside background electron density gradient scale length. **Journal of Geophysical Research: Space Physics**, v. 84, n. A1, p. 17–29, 1979. 2, 26, 27, 31, 32, 34, 35, 86

OSSAKOW, S. L.; CHATURVEDI, P. Morphological studies of rising equatorial spread f bubbles. **Journal of Geophysical Research: Space Physics**, v. 83, n. A5, p. 2085–2090, 1978. 33

OYA, H.; TAKAHASHI, T.; WATANABE, S. Observation of low latitude ionosphere by the impedance probe on board the hinotori satellite. **Journal of Geomagnetism and Geoelectricity**, v. 38, n. 2, p. 111–123, 1986. 2, 23, 36, 53, 82, 84

PARK, J.; LUEHR, H.; MICHAELIS, I.; STOLLE, C.; RAUBERG, J.; BUCHERT, S.; GILL, R.; MERAYO, J. M.; BRAUER, P. Westward tilt of low-latitude plasma blobs as observed by the swarm constellation. **Journal of Geophysical Research: Space Physics**, v. 120, n. 4, p. 3187–3197, 2015. 25, 85

PARK, J.; LÜHR, H.; STOLLE, C.; ROTHER, M.; MIN, K.; MICHAELIS, I. Field-aligned current associated with low-latitude plasma blobs as observed by the champ satellite. In: **Annales Geophysicae**. [S.l.: s.n.], 2010. v. 28, n. 3, p. 697–703. 7, 25, 85, 92

PARK, J.; MIN, K. W.; LEE, J.-J.; KIL, H.; KIM, V. P.; KIM, H.-J.; LEE, E.; LEE, D. Y. Plasma blob events observed by kompsat-1 and dmsp f15 in the low latitude nighttime upper ionosphere. **Geophysical Research Letters**, v. 30, n. 21, 2003. 2, 69, 104

PARK, J.; STOLLE, C.; LÜHR, H.; ROTHER, M.; SU, S.-Y.; MIN, K. W.; LEE, J.-J. Magnetic signatures and conjugate features of low-latitude plasma blobs as observed by the champ satellite. **Journal of Geophysical Research: Space Physics**, v. 113, n. A9, 2008. 2, 7, 24, 25, 69

PAUL, A.; RAY, S.; DASGUPTA, A.; CHANDRA, H. Radio signatures of november 1998 leonid meteor on transionospheric vhf satellite signal. **Planetary and Space Science**, v. 49, n. 7, p. 755–759, 2001. 25

PAULA, E. R. et al. Ionospheric irregularity behavior during the september 6–10, 2017 magnetic storm over brazilian equatorial–low latitudes. **Earth, Planets and Space**, Springer, v. 71, n. 1, p. 42, 2019. 2, 20, 22

PAULINO, I.; PAULINO, A. R.; CUEVA, R. Y.; AGYEI-YEBOAH, E.; BURITI, R. A.; TAKAHASHI, H.; WRASSE, C. M.; SANTOS, Â. M.; MEDEIROS, A. Fragoso de; BATISTA, I. S. Semimonthly oscillation observed in the start times of equatorial plasma bubbles. In: **Annales Geophysicae**. [S.l.: s.n.], 2020. v. 38, n. 2, p. 437–443. 1, 2

PEDROSA, D. S.; TRIEBNIG, G. Visual analysis of swarm and geomagnetic model data. In: **Living Planet Symposium**. [S.l.: s.n.], 2016. v. 740, p. 275. 60, 101

PIMENTA, A.; FAGUNDES, P.; BITTENCOURT, J.; SAHAI, Y. Relevant aspects of equatorial plasma bubbles under different solar activity conditions. **Advances in Space Research**, v. 27, n. 6-7, p. 1213–1218, 2001. 1, 2, 3, 20, 68, 82

PIMENTA, A.; SAHAI, Y.; BITTENCOURT, J.; ABDU, M.; TAKAHASHI, H.; TAYLOR, M. J. Plasma blobs observed by ground-based optical and radio techniques in the brazilian tropical sector. **Geophysical Research Letters**, v. 31, n. 12, 2004. 1, 2, 23, 24, 36, 87, 99, 104

PIMENTA, A.; SAHAI, Y.; BITTENCOURT, J.; RICH, F. Ionospheric plasma blobs observed by oi 630 nm all-sky imaging in the brazilian tropical sector during the major geomagnetic storm of april 6–7, 2000. **Geophysical Research Letters**, v. 34, n. 2, 2007. 2, 36, 40, 46, 89

PIMENTA, A. A.; AMORIM, D. C.; ALMEIDA, A. A. de; MACHADO, C. S. Plasma blob observed by ground-based radio and optical techniques in the f-region: a case study on 27–28 august 1987. In: IEEE. **URSI General Assembly and Scientific Symposium**. [S.l.], 2011. p. 1–4. 108, 109, 110

RANA, G.; YADAV, M. The ionosphere and radio propagation. **Journal Impact Factor**, v. 5, n. 11, p. 09–16, 2014. 1, 8

RAWER, K. **The ionosphere: its significance for geophysics and radio communications.** [S.l.]: F. Ungar, 1956. 10, 12, 18

REZENDE, L. D.; PAULA, E. D.; KANTOR, I.; KINTNER, P. Mapping and survey of plasma bubbles over brazilian territory. **The Journal of Navigation**, v. 60, n. 1, p. 69, 2007. 26

RISHBETH, H.; GARRIOTT, O. K. Introduction to ionospheric physics. **New York: Academic Press**, 1969. 8, 12

ROHRBAUGH, R.; HANSON, W. B.; TINSLEY, B.; CRAGIN, B.; MCCLURE, J.; BROADFOOT, A. Images of transequatorial bubbles based on field-aligned airglow observations from haleakala in 1984-1986. **Journal of Geophysical Research: Space Physics**, v. 94, n. A6, p. 6763–6770, 1989. 52

SAHAI, Y.; AARONS, J.; MENDILLO, M.; BAUMGARDNER, J.; BITTENCOURT, J.; TAKAHASHI, H. Oi 630 nm imaging observations of equatorial plasma depletions at 16 s dip latitude. **Journal of Atmospheric and Terrestrial Physics**, v. 56, n. 11, p. 1461–1475, 1994. 1, 2, 45, 52, 53, 65, 68, 70

SAHAI, Y.; FAGUNDES, P.; BITTENCOURT, J. Transequatorial f-region ionospheric plasma bubbles: solar cycle effects. **Journal of Atmospheric and Solar-Terrestrial Physics**, v. 62, n. 15, p. 1377–1383, 2000. 1, 2, 3, 68, 82

SAHAI, Y.; FAGUNDES, P.; BITTENCOURT, J.; ABDU, M. Occurrence of large scale equatorial f-region plasma depletions during geo-magnetic disturbances. **Journal of Atmospheric and Solar-Terrestrial Physics**, v. 60, n. 16, p. 1593–1604, 1998. 72

SHARMA, A.; GURAV, O.; GAIKWAD, H.; CHAVAN, G.; NADE, D.; NIKTE, S.; GHODPAGE, R.; PATIL, P. Study of equatorial plasma bubbles using all sky imager and scintillation technique from kolhapur station: a case study. **Astrophysics and Space Science**, v. 363, n. 4, p. 1–11, 2018. 1, 2

SHI, J.; WANG, Z.; TORKAR, K.; ZHEREBTSOV, G.; RATOVSKY, K.; NOMANOVA, E. Study on plasma blob to result in radio signal scintillations in low latitude ionosphere. In: **Progress In Electromagnetics Research Symposium-Spring**. [S.l.: s.n.], 2017. p. 2004–2007. 2, 25, 36

SIBANDA, R. P. Challenges in topside ionospheric modelling over South Africa. **Rhodes University**, 2010. 9

SINHA, H.; RAJESH, P.; MISRA, R.; DUTT, N. Multi-wavelength imaging observations of plasma depletions over Kavalur, India. In: **Annales Geophysicae**. [S.l.: s.n.], 2001. v. 19, n. 9, p. 1119–1131. 83

SOONG, T. T. **Fundamentals of probability and statistics for engineers**. [S.l.]: John Wiley & Sons, 2004. 59, 60

TAKAHASHI, H.; WRASSE, C.; OTSUKA, Y.; IVO, A.; GOMES, V.; PAULINO, I.; MEDEIROS, A.; DENARDINI, C.; SANTANNA, N.; SHIOKAWA, K. Plasma bubble monitoring by tec map and 630 nm airglow image. **Journal of Atmospheric and Solar-Terrestrial Physics**, v. 130, p. 151–158, 2015. 1, 2, 9, 21, 22

TARDELLI-COELHO, F.; PIMENTA, A.; TARDELLI, A.; ABALDE, J.; VENKATESH, K. Plasma blobs associated with plasma bubbles observed in the brazilian sector. **Advances in Space Research**, v. 60, n. 8, p. 1716–1724, 2017. 2, 89

WANG, N.; LI, Z.; HUO, X.; LI, M.; YUAN, Y.; YUAN, C. Refinement of global ionospheric coefficients for gnss applications: methodology and results. **Advances in Space Research**, v. 63, n. 1, p. 343–358, 2019. 36

WANG, Z.; SHI, J.; TORKAR, K.; WANG, G.; WANG, X. A case study on ionospheric scintillations at low latitude associated with a plasma blob observed in situ. **Geophysical Research Letters**, v. 42, n. 7, p. 2109–2114, 2015. 2, 24, 25, 26

WATANABE, S.; OYA, H. Occurrence characteristics of low latitude ionosphere irregularities observed by impedance probe on board the hinotori satellite. **Journal of Geomagnetism and Geoelectricity**, v. 38, n. 2, p. 125–149, 1986. 2, 23, 53, 69, 104

WEBER, E.; BUCHAU, J.; MOORE, J. Airborne studies of equatorial f layer ionospheric irregularities. **Journal of Geophysical Research: Space Physics**, v. 85, n. A9, p. 4631–4641, 1980. 1, 2

WRASSE, C. Estudos de geração e propagação de ondas de gravidade atmosféricas. **São José dos Campos: INPE**, 2004. 42, 43, 57

YOKOYAMA, T.; SU, S.-Y.; FUKAO, S. Plasma blobs and irregularities concurrently observed by rocsat-1 and equatorial atmosphere radar. **Journal of Geophysical Research: Space Physics**, v. 112, n. A5, 2007. 2

ZOLESI, B.; CANDER, L. R. **Ionospheric prediction and forecasting**. [S.l.]: Springer, 2014. 8

formato bibtex (p.ex: referencia.bib)